Quasi Two-Dimensional ^{6}Li Fermi gas

A thesis submitted for the degree of

Doctor of Philosophy

by

Paul Dyke

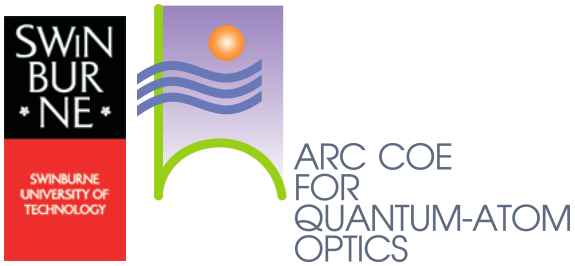

Centre for Atom Optics and Ultrafast Spectroscopy and

ARC Centre of Excellence for Quantum-Atom Optics

Faculty of Engineering and Industrial Sciences

Swinburne University of Technology

Melbourne, Australia

June 3, 2010

Declaration

I, Paul Dyke, declare that this thesis entitled:

"Quasi Two Dimensional ^{6}Li Fermi gas"

is my own work and has not been submitted previously, in whole or in part, in respect of any other academic award.

Paul Dyke

Centre for Atom Optics and Ultrafast Spectroscopy
Faculty of Engineering and Industrial Sciences
Swinburne University of Technology
Melbourne, Australia

Dated this day, June 3, 2010

- To my family

Abstract

Quasi-2D degenerate Fermi gases provide a rich physical environment to explore since many effects that are present do not exist in 3D. This thesis describes the first experiments carried out in a quasi-2D Fermi gas across the broad ^{6}Li Feshbach resonance at 834 G. A description of the apparatus used to form molecular Bose-Einstein condensates and degenerate Fermi gases in the two lowest hyperfine states of ^{6}Li, $|F = 1/2, m_f = 1/2\rangle$ and $|F = 1/2, m_f = -1/2\rangle$, is presented. An anisotropic 2D optical potential is formed by an elliptical Gaussian beam produced by tightly focusing a circular Gaussian beam in one direction with a cylindrical lens. The trapping frequencies are $\sim$3 kHz in the axial direction and $\sim$50 Hz in the radial direction giving an aspect ratio of $\sim$60. For a non-interacting Fermi gas this allows $\sim$1700 atoms to populate the lowest transverse harmonic oscillator state and to be considered as quasi-2D.

We present the transition from a three dimensional gas to a two dimensional gas at $\sim$2000 atoms agreeing within experimental uncertainty with the non-interacting atom number. The observations are made through measuring the radial and axial widths of the gas at three different magnetic fields, 810 G, 834 G, and 991 G. The widths σ are then plotted against the atom number N. The curve, $\log \sigma(N) = n \log N + a$, is then fit to the data in the 3D regime and in the 2D regime. The expansion of a non-interacting Fermi gas in the 2D regime changes from a scaling of $N^{1/4}$ to $N^{1/6}$ in the 3D regime and for a Bose gas it changes to $N^{1/5}$. A value for n is extracted in each of these regimes. For each magnetic field we then obtain in the 2D regime: $n = 0.27(0.04)$ at

810 G, $n = 0.23(0.02)$ at 834 G and $n = 0.26(0.01)$ at 991 G. In the 3D regime we obtain: $n = 0.195(0.01)$ at 810 G, $n = 0.154(0.01)$ at 834 G and $n = 0.175(0.01$ at 991 G. We also observe a change in the aspect ratio as we approach the 2D regime which is not present in our 3D single beam optical dipole trap and is absent in any 3D system. These first results indicate that we have a quasi-2D Fermi gas.

The main experimental results are the first indications of a confinement induced resonance in a ^{6}Li Fermi gas through the measurement of the cloud width in the tightly confined direction after a fixed expansion time. We observe a significant deviation in the transverse width of the 2D interacting Fermi gas from the 3D case due to the increased tight confinement. The confinement induced resonance should appear when the 3D scattering length approaches the transverse harmonic oscillator length, $a_z = \sqrt{\hbar/m\omega_z}$, where m is the mass and ω_z is the tight transverse trapping frequency. For our experimental parameters this leads to a 3D scattering length of 1.03 μm, where the observation is at 819(1) G. In the weakly confined direction there is no such increase in the width due to the free motion in the xy plane. Instead the cloud width across the Feshbach resonance increases monotonically, similar to that of a 3D gas and as described theoretically for a quasi-2D Fermi gas by Lin *et al.* [1].

Acknowledgements

I would not have been able to present the work in this thesis if it were not for many of the people in and around our laboratory. I start by thanking my supervisors Wayne Rowlands and Peter Hannaford for giving me an opportunity to work in such a fantastic field of research and for the support they have given.

In January 07 Chris Vale arrived in our laboratory and it was not long after that we obtained our first molecular Bose-Einstein condensate and in 2008 took over the CI role from which we have benefited greatly. It has been a pleasure to work with Chris. He has been a wealth of knowledge and support since he arrived at Swinburne University. His ability to happily explain the same thing to me many times until I actually understand it is very much appreciated. He has also spent many hours along with Peter, reading and improving the drafts of this thesis of which I am very thankful.

When I joined the lithium lab I was fortunate to join a great group of people, Grainne Duffy, Jürgen Fuchs, Gopi Veeravalli and Heath Kitson who was working on the photo-association of atomic rubidium next to our experiment. During the first couple of years most of my time was spent working with Jürgen who taught me about the laser system and how to run our experiment.

It has also been a pleasure to work with Eva Kuhnle who joined our group in June 07. She quickly proved to be a remarkable researcher and is an asset to our laboratory. I was also fortunate to spend time working with Michael Mark; not only did he prove to be a great researcher, his constant supply of coffee was most welcome.

To make an experiment such as ours you need a great technician and I am indebted to Mark "the Magnificent" Kivinen for construction of the equipment that we use.

Thanks must also go to Tatiana Tchernova for her administrative support.

During my time at CAOUS I have enjoyed the company of many people that have provided me with useful advice on physics, lending of equipment, writing of Labview code, dinner partners and many other things. So to Chris Ticknor, Brenton Hall, Andrei Sidorov, Jeff Davis, Alexander Akoulchine, Shannon Whitlock, Mandip Singh, Russell Anderson, Chris Hall, David McDonald, Dan White and anyone that I may have missed, thank you.

As a student you are always looking for ways to make a little extra money and so I thank Tom Edwards, Alex Mazzolini, Don Ward-Smith and Russel McLean for giving me the opportunity to teach.

Finally and most importantly I thank my family. Without their constant support and understanding none of this would be at all possible.

Contents

List of Figures

Chapter 1

Introduction

Since the advent of laser cooling and trapping techniques [2, 3, 4, 5] and the creation of gaseous Bose-Einstein condensates (BEC) [6, 7, 8], the rate of theoretical and experimental progress with these systems has been dramatic. Initial investigations involved the trapping of bosonic atoms of alkali elements such as ^{87}Rb and ^{23}Na. Bosons have the unique feature of being able to occupy the same quantum state. When cooled below a critical temperature a macroscopic occupation of the ground state can occur. For the other class of quantum particles, fermions, it was not so obvious that condensation could occur. However, the cooling apparatus employed in forming bosonic BECs were also being employed with fermions. Fermions are the building blocks of matter, and exist in superconductors [9], superfluids [10], neutron stars, and many other ensembles. Experimental and theoretical investigation into Fermi gases trailed bosonic gases. Fermions are subject to the Pauli exclusion principle, which states that two or more fermions cannot occupy the same state. This leads to a restriction on collisions that are essential in rethermalisation of the gas during evaporative cooling. Therefore non-interacting Fermi gases would have no condensation effects similar to its bosonic counterpart, and may appear to be simple systems. However, if two fermions of opposite spins are available which can interact, it is possible to form Cooper pairs [11] allowing condensation to a Fermi superfluid at sufficiently low temperatures [12]. In a weakly

interacting Fermi gas the temperature to achieve superfluidity has been postulated to be so low that it is technically extremely difficult to achieve. However, it is possible to form strongly interacting Fermi gases [13, 14, 15, 16, 17, 18, 19] through the use of an extraordinary tool called a Feshbach resonance [20, 21, 22, 23]. A superfluid that is in the strongly interacting region where the scattering length is large compared to the inter-particle separation will have a much higher transition temperature [12]. This makes it more accessible to experiments.

A magnetic Feshbach resonance allows us to control the two-body interactions between fermions of opposing spin configurations. This allows access to attractive and repulsive interactions through a simple change in the magnetic field. Below the Feshbach resonance the interactions are repulsive. Cooling of an atomic sample below the characteristic temperature T^*, two fermions with opposite spins can form a composite boson through three body recombination [24]. The resulting system then follows Bose-Einstein statistics. Cooling further below T_C the system condenses and forms a molecular Bose-Einstein condensate (mBEC) [25, 26, 27, 28, 29, 30, 31, 32, 33]. At the Feshbach resonance a strongly interacting region occurs where the scattering length diverges to $\pm\infty$ and the gas is said to be unitary. Here Fermi gases are universal [34, 35, 36, 37, 38] since they no longer depend upon the scattering length and the results can be applied to any other Fermi system. Above the Feshbach resonance the interactions become attractive and an interacting fermionic gas is formed. Bose-Einstein condensation does not occur due to the Pauli principle. However, weakly bound Cooper pairs [11] are formed between fermions of opposite spins and at sufficiently low temperatures a superfluid can form. This is described by the Bardeen, Cooper, and Schrieffer (BCS) [39] theory of superconductivity.

1.1 Motivation

The systems outlined previously have been compared to solid state condensed matter systems. With the advent of strongly interacting Fermi gases that analogy becomes even stronger. Along with the control that can be applied to interacting Fermi gas systems other regimes can be accessed. One is lower dimensional quantum degenerate gases. The behaviour of particles trapped in lower dimensional systems dramatically changes, often in a counterintuitive way. The BEC transition can be drastically altered by the reduction of dimensionality. In a two dimensional, uniform ideal Bose gas there is no BEC transition at finite temperature. This is a striking example of how thermal and quantum phase fluctuations can destroy the long range order at finite temperature in a Bose and Fermi gas. This has been shown in [40, 41, 42], and is known as the Mermin-Wagner Hohenberg Goldstone theorem. Considering only the 2D uniform ideal Bose gas the usual BEC phase transition is not possible; however the possibility of a transition of a different character was pointed out by Kane and Kadanoff [43] and proven by Berezinskii [44]. Independently, Kosterlitz and Thouless showed that this transition was composed of spontaneously formed vortex-antivortex pairs in the context of the solid state XY planar model [45]. Evidence for this transition, known as the BKT or KT transition, has been seen in 2D ^{4}He films [46]. It is believed that above the BKT transition temperature a quasi-condensate phase exists. In this region the condensate has no global phase coherence, but only local phase coherence. This has been experimentally observed in atomic hydrogen [47]. Below the BKT transition vortices pair up and the system acquires long range coherence.

Applying a magnetic or optical trapping potential to a quantum degenerate gas modifies the density of states and can suppress phase fluctuations across it. It was shown [48] that the modification to the density of states will allow the formation of a BEC at finite temperature in two dimensions but it is unclear whether an interacting gas undergoes a BEC like transition or a BKT type transition. In recent years, two dimensional quantum gases have generated much activity in trying to observe the BKT

transition using cold atoms.

The first low dimensional Bose condensate was reported in 2001 by Görlitz *et al.* [49]. They observed the crossover from 3D to a 2D and 1D condensate in an optical dipole potential with an aspect ratio of $\lambda \approx 80$. To reach lower dimensions they reduced the atom number such that it was below a critical atom number set by the aspect ratio of the optical trap. Since then a number of groups have studied the quasi-2D regime [50, 51, 52, 53, 54] in various trapping configurations. In 2006 Hadzibabic *et al.* [55] reported evidence of the BKT transition in a trapped atomic gas. The observations were through phase dislocations in the matter-wave interference patterns of overlapping 2D Bose gases released from a blue detuned optical lattice. The dislocations were attributed to vortices in the Bose gas associated with the BKT topological phase transition. More recently Cladè *et al.* [53] have observed the transition from a thermal Bose gas to a 2D quasi-condensate and perhaps the superfluid regime below the BKT transition. Another example is the transition to a Tonks gas [56, 57] formed in a one dimensional system where the strong interactions cause the Bose gas to behave like a system of ideal fermions. The reduction of dimensions also has a huge impact upon the scattering properties of the gas in the presence of a Feshbach resonance. It has been shown for a one dimensional Fermi gas that a weakly interacting bound state can exist independent of the scattering sign [58]. Measurements of p-wave Feshbach resonances [59] in 1D and 2D lattices were observed in ^{40}K, where there is a shift in the resonance position caused by the confining potential. More recently there have been measurements in a 1D Bose gas of ^{133}Cs [60] where a confinement induced resonance was observed and a transition to a Super Tonks-Girardeau region was demonstrated. Quasi-2D Fermi gases have not received much attention since they are notoriously difficult to treat both experimentally and theoretically. One recent publication [61] discussed the inelastic collisions in a quasi-2D Fermi gas formed in a red-detuned lattice. Prior to that Ferlaino *et al.* [62] produced a quasi-2D Bose-Fermi mixture in a 1D optical lattice.

In this thesis we present experiments that explore the quasi-2D region in a strongly

interacting ^{6}Li Fermi gas. The first objective is to observe a crossover from a 3D system to a 2D system at different magnetic fields in the BEC-BCS crossover. This represents the first experimental study of a quasi-2D Fermi gas at the Feshbach resonance. The second and main objective is to characterise the width of a quasi-2D Fermi gas as we pass through the Feshbach resonance through observations of deviations from the three dimensional behaviour of the gas. This represents the first attempt at such an experiment.

1.2 Thesis outline

The outline of this thesis is as follows: Chapter 2 briefly describes the theory required to understand Feshbach resonances and collisions at ultracold temperatures. The properties of a harmonically trapped non-interacting and interacting three dimensional quantum degenerate gas are then discussed. Following on from this the theory of two dimensional quantum gases is presented. The main idea is to look at some of the novel properties associated with 2D quantum degenerate gases and to describe the scattering properties required to understand the experiments in our laboratory. For completeness a brief review of the experimental work carried out on the BKT transition is provided, even though it is not the main focus of this thesis. Chapter 3 presents the main experimental set-up, that describes the vacuum system, lasers, and absorption imaging techniques. This chapter also describes the construction of the 2D optical trap and the details of producing quantum degenerate gases. Chapter 4 discusses the characterisation and production of molecular BECs and degenerate Fermi gases and characterises the trapping frequencies of the 2D optical trap. Chapter 5 presents the results of the quasi-2D Fermi gas experiments. We observe a crossover from a 3D gas to a 2D gas from measurements of the width of the cloud in both the axial and radial directions at three different magnetic fields. We also observe the aspect ratio changing as a function of the atom number which is a unique property of a lower dimensional quantum degenerate gas. The first observations of a confinement induced resonance

in a quasi-2D Fermi gas are then described. Measurements of cloud size after time of flight expansion across the BEC-BCS crossover are made in order to observe this phenomenon and it is shown to depend upon the geometry of the system. Chapter 6 gives an overall summary of the thesis and looks to future experiments that can be performed.

Chapter 2

Quantum degenerate gases in 2D and 3D

2.1 Introduction

At the centre of research on ultracold Fermi gases is the Bose-Einstein condensate to Bardeen, Cooper, Schrieffer crossover (BEC-BCS crossover). Here we have the ability to tune the interactions between the particles such that their behaviour changes from being dominated by bosonic to fermionic degrees of freedom. These two seemingly different physical regimes are connected through a Feshbach resonance described in section 2.3. The Feshbach resonance connects three very different regimes. At the Feshbach resonance the s-wave scattering length between two fermions in different spins states diverges to infinity. At this point the gas is said to be unitary and has universal properties. Below the resonance a new bound molecular state leads to a positive scattering length and two fermions can form a composite boson and will follow Bose-Einstein statistics [29, 25, 32] which can undergo molecular Bose-Einstein condensation (mBEC). Above the Feshbach resonance the scattering length is negative (attractive), and the formation of molecules is prohibited; however, pairing can still

occur. For a weakly interacting Fermi gas at sufficiently low enough temperatures correlated pairs, known as Cooper pairs, can form [11]. These are analogous to the pairs of electrons found in the Bardeen, Cooper, and Schrieffer (BCS) [39] theory of superconductivity. In between these regimes it is possible to form a resonantly interacting superfluid.

High temperature superconductivity has been investigated in condensed matter systems through lower dimensional physics. Confinement of a quantum degenerate gas to lower dimensions leads to a richness of physics not found in 3D. It has been shown by [40, 41, 42] that long range order associated with 3D condensates and Fermi fluids was destroyed due to phase fluctuations across the atomic sample in lower dimensional systems. However, it was pointed out by Kane and Kadanoff [43] that there may be another form of transition taking place other than the usual BEC phase. This was proven by Berezinskii [44] and shown by Kosterlitz and Thouless (BKT) [45] that there was a topological phase transition associated with the spontaneous formation of vortex-antivortex pairs. Above the BKT transition the condensate is believed to be composed of individual condensates where each small condensate has a uniform phase but is uncorrelated with its neighbouring condensate. This region is known as a quasi-condensate.

In this chapter we introduce the concepts of the BEC-BCS crossover and the physics associated with fermions and bosons that is required to understand our experiments in 2D and 3D. This chapter is not a comprehensive account of quantum degenerate gases and their interactions. For more detailed information the reader is referred to many comprehensive texts such as [63, 64, 65, 66, 67, 68] and articles [69, 70].

2.2 Interactions in an ultracold gas

There are many quantum mechanics texts that deal with the scattering of two particles [71, 72, 73, 74], and review articles [75, 64, 76] that discuss the role of

collisions in ultracold gases. Here we review some of the main concepts. Two types of collisions can take place in an ultracold gas, inelastic and elastic. An inelastic collision transfers energy between the internal and external degrees of freedom. Generally a change in internal energy leads to an increase in the external (kinetic) energy; so an inelastic collision will result in atom loss if the trapping depth is smaller than the energy released. Otherwise it is possible for the atom to stay trapped and heat the atomic sample. An example of an inelastic process is three body recombination where three atoms collide, two form a molecule and the internal (binding) energy released is shared between the other atom and the molecule. Elastic collisions are instrumental in establishing thermalisation of the atomic sample and conserve the momentum and kinetic energy of the colliding atomic pair. Here we deal with elastic collisions between two particles. When the interatomic potential is a function of only the separation between the particles, the relative and centre of mass variables in the scattering problem are separable. Relative motion can be reduced to the scattering of a single particle with reduced mass $\mu = m_1 m_2/(m_1 + m_2)$ from a potential $V(r)$. The time independent Schrödinger equation for the relative motion is

$$\Big(\frac{\hbar^2}{2\mu}\nabla^2 + V(\mathbf{r})\Big)\Psi(\mathbf{r}) = E\Psi(\mathbf{r}), \tag{2.2.1}$$

where $V(\mathbf{r})$ is the spherical scattering potential. We can determine a scattering solution $\psi(\mathbf{r})$ to equation 2.2.1 composed of an incident plane wave $e^{i\mathbf{k}\cdot\mathbf{z}}$ and a scattered spherical wave $f(k,\theta)\frac{e^{ikr}}{r}$, where the function $f(k,\theta)$ is the scattering amplitude and is dependent on the initial momentum $\hbar\mathbf{k}$ and θ is the angle between the incident and scattered direction of the particle. Outside of the interaction region (where $V(r) \to 0$) we have

$$\Psi_{\mathbf{k}}(\mathbf{r}) = e^{i\mathbf{k}\cdot\mathbf{z}} + f(k,\theta)\frac{e^{ikr}}{r}. \tag{2.2.2}$$

In most cases we are interested in the scattering cross section of the particle. This can be derived through the differential cross section $d\sigma/d\Omega$ by considering the probability that the scattered wave will cross some infinitesimal area per unit time $\mathbf{d}A = r^2\mathbf{d}\Omega$

given by

$$\frac{v}{r^2}|f|^2\mathbf{d}A = v|f|^2\mathbf{d}\Omega, \tag{2.2.3}$$

where v is the current density (flux per unit area) of the incident wave, allowing us to write the cross section as

$$\frac{\mathrm{d}\sigma}{\mathrm{d}\Omega} = |f(k,\theta)|^2. \tag{2.2.4}$$

Any function of θ can be expanded in terms of Legendre polynomials which produces a solution of equation 2.2.4 as

$$f(k,\theta) = \sum_{l=0}^{\infty}(2l+1)f_l(k)P_l(\cos\theta) \tag{2.2.5}$$

where $f_l(k)$ are the coefficients of the expansion known as the partial wave scattering amplitudes and can be written in terms of the partial wave phase shifts δ_l as

$$f_l(k) = \frac{\exp(i\delta_l)\sin\delta_l}{k}. \tag{2.2.6}$$

Using equations 2.2.4, 2.2.5 and 2.2.6 gives the total scattering cross section as

$$\sigma(k) = \sum_{l=0}^{\infty}\frac{4\pi}{k^2}\sin^2\delta_l(k). \tag{2.2.7}$$

For small values of k the phase shifts vary as $\delta_l(k) \propto k^{2l+1}$. In this low energy limit partial waves with $l \neq 0$ fall off as $\sigma \propto k^{4l}$. Thus the $l = 0$ wave is the dominant contribution to the total cross section, and derives from s-wave isotropic scattering. Using equation 2.2.7 for $l = 0$, one determines the total cross section to be

$$\sigma = \frac{4\pi a^2}{1+k^2a^2} \tag{2.2.8}$$

where a is the s-wave scattering length.

There are two limiting cases, the strongly interacting limit ($ka \gg 1$) and the weakly interacting limit ($ka \ll 1$). In the weakly interacting limit the scattering cross section

reduces to the general case of $4\pi a^2$. This is a consequence of the de Broglie wave length of the scattering atoms being larger than the s-wave energy. However in the strongly interacting limit the opposite is true and when $a \to \pm\infty$ the scattering cross section becomes $\sigma(k) = 4\pi/k^2$. This is the unitary limit and the scattering becomes independent of the scattering length.

2.3 Feshbach resonance

Access to the weak and strongly interacting regimes is accomplished through the use of a Feshbach resonance, first discovered by H. Feshbach in the context of nuclear scattering [20]. In this section we outline the basic idea of a Feshbach resonance. A more detailed theoretical discussion can be found in [77, 78] and references therein. In figure 2.3.1 we show how a Feshbach resonance arises between two colliding atoms. In this picture two scattering potential curves, or channels, are shown for atoms in

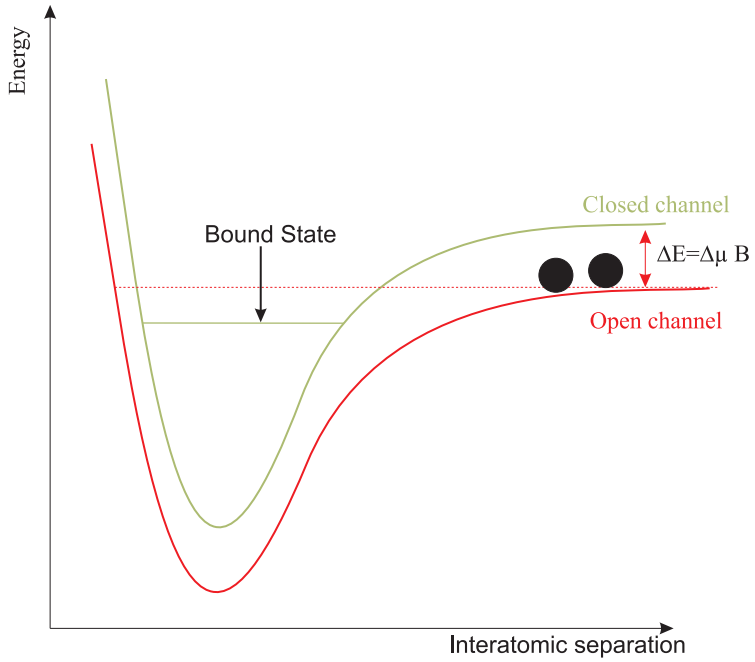

Figure 2.3.1: The scattering process near a Feshbach resonance. The open and closed channels have different magnetic moments. Tuning an external magnetic field the closed channel can be shifted to coincide with the open channel leading to a resonance.

different spin configurations. For the experiments performed in our laboratory the resonance occurs between ^{6}Li atoms in the internal states $|F = 1/2, m_f = 1/2\rangle$ ($|1\rangle$) and $|F = 1/2, m_f = -1/2\rangle$ ($|2\rangle$). The two incoming atoms normally interact in the lower energy "open channel", and the closed channel would have no effect on the scattering process since this is energetically inaccessible at large inter-atomic distances $R_e = \infty$. However, in these systems it is possible to tune the total energy of the open channel such that it coincides with the bound state energy in the closed channel giving rise to a Feshbach resonance. In general the two channels will have different magnetic moments, since one may be a triplet state and the other a singlet state, which allows them to be tuned relative to each other. Near the Feshbach resonance the scattering length varies with the strength of an applied magnetic field, according to [79]

$$a = a_{bg}\left(1 + \frac{\Delta B}{B - B_0}\right) \tag{2.3.1}$$

where a_{bg} is the background scattering length in the open channel, B is the strength of the applied external magnetic field, B_0 is the resonant magnetic field and ΔB is the width of the resonance. In figure 2.3.2 we plot the broad Feshbach resonance of ^{6}Li for the two lowest hyperfine states.

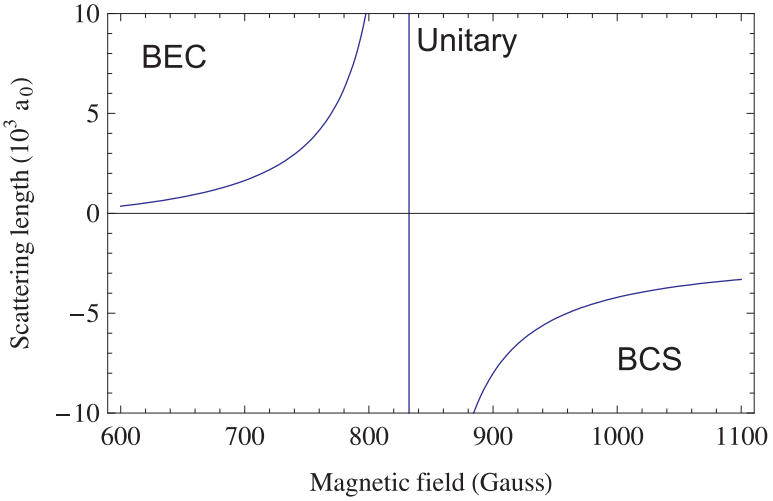

Figure 2.3.2: Calculated behaviour of the scattering length a for ^{6}Li atoms in states $|1\rangle$ and $|2\rangle$ across the BEC-BCS crossover [80].

2.4 Quantum statistics

The quantum statistics of a gas becomes important when the temperature is reduced such that the thermal de Broglie wavelength $\lambda_{dB} = \sqrt{\frac{2\pi\hbar^2}{mk_{\mathrm{B}}T}}$ is comparable to the inter-particle spacing, where m is the mass of the particle at temperature T. We can define a critical phase space density as $D = n\lambda_{dB}^3$ where n is the particle density. In the limit $n\lambda_{\mathrm{dB}}^3 \ll 1$ a gas of indistinguishable particles can be described by Maxwell-Boltzmann statistics since the mean occupation of all states is less than one. Cooling the gas such that $n\lambda_{\mathrm{dB}}^3 \geq 1$ brings the quantum mechanics of the system into play. We now need to describe the particles using either Bose-Einstein statistics for particles with an integer value of their intrinsic angular momentum (spin) or Fermi-Dirac statistics for those with an odd half integer spin. The average occupation of a single particle state for the different types of particles are

$$n(\varepsilon) = \frac{1}{\exp[(\varepsilon - \mu)/k_B T] - 1} \qquad \text{Bosons} \tag{2.4.1}$$

$$n(\varepsilon) = \frac{1}{\exp[(\varepsilon - \mu)/k_B T] + 1} \qquad \text{Fermions} \tag{2.4.2}$$

where T is the temperature, k_B is the Boltzmann constant, ε is the particle energy in that state. The chemical potential μ is given by the normalisation condition

$$\sum_i n(\varepsilon) = N \tag{2.4.3}$$

where N is the total number of atoms. For a gas of identical bosons a macroscopic occupation of the ground state can ensue as the temperature for a constant atom number N drops below the critical temperature. This occurs since μ changes to conserve N. As μ approaches ε from below the denominator in equation 2.4.1 approaches zero and occupation of the ground state becomes large and Bose-Einstein condensation takes place. Fermions, however, can only fill up the available states with one particle per state. This is described by the Pauli exclusion principle which is a consequence of the

fact that the total wave-function for two identical fermions must be anti-symmetric and therefore forbids the simultaneous quantum occupation of a state. At $T = 0$ all bosons will be condensed in the ground state and fermions will occupy the lowest available state up to the Fermi energy E_F as depicted in figure 2.4.1.

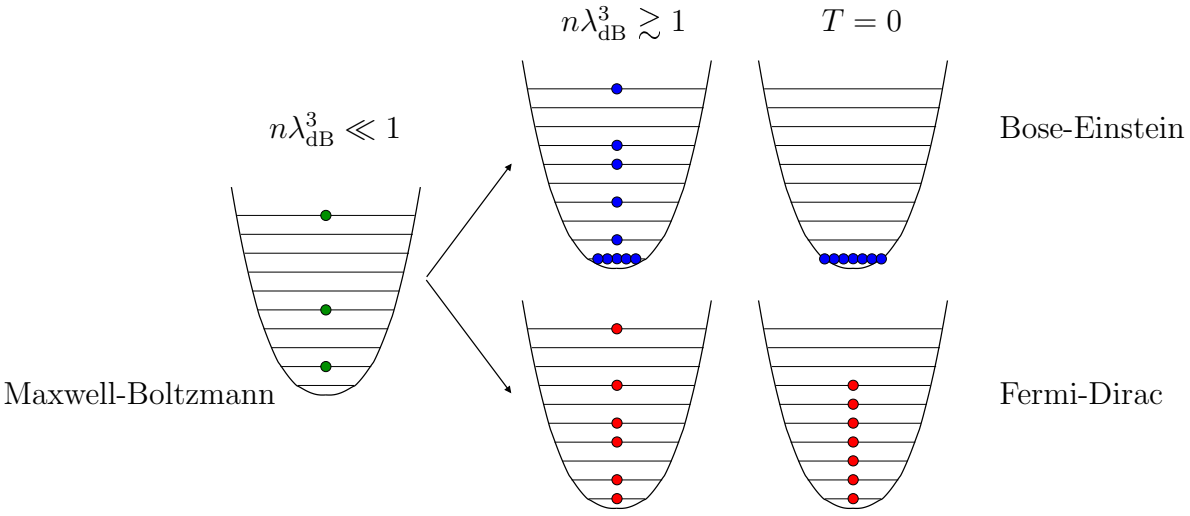

Figure 2.4.1: Comparing the quantum statistical behaviour of the atomic sample at various temperatures as described in the text [81, 82].

2.5 The harmonically trapped non-interacting gas

Experiments with atomic gases are in general confined to a harmonic potential defined as

$$V(r) = \frac{1}{2} m \sum_i (\omega_i^2 i^2) \tag{2.5.1}$$

where m is the atomic mass and ω_i is the trapping frequency with $i = x, y, z$. A semiclassical description of the thermodynamical properties can be applied if the temperature of the sample greatly exceeds the harmonic oscillator level spacings for individual particle states ($k_B T \gg \hbar\omega_i$). The confining potential determines the density of states. We can write down the semiclassical formula and find the density of states

for a confining potential using [83]

$$g(\varepsilon) = \int \frac{d^D\mathbf{r}d^D\mathbf{p}}{(2\pi\hbar)^D}\delta(\varepsilon - \varepsilon(\mathbf{r},\mathbf{p})) \tag{2.5.2}$$

where $\delta(x)$ is the Dirac delta function and $D = 1, 2, 3$. Integrating this for a harmonic potential leads to

$$g(\varepsilon) = \frac{\varepsilon^{d-1}}{(d-1)!\prod_{i=1}^{d}\hbar\omega_i}. \tag{2.5.3}$$

For the three dimensional harmonic oscillator we have

$$g(\varepsilon) = \frac{\varepsilon^2}{(2)\hbar^3\bar{\omega}^3} \tag{2.5.4}$$

where $\bar{\omega}$ is the geometric mean of the trapping frequencies $(\omega_x\omega_y\omega_z)^{1/3}$.

2.5.1 Bose gas

In the case of bosons occupation of the single particle state with energy ε is given by equation 2.4.1. Multiplying this by the density of states $g(\varepsilon)$, and summing overall states defines the total number of atoms

$$N = \sum n(\varepsilon)g(\varepsilon). \tag{2.5.5}$$

In the semiclassical formulation we can replace the summation over all particle states by an integral

$$N = N_0 + \int n(\varepsilon)g(\varepsilon)d\varepsilon, \tag{2.5.6}$$

where N_0 is the number of atoms occupying the ground state. N_0 must be treated separately as in the semiclassical description, $g(0) \to 0$ and condensation will not show up. Evaluating the integral with the chemical potential $\mu = 0$ gives the critical

temperature T_c as [63]

$$T_c = \Big(\frac{N}{\zeta(3)}\Big)^{1/3} \frac{\hbar\bar{\omega}}{k_B} \approx 0.94 \frac{\hbar\bar{\omega}}{k_B} N^{1/3} \tag{2.5.7}$$

where $\zeta(3)$ is a the Riemann Zeta function. It then follows that we can determine the condensate fraction as a function of temperature by combining equation 2.5.7 with equation 2.5.5

$$N_0/N = 1 - \Big(\frac{T}{T_C}\Big)^3. \tag{2.5.8}$$

In a non-interacting ideal gas condensate all particles will occupy the lowest single particle state and the shape of the ground state wave function $\varphi_0(r)$ gives the density distribution $n(r)$, where the harmonic oscillator ground state wave function in three dimensions is

$$\varphi_0(r) = \Big(\frac{m\bar{\omega}}{\pi\hbar}\Big) \exp\Big[- \frac{m}{2\hbar}(\omega_x x^2 + \omega_y y^2 + \omega_z z^2)\Big]. \tag{2.5.9}$$

As the particle number N grows so does the density $n(r) = N|\varphi(r)|^2$. However, the condensate size remains independent of N. Instead it is fixed by the harmonic oscillator length given as

$$a_{ho} = \sqrt{\frac{\hbar}{m\bar{\omega}}}. \tag{2.5.10}$$

For temperatures well above the condensation temperature classical gas statistics are obeyed where the widths of the distributions are [63]

$$R_i^2 = \frac{2k_B T}{m\omega_i^2}. \tag{2.5.11}$$

The widths are much broader than a_{ho} and Bose-Einstein condensation shows up as a visible narrow peak in the spatial and momentum distributions as the temperature is lowered.

2.5.2 Fermi gas

The trapped non-interacting Fermi gas is dealt with similarly to the Bose case, but using Fermi-Dirac statistics. Considering N identical fermions we are interested in the energy of the highest occupied state known as the Fermi energy E_F. This is given by the chemical potential at $T = 0$. Substituting equations 2.4.2, where $n(\varepsilon)$ becomes a unit step function as $T \to 0$, and 2.5.4 into 2.5.5 and integrating up to E_F gives

$$E_{\mathrm{F}} = \hbar\overline{\omega}(6N)^{1/3} = k_{\mathrm{B}}T_{\mathrm{F}}, \tag{2.5.12}$$

where T_F is the Fermi temperature. The density distribution at $T = 0$ can be calculated by using the semiclassical local density approximation (LDA). This assumes that the sample can be approximated by a uniform gas at any local position. Defining a local Fermi wave vector k_F at each point in space gives

$$E_F(\mathbf{r}) = \frac{\hbar^2 k_F(\mathbf{r})^2}{2m}. \tag{2.5.13}$$

At some position r all states are filled up to $\hbar k_F(\mathbf{r})$. The number of atoms that can fill the momentum sphere with radius $\hbar k_F(\mathbf{r})$ is given as

$$n(\mathbf{r}) = \frac{4}{3}\pi(\hbar k_F(\mathbf{r}))^3 \frac{1}{(2\pi\hbar)^3}. \tag{2.5.14}$$

Combining equations 2.5.13 and 2.5.14 we obtain the density distribution of the non-interacting Fermi gas

$$n(\mathbf{r}, T = 0) = \frac{1}{6\pi^2}\Big[\frac{2m}{\hbar^2}(E_f - V(\mathbf{r}))\Big]^{3/2}. \tag{2.5.15}$$

The point at which $V(\mathbf{r}) > E_F$ sets the maximum extent of the cloud, which is called the Fermi radius. Setting $V(R^i) = E_F$ we have

$$R^i_{\mathrm{F}} = \sqrt{\frac{2k_{\mathrm{B}}T_{\mathrm{F}}}{m\omega_i^2}} \qquad \text{or} \qquad R^i_{\mathrm{F}} = \sqrt{\frac{\hbar}{m\overline{\omega}}}\big(48N\big)^{1/6}\frac{\overline{\omega}}{\omega_i}. \tag{2.5.16}$$

Equation 2.5.15 for the zero temperature density distribution becomes

$$n(\mathbf{r}, T=0) = \frac{8N}{\pi^2 R_{\mathrm{F}}^x R_{\mathrm{F}}^y R_{\mathrm{F}}^z}\Big[1 - \Big(\frac{x}{R_{\mathrm{F}}^x}\Big)^2 - \Big(\frac{y}{R_{\mathrm{F}}^y}\Big)^2 - \Big(\frac{z}{R_{\mathrm{F}}^z}\Big)^2\Big]^{3/2}. \tag{2.5.17}$$

2.6 Interacting Bosons

Interparticle interactions through Van der Waals forces play an important role in the dynamics of real BECs. The many body Hamiltonian in second quantised form is given by [84]

$$\begin{aligned} \hat{H} &= \int \hat{\Psi}^\dagger\Big(-\frac{\hbar^2}{2m}\nabla^2 + V_{ext}\Big)\hat{\Psi}(\mathbf{r})d\mathbf{r} \\ &+\frac{1}{2}\int \hat{\Psi}^\dagger(\mathbf{r})\hat{\Psi}^\dagger(\mathbf{r})V_{int}(\mathbf{r}-\mathbf{r}')\hat{\Psi}(\mathbf{r})\hat{\Psi}(\mathbf{r})d\mathbf{r}d\mathbf{r}' \end{aligned} \tag{2.6.1}$$

where V_{ext} is the trapping potential, $\hat{\Psi}(\mathbf{r})$ is the bosonic field operator and $V_{int}(\mathbf{r}-\mathbf{r}')$ is the interaction potential. It is possible to solve the full quantum mechanical model of an interacting system, as done in [85], for 10^4 atoms using Monte Carlo methods. This can provide exact results; however it requires great computational power and is generally impractical for realistic experimental systems. As such approximate methods are employed. The simplest method is a mean field approximation, first formulated by Bogoliubov [86]. The main point is to separate out the condensate part of the field operator $\hat{\Psi}(\mathbf{r}, t)$ and describe it by a classical field $\psi(\mathbf{r})$ with fluctuations δ. We can make the approximation that the condensate wavefunction is the expectation value of the field operator $\psi(\mathbf{r}) = \langle\hat{\Psi}(\mathbf{r})\rangle$. This allows us to neglect the quantised nature of the field operator. Derivation of the condensate wave function consists of rewriting the field operator using the Heisenberg equation with equation 2.6.1 and replacing the field

operator $\hat{\Psi}(\mathbf{r},t)$ with the classical field $\psi(\mathbf{r})$ [84].

$$i\hbar\frac{\partial}{\partial t}\hat{\Psi} = [\hat{\Psi},\hat{H}] = \Big(-\frac{\hbar^2}{2m}\nabla^2 + V_{ext}(\mathbf{r}) + \int d\mathbf{r}' \hat{\Psi}^\dagger(\mathbf{r},t)V_{int}(\mathbf{r}-\mathbf{r}')\hat{\Psi}(\mathbf{r})\Big)\hat{\Psi}(\mathbf{r},t) \tag{2.6.2}$$

We only consider gases in the ultracold limit where the kinetic energy is too small to allow any higher partial wave scattering $l \neq 0$; therefore collisions can be characterised by a single parameter, the s-wave scattering length a. The Born approximation allows us to replace the interaction potential, which is a poor approximation when short distances are involved $(\mathbf{r}-\mathbf{r}')$, by an effective contact interaction given by

$$V_{int}(\mathbf{r}-\mathbf{r}') = g\delta(\mathbf{r}-\mathbf{r}') \tag{2.6.3}$$

where $g = 4\pi\hbar^2 a/m$ and relates the s-wave scattering parameter to the contact interaction which gives,

$$i\hbar\frac{\partial}{\partial r}\Psi(\mathbf{r},t) = \Big(-\frac{\hbar^2}{2m}\nabla^2 + V_{ext}(\mathbf{r}) + g|\Psi(\mathbf{r},t)|^2\Big)\ \Psi(\mathbf{r},t). \tag{2.6.4}$$

This is the Gross-Pitaevskii equation [87, 88] from which the density distribution can be calculated $n(r,t) = |\Psi(\mathbf{r},t)|^2$. Confining ourselves to repulsive interactions and the condition where $N_0 \gg 1$ the $|\Psi|^2$ term will be much greater than the kinetic energy; so for sufficiently large N we can neglect the kinetic energy. This is the Thomas-Fermi approximation and the density profile can be given analytically as

$$n(\mathbf{r}) = \frac{1}{g}(\mu - V(\mathbf{r})). \tag{2.6.5}$$

The normalisation condition $\int d\mathbf{r} n(\mathbf{r}) = N$ for a 3D harmonic potential, defines the chemical potential μ as

$$\mu = \frac{\hbar\bar{\omega}}{m}\Big(\frac{15Na}{a_{ho}}\Big)^{2/5} \tag{2.6.6}$$

and the shape of the density distribution in a harmonic trap is an inverted parabola. At the Thomas Fermi radius, given as

$$R_i = a_{ho}\frac{\bar{\omega}}{\omega_i}\left(\frac{15Na}{a_{ho}}\right)^{1/5} \tag{2.6.7}$$

the density goes to zero.

In an interacting cloud at finite temperature T the interaction term also couples the thermal and condensed component. However, as the density of the thermal component is usually much lower than the condensate, this can generally be ignored. We can then use the $T = 0$ solution by replacing the total number of atoms N by only the condensed number N_0. An interacting condensate also has a different peak density compared to that of an ideal gas; this leads to a change in the critical temperature T_c as calculated by [89]

$$\frac{T_c - T_c^0}{T_c^0} = -1.32N^{1/6}\frac{a}{a_{\mathrm{ho}}} \tag{2.6.8}$$

where T_c is the critical temperature of the non-interacting gas.

2.7 Interacting Fermions

The physics of non-interacting Fermi gases described above applies to a spin polarised gas where the Pauli principle excludes s-wave interactions between particles. However, in our experiments we have a two spin state mixture and two-body interactions can be made resonant, via the Feshbach resonance, which drastically alters the behaviour. At low temperatures this allows the formation of pairs known as Cooper pairs [11] in the BCS regime and these pairs can condense to form a superfluid. Cooper pairs differ from molecules as they arise even when there is no bound state present and form via correlations in the presence of a strongly interacting Fermi sea.

We consider N fermionic atoms in the lowest hyperfine states $|F = 1/2, m_F = \pm 1/2\rangle$

which will be denoted $|1\rangle$ and $|2\rangle$ hereafter. The mixture of the two states is equal such that we have $N/2$ atoms in each state. Interactions take place through s-wave collisions, characterised by the scattering length a. We quantify the interaction strength through a dimensionless interaction parameter $1/k_F a$, where k_F is the Fermi wave vector such that $1/k_F a$ is roughly equal to the ratio between the inter-particle separation and the scattering length. By tuning the dimensionless interaction parameter we are able to access three limiting cases: $(k_F a)^{-1} \to -\infty$, $(k_F a)^{-1} \to +\infty$ and , $(k_F a)^{-1} \to 0$ corresponding to the BCS, BEC and unitary regime where the scattering length diverges to $|\infty|$, respectively. These situations are described below.

BEC limit: In this limit, the scattering length is positive $a > 0$ and $1/(k_F a) \to +\infty$. It was shown by [24] that when the scattering length is positive, a repulsive interacting Fermi gas is formed. However, if a Feshbach resonance is present, the positive scattering length will lead to the emergence of a molecular bound state in the inter-particle potential. Two fermions of opposite spin states can occupy this bound state creating a composite boson that can be well described by the standard interacting BEC theory. To form the molecules, three-body recombination must take place so that the binding energy of the molecule can be given up as the kinetic energy of the third particle. In general three-body s-wave collisions in a Fermi gas are suppressed by the Pauli principle. However, in the presence of a Feshbach resonance, it has been shown theoretically [90] that they can occur. For efficient production of molecules, the temperature of the sample must be lower than the molecule binding energy given as $E_{\rm b} \simeq -\hbar^2/ma^2$ [91]. These molecules are then formed in the highest ro-vibrational states near the Feshbach resonance. The size of these molecules is of the order of $a/2$, but as $a \to 0$ this approximation fails. Since inelastic collisions are suppressed by the Pauli principle, weakly bound molecules formed by fermions are generally more stable than those formed by two bosonic atoms [28]. This can be seen if we consider an atom-molecule collision, since relaxation into a deeply bound state by collisions is a three body process. In a two state mixture, the incoming atom must

be in the same internal state as one of the atoms contained in the composite boson. Pauli blocking will then prohibit the free atom from approaching the molecule. We can characterise the inelastic collision rates for molecule-molecule scattering and atom-molecule scattering by a loss coefficient α evaluated by [26, 17]

$$\alpha_{\rm M} \propto a^{-2.55} \qquad \text{and} \qquad \alpha_{\rm AM} \propto a^{-3.33}, \tag{2.7.1}$$

where the collisions have been described in terms of the atomic scattering length [24, 92]

$$a_{\rm M} = 0.6a \qquad \text{and} \qquad a_{\rm AM} = 1.2a. \tag{2.7.2}$$

In weakly bound molecules the two atoms are well separated and the molecule wave function is open channel dominated. We can see that an increase in the scattering length causes a decrease in the inelastic collision rate giving a more stable molecule near the Feshbach resonance.

For the weakly repulsive gas of bosonic molecules, one still requires in the Thomas-Fermi limit the interaction energy to dominate over the kinetic energy. This allows us to write the density distribution for molecules as

$$n(\mathbf{r}, T=0) = \frac{15N}{16\pi^2 R^x R^y R^z}\Big[1 - \Big(\frac{x}{R^x}\Big)^2 - \Big(\frac{y}{R^y}\Big)^2 - \Big(\frac{z}{R^z}\Big)^2\Big]. \tag{2.7.3}$$

$$R^i = \sqrt{\frac{2\mu_M}{M\omega_i^2}} = a_{ho}\frac{\bar{\omega}}{\omega_i}\left(\frac{15N_M a_M}{a_{ho}}\right)^{1/5} \tag{2.7.4}$$

where $N_M = N/2$ is the number of molecules with mass $M = 2m$ and $a_M = 0.6a$ is the molecular scattering length.

BCS limit: As the dimensionless interaction parameter $(k_f a)^{-1} \to -\infty$, we approach the BCS limit. A weak attractive interaction exists between fermions in different spin states. The formation of correlated Cooper pairs is energetically favourable even if the attraction is very small. The size of the pairs is typically on the scale of the Fermi radius, much larger than the inter-particle separation $n^{-1/3}$ [93, 94].

In contrast to the bound molecules formed on the BEC side of the Feshbach resonance the pairing gap (the energy required to break a pair) is smaller than the Fermi energy and decreases exponentially as we approach the BCS limit.

For $k_F|a| \ll 1$ the cloud is compressed due to the attractive interactions. Using standard BCS theory that describes the superconductivity in metals [39], we can solve the many-body problem at $T = 0$ and finite temperature. A first order correction is obtained to the Thomas-Fermi radius by adding the interactions as a perturbation to the non-interacting Fermi gas giving [91]

$$R^i = \sqrt{\frac{2\mu_0}{m\omega_i^2}} = R^i_{\mathrm{F}}\big(1 - \frac{256}{315\pi^2}k_{\mathrm{F}}|a|\big) \tag{2.7.5}$$

where k_F is the Fermi wave vector and R^i_F is the Fermi radius of the non-interacting gas.

Unitarity: At resonance, $(k_f a)^{-1} \to 0$, the scattering length diverges leaving the inter-particle separation $n^{1/3}$ as the only relevant length scale such that the scattering cross section $\sigma_0 = 4\pi/k^2$ becomes independent of the scattering length equation 2.2.5. In this regime the gas is said to behave in a universal manner [38]. Pairing and superfluidity can occur in these systems and the pair size is of the same order as the inter-particle spacing. Universality is expected to be the same in all strongly interacting Fermi systems and is characterised by a universal parameter β. This factor relates the properties of a unitary Fermi gas to those of an ideal gas. There have been numerous theoretical calculations of the parameter β [95, 96, 97, 98, 99, 100]. These values agree well with measurements of the β factor in both lithium [35, 101, 102, 103, 16, 34] and potassium [37] and is found to be ~ -0.58. One way to determine β is to measure the spatial extent of the atomic sample where we can obtain a density profile for the unitary gas given by [64] as

$$n(\mathbf{r}, T = 0) = \frac{8N}{\pi^2 R^x_{\mathrm{U}} R^y_{\mathrm{U}} R^z_{\mathrm{U}}}\Big[1 - \Big(\frac{x}{R^x_{\mathrm{U}}}\Big)^2 - \Big(\frac{y}{R^y_{\mathrm{U}}}\Big)^2 - \Big(\frac{z}{R^z_{\mathrm{U}}}\Big)^2\Big]^{3/2} \tag{2.7.6}$$

with $R^i_{\rm U} = (1+\beta)^{\frac{1}{4}} R^i_{\rm F}$. In this limit, the chemical potential at $T = 0$ is given by

$$\mu = (1+\beta)E_F = (1+\beta)\frac{\hbar^2}{2m}(3\pi n)^{2/3} \tag{2.7.7}$$

which has the same form as equations for non-interacting fermions.

2.8 Ideal quantum degenerate gases in 2D

In a homogeneous 2D gas the density of states is very different from the 3D case and is

$$g(\varepsilon) = \frac{Am^2}{2\pi\hbar^2} \tag{2.8.1}$$

where A is the area, and m the atomic mass. Using equations 2.4.1 and 2.4.2 for the occupation of single particle states, rewritten here for convenience

$$n(\varepsilon) = \frac{1}{\exp(\varepsilon - \mu/k_B T) \pm 1} \tag{2.8.2}$$

where the upper (lower) sign is for fermions (bosons). We can determine the total atom number by following the same prescription as in the 3D case of section 2.5. Stating just the solution gives for bosons

$$n\lambda^2_{dB} = -\ln\left(1 - \exp\frac{\mu}{k_B T}\right) \tag{2.8.3}$$

where λ^2_{dB} is the thermal de-Broglie wavelength in 2D, μ is the chemical potential, T is the temperature and n the total atom number. It is obvious from equation 2.8.3 that as $\mu \to 0$ the atom number diverges so there is no need for macroscopic occupation of the ground state to conserve particles and thus no formation of a BEC. In the next section we consider this more carefully for a trapped non-interacting gas.

2.9 Trapped quantum degenerate gases in 2D

2.9.1 Bosons

To achieve a 2D system in experiments we confine the atoms in a harmonic trap with one dimension (z) being much more tightly confined than the other two (x and y). To form a 2D Bose gas we must satisfy the criterion $k_B T, \mu << \hbar\omega_z$ where μ is the chemical potential and ω_z is the axial trap frequency of the harmonic potential. If this condition is satisfied then the particles are assumed to be contained in the ground state and to be kinematically frozen. This condition allows us to ignore the axial trapping direction in the density of states. For a dimensionality $d = 2$ in equation 2.5.3 we obtain

$$g(\varepsilon) = \frac{\varepsilon}{\hbar^2 \omega_r^2} \tag{2.9.1}$$

where ω_r is the geometric mean of the trapping frequencies $\sqrt{\omega_x \omega_y}$ in the radial direction. We can now substitute equation 2.9.1 into equation 2.5.5 setting $\mu = 0$ which we can do since $k_B T \gg \hbar\omega_r$. To simplify the integration we can substitute $x = \varepsilon / k_B T$, and use the definite integral

$$\int_0^\infty \frac{x}{\mathrm{e}^x - 1} \mathrm{d}x = \frac{\pi^2}{6}. \tag{2.9.2}$$

The solution is

$$N - N_0 = \left(\frac{k_B T}{\hbar\omega_r}\right)^2 \frac{\pi^2}{6}. \tag{2.9.3}$$

The finite size of the system imposed by the confining potential allows a macroscopic occupation of the ground state, and therefore condensation can take place. Determining the critical temperature and the condensate fraction in the two dimensional gas as previously gives

$$T_c = \sqrt{6N} \frac{\hbar\omega_r}{\pi k_B}, \tag{2.9.4}$$

and

$$N_0/N = 1 - \left(\frac{T}{T_C}\right)^2. \tag{2.9.5}$$

However, there is an important point to make about the trapped ideal 2D Bose gas. Although condensation can occur it is known to be a delicate entity [69]. If we substitute $\mu - V(x)$ where V(x) is the confining potential in equation 2.8.3 for μ in the x direction then we have $n(x)\lambda^2 = -\ln\left(1 - \exp\frac{\mu - V(x)}{k_B T}\right)$. Integrating this gives equation 2.9.4; however $n(0)_{max} = \infty$. This shows that only when the spatial density at the centre of the confined gas is infinite will condensation occur.

2.9.2 Fermions

In section 2.9.1 we have seen that the criterion for a 2D Bose gas is $k_B T, \mu << \hbar\omega_z$. A similar criterion occurs for a 2D Fermi gas where the temperature and Fermi energy $k_B T, E_F << \hbar\omega_z$, where ω_z is the axial trapping frequency. The gas is then confined to the lowest transverse harmonic oscillator state. To calculate the properties of the gas we proceed as before. Using equations 2.9.1 and 2.8.2 we can solve the integral for the total particle number and determine the two dimensional Fermi energy as

$$E_{F2D} = \sqrt{2N}\hbar\omega_r, \tag{2.9.6}$$

where N is the total atom number and ω_r is the radial trapping frequency. An important difference from the 3D case is the Fermi momentum distribution for a trapped non-interacting cloud. In three dimensions there are six degrees of freedom associated with the 3D phase space. However, in 2D the transverse dimension is frozen out and therefore the volume which the gas occupies is smaller and the gas will expand faster. To calculate the Fermi radii of a non-interacting trapped Fermi gas we can proceed as in section 2.7; replacing the 3D Fermi energy with the 2D Fermi energy. The characteristic size of the trapped Fermi gas with energy E_{F2D} in a harmonic

potential with frequencies ω_i can be determined from

$$R_F^i = \sqrt{\frac{2k_B T_F}{m\omega_i^2}}. \tag{2.9.7}$$

Substituting for E_{F2D} gives

$$R_{F2D}^i = (8N)^{1/4}\sqrt{\frac{\hbar}{m\omega_r}}\frac{\omega_r}{\omega_i} \tag{2.9.8}$$

where N is the atom number, m is the atomic mass, ω_r is the trapping frequency and $i = x, y, z$. Comparing this to the 3D non-interacting Fermi radius

$$R_{\mathrm{F3D}}^i = \sqrt{\frac{\hbar}{m\overline{\omega}}}\big(48N\big)^{1/6}\frac{\overline{\omega}}{\omega_i} \tag{2.9.9}$$

we see that the exponent of the atom number goes as $N^{1/4}$ in the 2D case, whereas in the three dimensional system it goes as $N^{1/6}$. This should allow us to observe a transition from the three dimensional regime to the two dimensional regime as we vary the atom number of the atomic sample across this transition in an experiment. Equation 2.9.8 describes the radius for the weakly confined direction of the trap. Since the cloud is in the lowest transverse oscillator state in the tightly confined direction. Here the width will be given by a Gaussian function equivalent to the harmonic oscillator length $a_z = \sqrt{\hbar/m\omega_z}$.

To find the atom number at which we crossover into the two dimensional regime of a non-interacting Fermi gas we can start by writing down explicitly the criterion for two dimensionality which is $E_F << \hbar\omega_z$. Using this condition and equation 2.9.6 gives

$$N_{crit} = \frac{1}{2}\Big(\frac{\omega_z}{\omega_r}\Big)^2 = \frac{\lambda^2}{2}, \tag{2.9.10}$$

where $\lambda = \omega_z/\omega_r$. For our experimental parameters $\omega_z/2\pi = 2.9$ kHz and $\omega_r/2\pi =$ 50 Hz this gives $N_{crit} = 1700$ atoms for the non-interacting Fermi gas.

Counting states:

Another way to determine the critical atom number for the non-interacting Fermi gas is to count the number of microstates in a harmonic oscillator with energy lower than that of the first transverse excited state. Here we simply count how many atoms it takes to fill states with energy below the first excited state. To determine the number of states with energy below the first transverse excited state we start by writing down the quantised energy spectrum with $n_z = 0$. This defines the lowest harmonic oscillator state as

$$\varepsilon = (n_x + \frac{1}{2})\hbar\omega_x + (n_y + \frac{1}{2})\hbar\omega_y + \frac{1}{2}\hbar\omega_z. \tag{2.9.11}$$

Similarly we write down the equation for when we populate the lowest energy first excited state where $n_z = 1, n_x = 0, n_y = 0$. Imposing the condition that the excited state energy is greater than the lowest state energy, $\varepsilon_1 > \varepsilon_0$, we have

$$\hbar\Big(\frac{\omega_x}{2} + \frac{\omega_y}{2} + \frac{3\omega_z}{2}\Big) > \hbar\Big[(n_x + \frac{1}{2})\omega_x + (n_y + \frac{1}{2})\omega_y + \frac{\omega_z}{2}\Big]. \tag{2.9.12}$$

Simplifying gives

$$\omega_z > \omega_x n_x + \omega_y n_y. \tag{2.9.13}$$

Rewriting equation 2.9.13 with two new variables $\lambda = \omega_z/\sqrt{\omega_x\omega_y}$ and $\alpha = \sqrt{\omega_x/\omega_y}$ we have

$$\lambda > \alpha n_x + \frac{n_y}{\alpha}. \tag{2.9.14}$$

We can place an upper limit for the two dimensional limit by replacing the inequality

$$\lambda - 1 = \alpha n_x + \frac{n_y}{\alpha}. \tag{2.9.15}$$

Fixing ω_z and counting from the ground state in both the x and y states we are able to find the number of states with energy less than the first excited state. To count the

number of states we use the summation

$$\sum_{n_x=0}^{\lambda/\alpha-1}\sum_{n_y=0}^{\alpha(\lambda-\alpha n_x-1)} 1 = \lambda\Big(\frac{\lambda-\alpha}{2}+\frac{1}{\alpha}-1\Big). \tag{2.9.16}$$

In the limit that $\alpha \to 1$ then equation 2.9.16 becomes, $N_{crit} = (\lambda^2+\lambda)/2$. Using our parameters $\omega_z/2\pi = 2.9$ kHz and $\omega_r/2\pi = 50$ Hz this gives $N_{crit} = 1830$, which is comparable to the approximate value found above.

Growth of a non-interacting Fermi gas in a pancake trap:

In the previous section we derived the value for the critical atom number, by considering how we fill the harmonic oscillator states up to the first transverse excited state. We can extend upon this idea by considering how the spatial extent of the particle density distribution changes as more and more excited states are populated. To obtain a physically intuitive picture we start by considering the change in density profile as we fill up the one dimensional harmonic oscillator and then extend this to the three dimensional case. This section is intended to provide the parameters to extract useful information from the experimental results of chapter 5 for further theoretical discussion on shell structure of a non-interacting Fermi gas in anisotropic and isotropic confinement the reader is referred to [104, 105, 106, 107] where in particular Vignolo and Minguzzi [105] discuss the confinement in any spatial dimension.

In section 2.9.2 we found that the weakly confined width of the gas in the 2D regime scaled as $N^{1/4}$ and $N^{1/6}$ in the 3D regime. If we plot the radius against the atom number there should be two different slopes; $N^{1/4}$ in the 2D regime and $N^{1/6}$ in the 3D regime. This should be most visible in the weakly interacting Fermi gas formed at 991 G.

To formulate the problem we start with the simplest case, the time independent Schrödinger equation in one dimension

$$-\frac{\hbar^2}{2m}\frac{\partial^2}{\partial x^2}\Psi(x) + V(x)\Psi(x) = E\Psi(x) \tag{2.9.17}$$

where the external potential is $V(x) = 1/2m\omega^2 x^2$ and m is the mass. Since the solution to the one dimensional harmonic oscillator is in every elementary quantum mechanics text we state only the solution for the wavefunction in terms of the spatial eigenstates with the dimensionless unit $\sqrt{\hbar/m\omega}$

$$\psi(x) = \Big(\frac{1}{\pi}\Big)^{1/4} \frac{1}{\sqrt{2^n n!}} H_n(x) \exp\Big(-\frac{x^2}{2}\Big). \tag{2.9.18}$$

In figure 2.9.1 we show the shape of the first few wave functions. Since we are

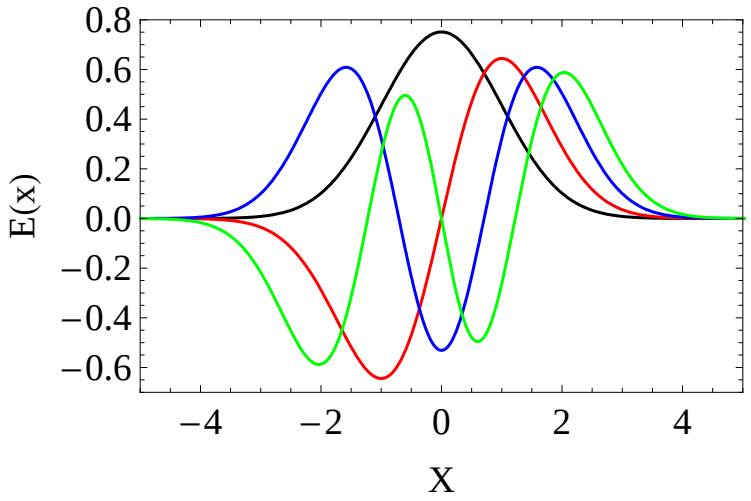

Figure 2.9.1: The first few wave functions of the quantum harmonic oscillator. $\psi_0(x)$ is the black curve, $\psi_1(x)$ is the red curve, $\psi_2(x)$ is the blue curve and $\psi_3(x)$ is the green curve.

considering fermionic particles only one can occupy each oscillator state. So for the 1D case if we have 5 atoms then 5 oscillator states are filled. By calculating the filling in a one dimensional harmonic oscillator we can show the physical effects of shell filling. We sum up each of the density profiles for a certain number of atoms, which for a non-interacting gas in one dimension can be written as

$$n(x) = \sum_n |\psi_n(x)|^2. \tag{2.9.19}$$

Using equation 2.9.19 we can calculate the density profile $n(x)$ for N particles where

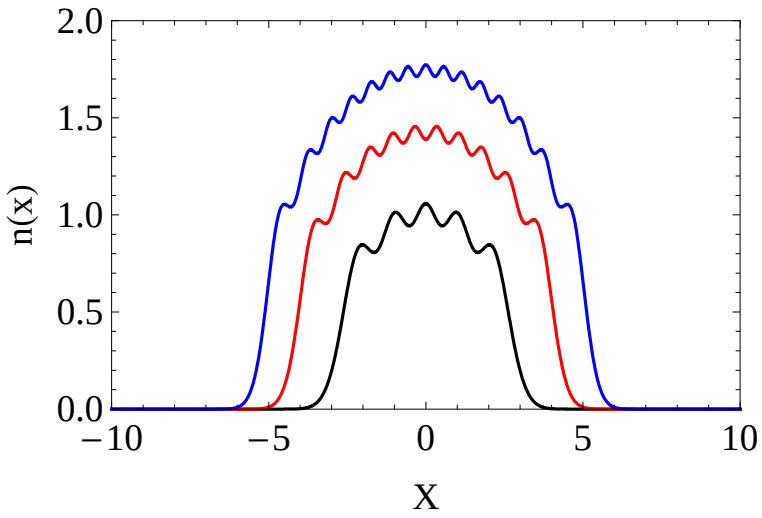

Figure 2.9.2: Particle density profiles for $N = 5$ particles (black), $N = 10$ particles (red), and $N = 15$ particles (blue) confined fermionic particles.

figure 2.9.2 shows the particle density distribution for N= 5 particles, N= 10 and N=15 atoms. We see that the fluctuations are equal to the number of atoms and as N increases the amplitude of the fluctuations decreases forming a smooth distribution at large N. By applying a Gaussian function fit to the particle density distributions we can build up a picture of how the width of the gas varies as we add more atoms. Unfortunately to calculate the values for greater N is unreasonable since we use the Hermite polynomials. For example if N where equal to 1000 atoms we would need to sum all Hermite polynomials up to 1000. In the 3D case we assume that the harmonic oscillator potential takes the form

$$V(\mathbf{r}) = \frac{m\omega^2}{2}(x^2 + y^2 + \lambda_z^2 z^2) \tag{2.9.20}$$

where m is the particle mass, ω is the trapping frequency and $\lambda_z = \lambda = 58$ for our pancake trap. For the anisotropic 3D harmonic oscillator we must now take into account the degeneracy. The degeneracy arises since the energy is the sum of n_x, n_y, and n_z and any set of quantum numbers having the same sum will represent the states of equal

energy. Writing out the eigenenergies of the harmonic oscillator potential gives

$$E = (n + (\frac{\lambda}{2} + 1))\hbar\omega, \tag{2.9.21}$$

where the shell quantum numbers are $n = n_x + n_y + \lambda n_z$ and $n_{x,y,z}$ are the usual integer quantum numbers associated with the harmonic oscillator. By restricting λ to integer values we can in turn use only integer values for shell filling which allows us to write out the degeneracies as [108]

$$g(n) = \frac{1}{2}(n+1)(2n - \lambda n + 2). \tag{2.9.22}$$

The total number of quantum states equal to the Fermi energy is given by the sum

$$S = \sum_{n=0}^{n_F} g(n) \tag{2.9.23}$$

where $n_F = E_F/\hbar\omega - 3/2$ and is the Fermi shell number. This model assumes a spin polarised Fermi gas where only one fermion per state is allowed. It is now possible to use the degeneracies to calculate the particle distributions as we populate each state. Summing up over all states and calculating the particle density distributions using the spatial wave functions

$$\psi(r) = \Big(\frac{1}{\pi}\Big)^{1/4} \frac{1}{\sqrt{2^n n!}} H_n(r) \exp\Big(-\frac{r^2}{2}\Big) \tag{2.9.24}$$

$$\psi(z) = \Big(\frac{\lambda^2}{\pi}\Big)^{1/4} \frac{1}{\sqrt{2^n n!}} H_n(\lambda z) \exp\Big(-\frac{\lambda z^2}{2}\Big) \tag{2.9.25}$$

where $r = x^2 + y^2$, $\psi(r)$ is the radial wavefunction and $\psi(z)$ is the transverse wavefunction. Figure 2.9.3 shows how the transverse width grows as a function of the atom number. We can see that until the lowest transverse state is exceeded at ~ 1700 atoms the width of the gas is constant, thereafter it scales as $N^{1/6}$.

Figure 2.9.4 shows how the radial width grows as a function of the atom number. For an atom number up to 1700 the width scales as $N^{1/4}$ above 1700 the cloud width scales

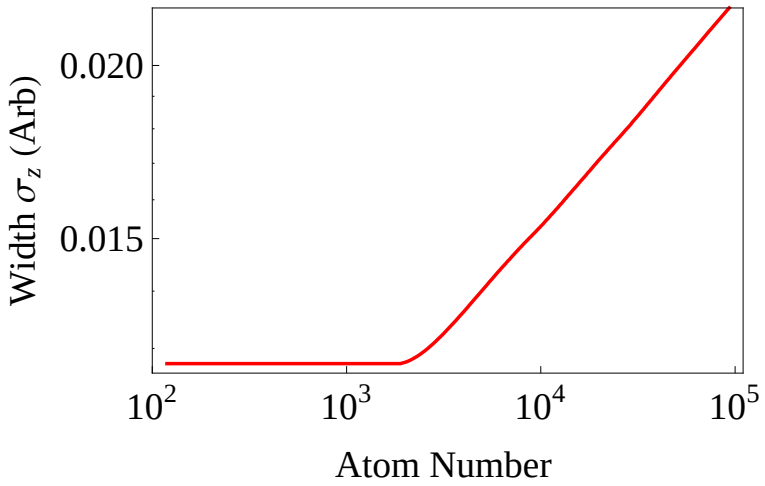

Figure 2.9.3: Axial growth of a non-interacting gas for N=10^5 atoms.

as $N^{1/6}$. It is also possible to make out structure in the curve as we start to populate the next shell. This smooths out as we add more atoms. This gives a quantitative signature for observing the crossover from 3D to 2D.

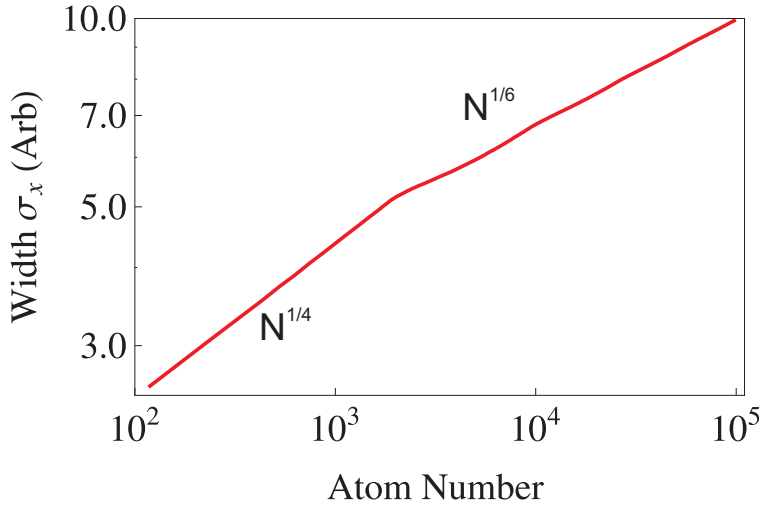

Figure 2.9.4: Radial growth of a non-interacting Fermi gas versus atom number. As each shell becomes populated structure to the curve is visible.

2.10 Scattering in 2D

Quantum scattering of atoms in two dimensions is treated in a number of texts [74], and articles [109, 110, 111]. The purpose of this section is to introduce the relevant theoretical descriptions to understand the experimental results obtained in our laboratory described in section 5.8 of this thesis. As in the three dimensional case described in section 2.2 we can describe $\Psi(\mathbf{r})$ at inter-particle distances of $r \to \infty$ as the sum of the plane wave and an asymptotic outgoing scattered circular wave

$$\Psi_{\mathbf{k}}(\mathbf{r}) = e^{i\mathbf{k}\cdot\mathbf{z}} - f(k)e^{ikr}\sqrt{\frac{i}{8\pi kr}} \tag{2.10.1}$$

where $f(k)$ is the scattering amplitude. Equation 2.10.1 differs from equation 2.2.2 by the factor $\sqrt{-8\pi k}$ due to the circular outgoing wave and the $1/\sqrt{r}$ dependence in the scattered wave is to conserve probability in 2D. As for the three dimensional scattering we wish to find the scattering amplitude and the cross section σ. The probability for the outgoing wave to cross an infinitesimal line segment $d\mathbf{a}$ per unit time is

$$\alpha(k) = v\frac{\mid f(k) \mid^2}{8\pi kr}\mathbf{d}a = v\frac{\mid f(k) \mid^2}{4k}\mathbf{d}\Omega \tag{2.10.2}$$

where $v = \frac{2\hbar k}{m}$, and is the current density (flux per unit area) of the incoming wave. This allows one to write the two dimensional cross section as

$$\sigma(k) = \mid f(k) \mid^2 /4k \tag{2.10.3}$$

which we note is the similar to the 3D scattering case. At low energies the scattering amplitude is [112, 74]

$$f(k) = \frac{4\pi}{2\ln(\frac{1}{ka_{2D}}) + i\pi} \tag{2.10.4}$$

where a_{2D} is the 2D scattering length, defined later. From equation 2.10.4 we see a contrast to the three dimensional case. Since $f(k)$ tends to 0 when $k \to 0$ the cross section $\sigma(k)$ increases to infinity. Contrasting this to the 3D system, the coupling

coefficient g_{2D} is related to the scattering amplitude and is energy dependent as described in the next section.

2.10.1 Scattering in a quasi-2D gas

To consider the g_{2D} coupling constant we impose a tight confinement potential $V_{2D}(z) = m\omega_z^2 z^2/2$ and the condition $k_B T, \mu << \hbar\omega_z$ such that the gas is frozen into the lowest transverse harmonic oscillator ground state. Petrov *et al.* [112] calculated the scattering amplitude for this case which has the general form of equation 2.10.4. To derive the relationship for the 2D geometry between a_{2D} and a_{3D} we use the expression for the bound state energy $E_B = \hbar^2/2ma_{2D}$. By equating this to the binding energy in terms of the 3D scattering length given by [112]

$$E_B = \hbar\omega_z \Big(\frac{B}{\pi}\Big) \exp\Big(-\sqrt{2\pi}\frac{a_z}{a_{3D}}\Big) \tag{2.10.5}$$

this leads to a 2D scattering length given as

$$a_{2D} = a_z \sqrt{\frac{\pi}{B}} \exp\Big(-\sqrt{\frac{\pi}{2}}\frac{a_z}{a_{3D}}\Big) \tag{2.10.6}$$

where B=0.915 and is a scaling factor [112]. Using equations 2.10.6 and 2.10.4 the low energy limit scattering amplitude is found to be

$$f(k) = \frac{4\pi}{\sqrt{2\pi}a_z/a_{3D} + \ln(B/\pi k^2 a_z^2) + i\pi} \tag{2.10.7}$$

where k is the wave vector for a Fermi gas and introduces the energy dependence. In a 3D regime where the transverse confinement is weak a_z is much larger than the s-wave scattering length a and we can neglect the imaginary and logarithmic terms, giving the scattering amplitude as

$$f(k) = \frac{\sqrt{8\pi a_{3D}}}{a_z} \equiv \tilde{g}_{2D} \ll 1 \tag{2.10.8}$$

This is now independent of energy and the dimensionless coupling constant $\tilde{g}_{2D}$ is less than one which is the situation described in section 2.11. This is a quasi-2D gas since the binary collisions can be described by the relevant 3D s-wave scattering. This regime is only relevant when $a_z \gg a_{3D}$. When $a_z \approx a_{3D}$, as in the presence of a Feshbach resonance, the logarithmic term in equation 2.10.7 becomes significant. At this point a pole can exist leading to a confinement induced resonance for certain values of the harmonic oscillator length a_z.

In the regime where $a_z \leq a_{3D}$ we need to use the full coupling constant

$$g_{2D} = \frac{4\pi\hbar^2}{m} \frac{1}{\sqrt{2\pi}a_z/a_{3D} + \ln(B\hbar\omega_z/\pi\varepsilon)}. \tag{2.10.9}$$

A pole in this quantity will occur when the denominator of equation 2.10.9 is zero. Solving for the 3D scattering length a_{3D} gives

$$a_{3D} = -\frac{\sqrt{2\pi}a_z}{\ln(\frac{B\hbar\omega_z}{\pi\varepsilon})} \tag{2.10.10}$$

where a_z is the harmonic oscillator length, and ω_z is the axial trapping frequency and $\varepsilon \sim E_F$ in a Fermi gas. For our initial conditions of trap frequencies of $\omega_z/2\pi =$ 2951 Hz, $\omega_y/2\pi = 57$ Hz and $\omega_x/2\pi = 45$ Hz we should see a confinement induced resonance at approximately 814 G. Increasing the frequency or decreasing the frequency will allow us to shift the pole above or below this position.

2.11 Interacting 2D quantum degenerate gas

As stated in the introduction it is possible to achieve superfluidity in 2D systems even if a BEC only exists at $T = 0$. In 2D systems finite temperature phase fluctuations play a key role and can lead to a quasi-condensate. A quasi-condensate can be considered as being broken into individual condensates which are coherent within themselves but show no global coherence. Further cooling can cause these quasi-condensates to merge

where vortices that form at boundaries pair up leading to the BKT superfluid.

This section describes the trapped interacting Bose gas and the differences to the density distribution compared to the 3D case. For completeness we summarise two major experimental works that have been reported on the Berzinskii, Kosterlitz and Thouless (BKT) [44, 45] superfluid transition and the theoretical work on fermions.

Bosons:

Introduction of a trapping potential stabilises the atom cloud against thermal phase fluctuations that occur in the homogeneous cloud, since it introduces a finite size to the system. This allows a true BEC to form even for finite temperatures as described in section 2.9.1. In the radial direction of the quasi-2D cloud, where $r = \sqrt{x^2 + y^2}$, it is valid to use the Thomas-Fermi approach as in section 2.5. The 2D density profile is thus

$$n_0(r) = \frac{\mu}{g}\Big(1 - \frac{r^2}{R_r^2}\Big) \tag{2.11.1}$$

where $R_r = \sqrt{2\mu/m\omega_r^2}$ is the Thomas Fermi radius in the xy plane and μ is the chemical potential. To determine the chemical potential in the Thomas-Fermi limit we use $N_0 = \int n_0(r)dr$ giving

$$\mu = 2\sqrt{N g'_{2D}}\hbar\omega_r \tag{2.11.2}$$

where N is the number of atoms and ω_r is the mean trapping frequency in the radial direction. We also introduce the dimensionless coupling constant g'_{2D}

$$g'_{2D} = \frac{m\tilde{g}_{2D}}{4\pi\hbar^2} \tag{2.11.3}$$

where $\tilde{g}_{2D}$ is defined in equation 2.10.8. Using equation 2.11.2 and the Thomas Fermi radius for the cloud in the xy plane we can obtain the extent of the radius in the 2D regime similar to the trapped non-interacting Fermi gas this gives

$$R_r = \Big(\frac{128}{\pi}\Big)^{1/8}\Big(\frac{N a a_r^4}{a_z}\Big)^{1/4} \tag{2.11.4}$$

where a is the s-wave scattering length, and a_r is the harmonic oscillator length in the radial direction. It can be seen from equation 2.11.4 that the width in the BEC limit will also follow a $N^{1/4}$ scaling allowing a measurable parameter for the crossover from 3D to 2D on the BEC side of the Feshbach resonance.

The 2D interacting Bose and Fermi gas have an interesting peculiarity, the BKT transition. The purpose of the following discussion is to summarise some of the work that has taken place in observing the transition. Experimentally the BKT transition was first characterised by Bishop and Reppy [46]. Characterisation of the superfluid transition for a two dimensional film of ^{4}He adsorbed onto a Mylar substrate was reported. Observation of an abrupt variation in the superfluid signal at the transition temperature was seen as a narrow peak in the superfluid dissipation. The peak was noted to be a, "*fundamental difference between the onset phenomena in two- and three-dimensional superfluids*". The observations showed good agreement with the predictions of Kosterlitz-Thouless theory. For trapped Bose gases their have been two main experiments associated with the BKT transition reported by Hadzibabic *et al.* [55] and Cladè *et al.* [53].

Hadzibabic *et al.* prepared a 3D quantum degenerate cloud of ^{87}Rb in a cylindrically symmetric trap. To transfer to the 2D regime they apply a blue detuned 532 nm, optical lattice with periodic spacing of 3μm. This splits the 3D cloud up into independent 2D clouds. These separated clouds are then released and after sometime expand and overlap producing a matter-wave interference pattern. This is then imaged on a CCD camera by a resonant laser pulse. To explore different temperature regimes in the 2D gas, they vary the final evaporation point of the 3D degenerate gas before applying the optical lattice. In this way it is possible to study the temperature regime where condensation occurs through to a fully condensed gas in 3D. There are two main experimental results reported. First is the observation of quasi-2D long range order and secondly the proliferation of free vortices that occur above the BKT transition temperature. To observe the effects of long range order they measure the contrast of

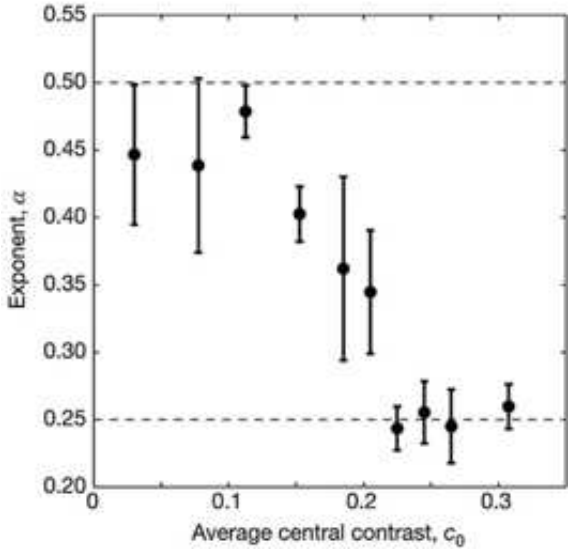

Figure 2.11.1: The decaying exponent α versus the fringe contrast. This shows the emergence of the long range order in a quasi-2D Bose gas. Reprinted by permission from Macmillan Publishers Ltd: Nature, [55], copyright 2006.

fringes in the matter-wave interference pattern where the results are summarised in figure 2.11.1.

To determine the long range order they partially integrate the interference pattern over interaction lengths L_x and L_y in the x and y directions, respectively. They state that the contrast will then be proportional to $1/(L_x)^{2\alpha}$ and the exponent α will indicate the decay of coherence and the transition to long range coherence. The x-axis shows the contrast of the central part of the cloud rather than the full extent since the cloud is not uniform in this direction. In the high temperature regime the contrast is $\sim$13% and α is about 0.5. The exponent then falls of rapidly as the temperature is reduced and plateaus. This indicates two different regimes for high and low temperature. From the wings of the cloud they infer a temperature and density at a contrast of 0.15 to be 290 nK which gives a thermal de Broglie wavelength of 0.3 μm. This gives a phase space density of $n_s\lambda^2 = 6 \pm 2$ where the BKT transition occurs at $n_s\lambda^2 = 4$. This result is interpreted as showing that below the BKT transition a superfluid state is accessed since long range order emerges. The observation of vortices is shown in figure 2.11.2 again they measure the contrast of the fringes where the dislocations in the interference

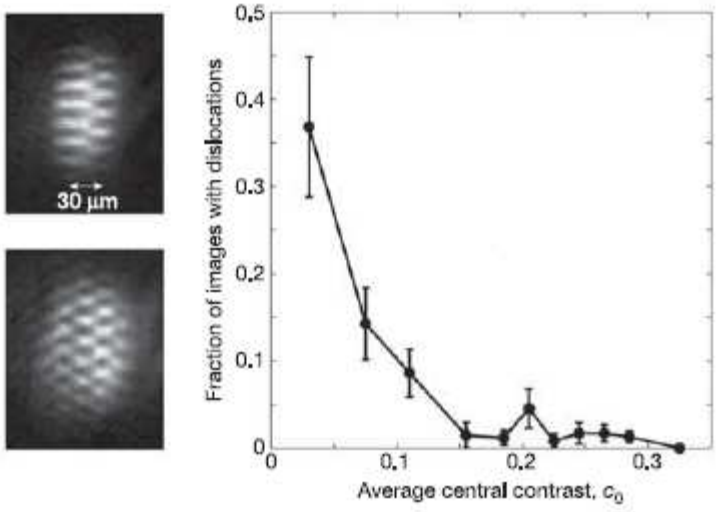

Figure 2.11.2: Fringe dislocations in a quasi 2D gas attributed to vortices in the thermal cloud. Reprinted by permission from Macmillan Publishers Ltd: Nature, [55] copyright 2006.

pattern are attributed to free vortices in the cloud at high temperature. They observe that the onset of the dislocations is also associated with a change in α and the loss of long range order. With both of these main results they are able provide evidence of the BKT transition.

The work reported by Cladè *et al.* [53] reports experimental evidence of the quasi-condensate phase. Their experiment uses ^{23}Na atoms trapped in an attractive optical dipole potential formed by a Gaussian beam that is focussed in one dimension to form the anisotropic light sheet potential. To form a quasi-2D gas of bosons they first confine the atoms in a magnetic trap and cool them to temperatures above the critical temperature for BEC to occur in a 3D system. They then transfer the atoms into the optical dipole trap and cool the atoms further to a fixed trap depth where all experiments are performed such that the temperature remains the same. Absorption imaging is used along the vertical direction after some expansion time to obtain the 2D density profile. The inset profiles of figure 2.11.3 shows the three different regimes that are reported in the paper. The first is the thermal phase, in which the spatial distribution of the cloud is well described by a Gaussian distribution. The other two

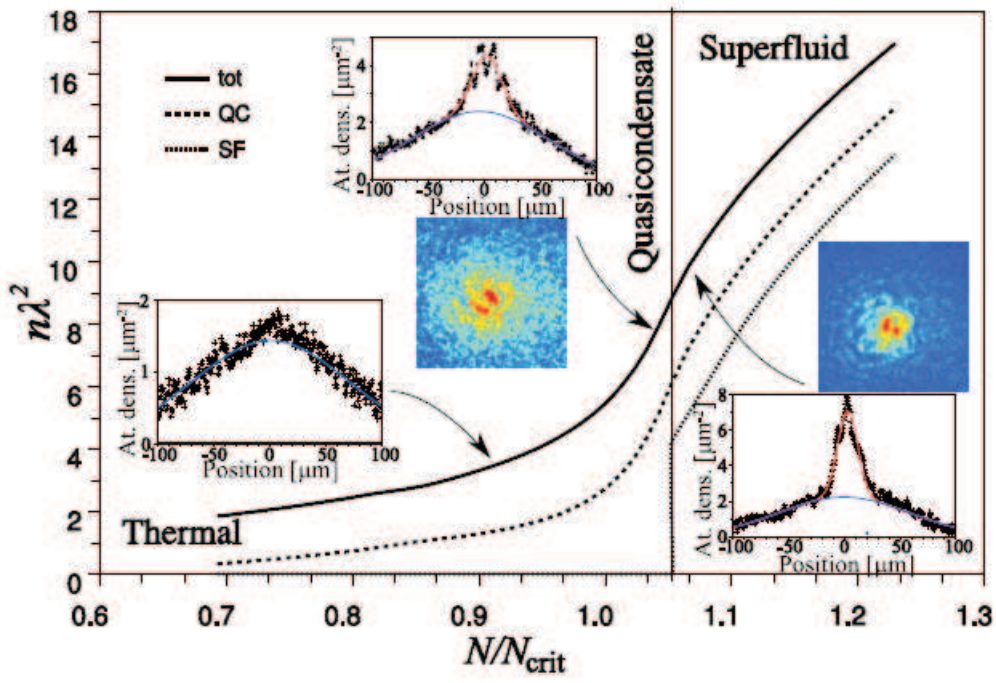

Figure 2.11.3: Absorption images and their density profiles for different values of N after 5 ms expansion time. Reprinted with permission from [53]. Copyright (2009).

pictures are for the same temperature but different atom numbers. Both images show density fluctuations around a bimodal peak. The fluctuations of the cloud are only seen in the TOF images. The lower atom number is in the quasi-condensate regime and as the atom number and therefore density is raised it crosses over into a combination of normal and superfluid states. However, the superfluid cannot be seen at 5 ms time of flight, but after 10 ms TOF, they observe a trimodal peak, which may be attributed to the three distinct regimes of thermal, quasi-condensate and superfluid. To support evidence of a BKT transition they plot the width of the bimodal distribution (the insets in figure 2.11.3) as a function of density shown in figure 2.11.4. Initially they see the width reduce as the cloud becomes more coherent, but reaches a minimum, and then starts to increase again. The minimum coincides with the theoretical value for the BKT transition.

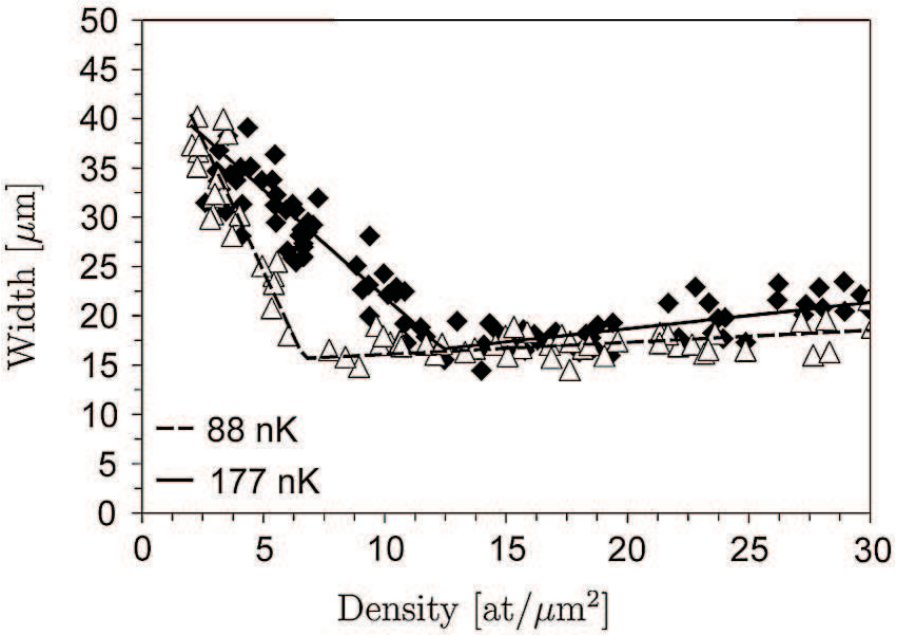

Figure 2.11.4: Determination of the BKT transition point is found by fitting the narrowest part of the cloud shown in figure 2.11.3 and plotting the width versus the density of the cloud. The intersection of the two slopes indicates the BKT transition point. Reprinted with permission from [53]. Copyright (2009).

Fermions:

The BKT transition is also expected for a Fermi gas near the Feshbach resonance. The theory for a strongly interacting quasi-2D Fermi gas is sparce since it is extremely difficult. Some theoretical work on the BEC-BCS crossover in a quasi-2D Fermi gas has been discussed in [113, 114, 115, 116]. However, to the authors knowledge the only article that describes the BKT transition in an interacting Fermi gas is by Zhang *et al.* [117]. In the following section we summarise the results of this paper.

Zhang *et al.* [117] use a Hamiltonian previously derived by Kestner *et al.* [118] and study the superfluid transition temperature across a Feshbach resonance for a trapped quasi-2D Fermi gas for both ^{6}Li and ^{40}K. The main result shows that the BKT transition evolves from zero temperature in the limiting BCS case to a constant value in the BEC limit. Below we summarise their findings.

Considering only the uniform quasi-2D Fermi gas, i.e., with no radial trapping

potential they find that the superfluid transition for the BKT temperature T_{BKT} evolves continuously across the resonance. Where on the BEC side of the resonance (where the fermions form weakly bound molecules) it increases to a limiting value of $0.075E_F$ as shown in figure 2.11.5. The figure shows the variation of the transition temperature across the Feshbach resonance for different ratios of E_F/ω_z. First we note the point at which the BEC limit is reached is on the BCS side of the Feshbach resonance. This is due to the existence of a two body bound state irrespective of the sign of the scattering length in a lower dimensional system. This condition is realised as long as $E_b \gg E_F$. As the ratio $E_F/\omega_z \to 1$ the dimensionality of the gas will approach the 3D limit. At that point we will recover the usual BEC-BCS crossover physics and no bound state will occur on the BCS side of the resonance.

By imposing a potential in the radial direction $V(r) = m\omega_\perp r^2/2$, where $\omega_\perp = \sqrt{\omega_x\omega_y}$, it is possible to consider a trapped quasi-2D Fermi gas. Calculation of the

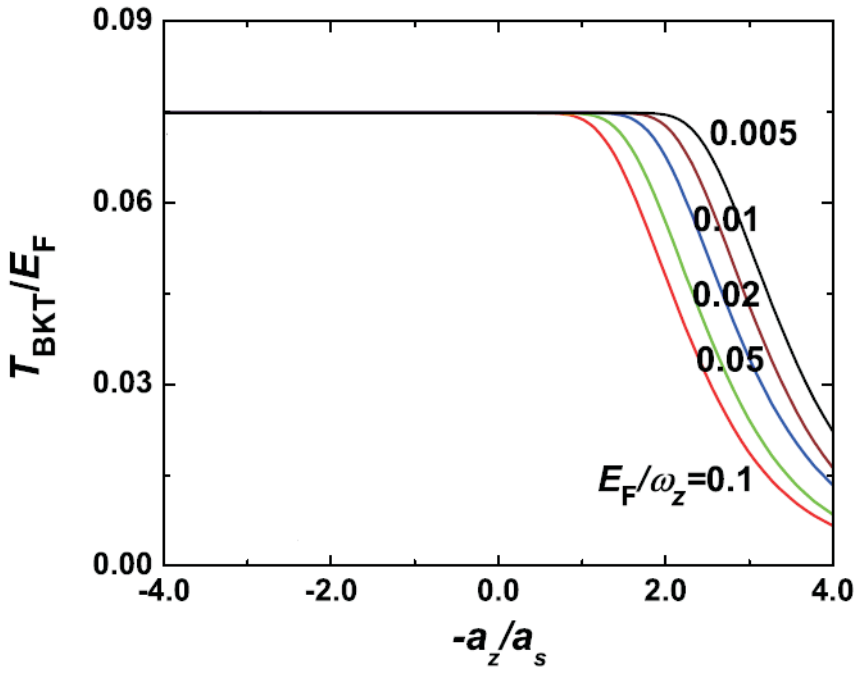

Figure 2.11.5: The BKT transition temperature T_{BKT} for a uniform quasi-2D Fermi gas across the Feshbach resonance for different values of E_F/ω_z. This figure is reproduced from [117].

trapped atom and superfluid density distributions in the radial direction are performed by using the local density approximation and the position dependent chemical potential $\mu(r) = \mu_0 - V_\perp(r)$ where μ_0 is the chemical potential at the centre of the trap. Fixing the total particle number $N = 2\pi \int_0^\infty n(r) r dr$; it is possible to show that by varying the temperature, a superfluid does not exist at high temperature. As the temperature is lowered the density builds and a superfluid appears from the centre of the trap. This extends out over the whole radius as T decreases further. At temperatures between the high temperature values and T=0, there is an abrupt discontinuity in the superfluid density; characteristic of the BKT type phase transition.

2.12 Summary

This chapter begins by revising the relevant collisions and interactions for a 3D non-interacting and interacting quantum degenerate gas. This leads us into a discussion about the relevant zero temperature properties of a harmonically trapped degenerate gas. The main objective is to give familiarity to the subject matter rather than a comprehensive description. We then turn our attention to a 2D quantum degenerate gas. Here we focus on the relevant subject matter that allows useful extraction of properties contained in the thesis. We also introduce the topic of scattering in 2D as the results in section 5.8 indicate the existence of a confinement induced resonance. For completeness we review some of the experimental results of the BKT transition obtained in Bose gases and the theory that has been developed for an interacting 2D Fermi gas.

Chapter 3

Experimental Description

This chapter briefly details our experimental apparatus used to create ultracold ^{6}Li gases. Since the first thesis [81] to come out of our lab several modifications to the experiment have been made, including the addition of a tapered amplifier and re-configuration of the laser locking system. In addition to this we installed an offset locking system for imaging at high magnetic fields as described in [82]. However, the vacuum system, coils and many other parts of the experiment remain the same. Only a brief description of those parts is provided. A more in depth description of the system can be found in [81].

3.1 Vacuum

Obtaining ultra cold quantum degenerate gases requires an ultra high vacuum (UHV) environment to provide good thermal isolation from the surroundings and to avoid collisions with hot back ground gas molecules. Our UHV system consists of two main chambers shown in figure 3.1.1 as the left and right pumping chambers. These are separated into five sections as described below.

Lithium is a solid at room temperature so to acquire a significant vapor pressure we heat, in an oven, 1 g of 95% enriched ^{6}Li to 420 °C, well above the melting point of 181 °C. The oven consists of a steel tube housing the lithium, connected to the oven pumping chamber via a 10 cm long tube with a diameter of 4.5 mm. This collimates the atomic beam and maintains the required pressure difference between the oven and pumping chamber. Inside the collimation tube a wire mesh is placed to recirculate some of the lithium increasing the lifetime of one piece. Lithium reacts with many different materials, so to seal the vacuum system, where the largest amount of lithium is found, nickel gaskets are used instead of copper as this reacts less. Around the outer tube of the oven heating wire is wound and the system is embedded in two cement blocks which help to reduce power consumption.

The collimation tube is connected to a six way cross. Attached to this are the titanium sublimation pump (TSP), a home made mechanical shutter, a 50 l/s Varian ion pump and a turbo molecular pump. Stress reduction is provided by an angled steel valve connected to the turbo pump via a bellow. During the initial pumping and baking out stages the turbo molecular pump is used since the other pumps are inefficient at low pressure. An all-metal in-line valve is attached to the exit of the six way cross connecting the Zeeman slowing region with the oven pumping chamber. This also serves to isolate the two chambers if new lithium is needed.

The Zeeman slower acts as a low conductance tube providing additional differential pumping between the low vacuum end and the UHV end of the system. It consists of four sections; two are 10 cm long and two are 5 cm long each increasing in diameter from 4 mm to 10 mm in increments of 2 mm. The exit is then connected directly to the first metal-to-glass transition of the glass cell as can be seen in figure 3.1.1b.

The science takes place within the glass cell. The dimensions are 12 x 3 x 3 cm^2, it has an anti-reflection coating for both 1030 and 670 nm light on the exterior. There are two metal to glass transitions at either end, one connected to the Zeeman slowing coil and the other to an edge welded bellow which reduces stress on the glass cell. This

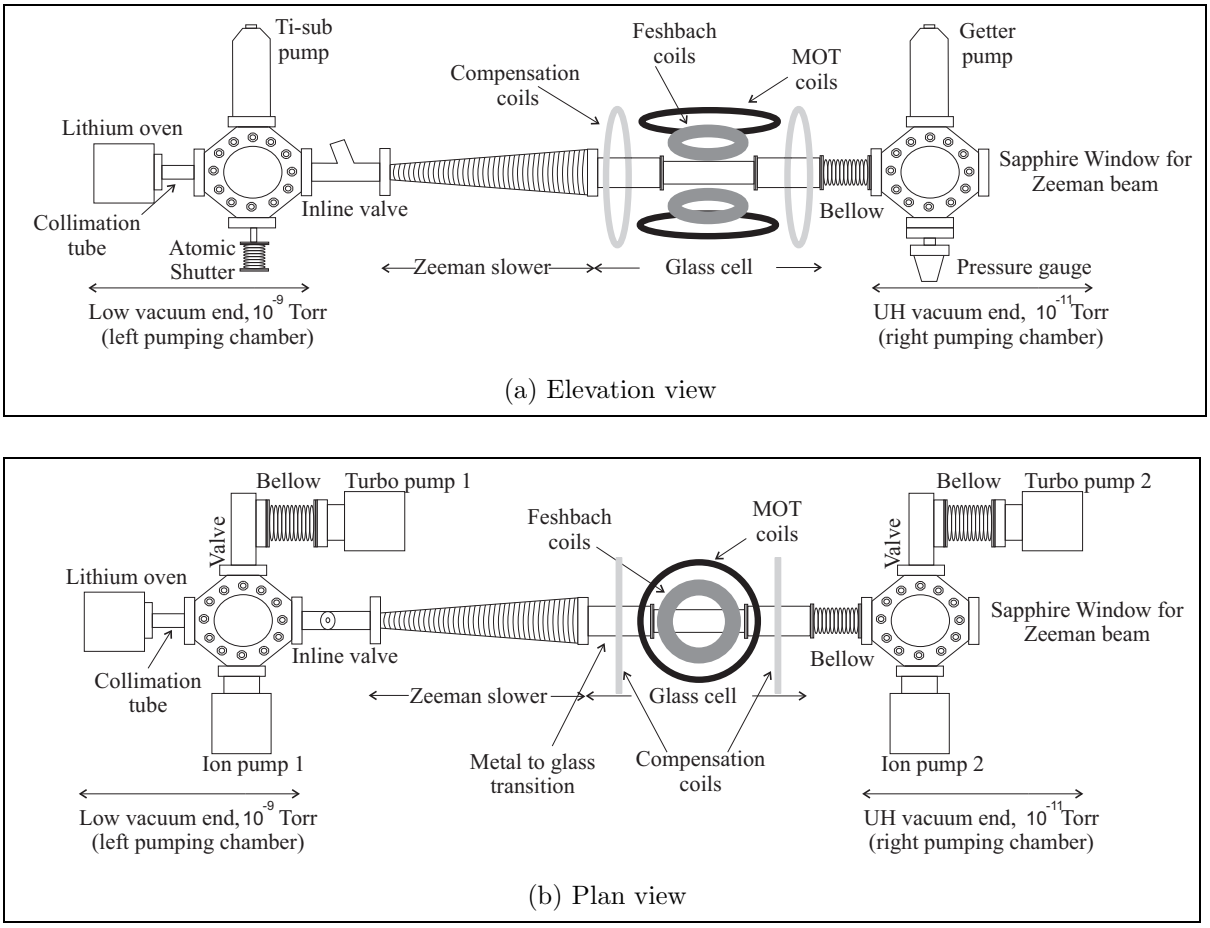

Figure 3.1.1: The two schematics show (a) the elevation view and (b) the plan view of the vacuum set-up [82].

is then connected to a six way cross and the final pumping chamber.

Attached to the six way cross is a non-evaporative getter pump, another 50 l/s Varian ion pump which maintains the UHV, another molecular turbo pump, which is used during the initial pumping and baking-out stages, a pressure gauge and a sapphire view port, which seals the overall system. The view port also acts as the entrance window for the Zeeman slowing beam. Not described here is the baking out process and how we obtain UHV. An extensive description of these procedures can be found in [81, 82].

3.2 Laser system

This section describes the laser sources required to produce the magneto-optical trap (MOT) beams and the absorption imaging beams. We start by describing how we generate stable laser frequencies through saturation absorption spectroscopy in a lithium vapour cell, then from this reference point describe the production of different laser frequencies required to trap and image the atomic sample.

A schematic of the lithium vapour cell is shown in figure 3.2.1. The cell consists of a 30 cm stainless steel crossed tube connected to two flexible bellows at either end with glass view ports, which give optical access to the pump and probe beams. The cardinal part is heated by heating tape, wound around the outer tube, to 350 °C increasing the vapour pressure inside the cell. Sub-Doppler absorption spectroscopy is used to produce

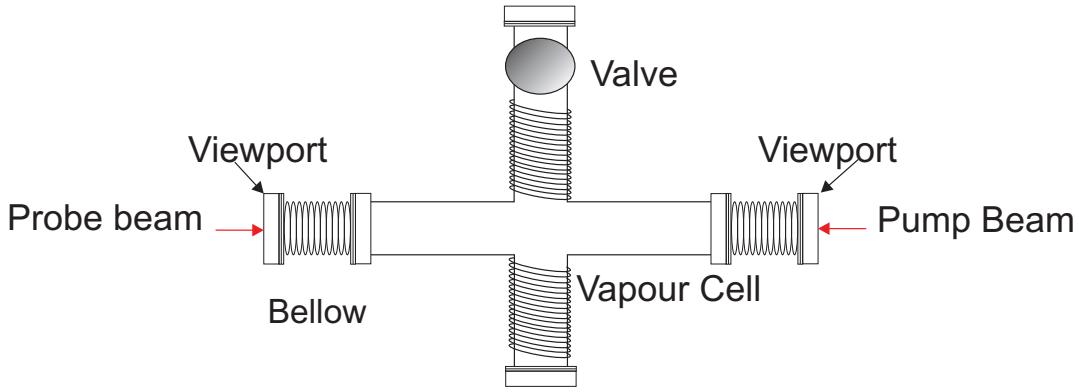

Figure 3.2.1: Saturation spectroscopy cell

a stable reference frequency to which the lasers can be locked. Modulating the pump beam with an acousto-optic modulator (AOM) and then observing the probe intensity transmitted at that particular frequency using a lock-in amplifier provides an error signal with a zero crossing at the top of the saturation absorption peak. An external cavity diode laser (ECDL)[1] is frequency stabilised by passing first through an AOM red-detuned by 206 MHz,

[1] 15 mW Toptica DL 100, $\lambda = 671$ nm

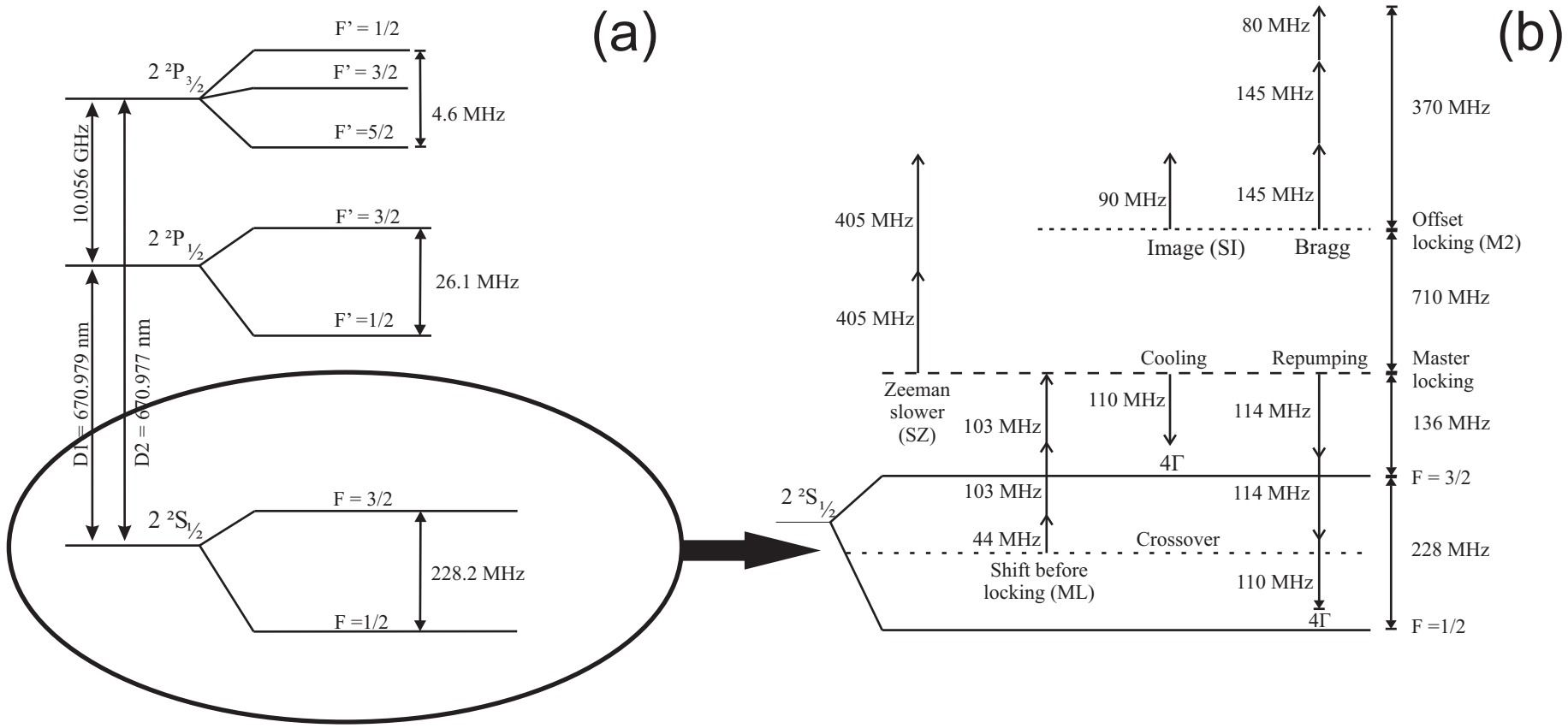

Figure 3.2.2: (a) Energy level diagram (b) Laser locking scheme for generating the frequencies used in the experiment.

then through the lithium cell and further red-shifted 44 MHz from the crossover peak of the two lowest hyperfine states of ^{6}Li shown in figure 3.2.2. This final AOM has an external modulation of 250 kHz to provide the error signal after lock in detection. The probe intensity is then observed at a photodiode. Using a lock-in amplifier the derivative of this signal is obtained and the laser is locked to the D2 transition of ^{6}Li.

It was previously reported [81] that the line width of the ECDL was approximately 1 MHz. Since then the Toptica controllers have been replaced with ECDL controllers from MOG Laboratories Pty Ltd (MOGlabs), model DLC-202 used to improve the linewidth with minimal cost. The controllers directly replace the Toptica supplies and lock-in amplifiers, with a few simple modifications. First we replaced the laser head board on the Toptica ECDL 100 with one provided with our new controllers. Secondly we added the 250 kHz modulation to the AOM as stated above, where previously the applied modulation could only be 30 kHz. We now obtain line widths of approximately 400 kHz found by beating two independent lasers and measuring the width of the resultant beat note on a spectrum analyser. From this reference point, frequencies for re-pumping light, trapping light, Zeeman light and image offset locking are generated.

3.2.1 Generation of the six-beam MOT

The laser beams used for the MOT come from a tapered amplifier (BoosTA from Toptica, 670 nm, 0.5 W). The Boosta output is sent down a polarisation maintaining fibre then expanded to a $1/e^2$ waist of 25 mm and split into 6 separate circularly polarised beams. The construction of the optics is shown in figure 3.2.3. The laser frequency is produced as described in the previous section. The ECDL does not produce sufficient power for the MOT; therefore amplification of the ECDL is implemented through a Master-Slave configuration, laser S1[2].

[2]In both S1 and SZ we use opnext HL6545MG, $\lambda = 660$ nm 120 mW diodes

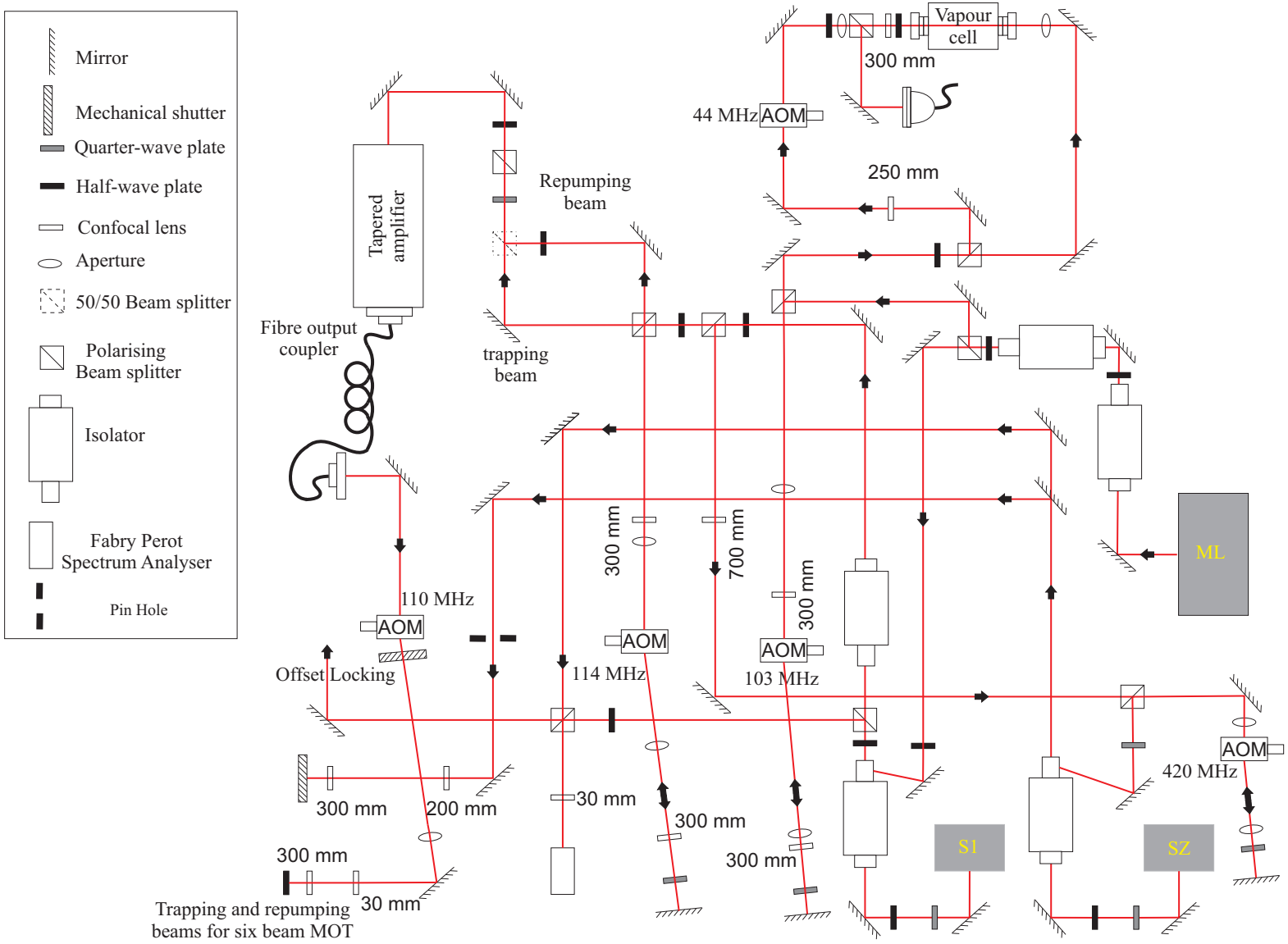

Figure 3.2.3: Optical set up for creating MOT and Zeeman slower beams.

This in turn injection locks the slave laser SZ used for the Zeeman slowing beam, and produces the laser light for offset locking, re-pump and trapping light.

Re-pump and trapping light: Light at both re-pump and trapping frequency are coupled into the tapered amplifier directly from laser S1. To produce the re-pump light red-detuning of laser S1 by 228 MHz is required. This is achieved using an acousto-optic modulator (AOM) at 114 MHz in double pass configuration on part of the light from S1. Recombination with the trapping beam takes place at a 50/50 beam splitter cube, where the power is approximately 6 mW in each beam before coupling into the tapered amplifier. This is coupled to a single mode polarisation maintaining fibre, focussed into an AOM whose frequency is 110 MHz. The combined beams are expanded using a telescopic arrangement of 30 and 300 mm focal length lenses, changing the beam diameter from 2.5 mm to 25 mm. The beams are then split into six, with approximately 16 mW power in each beam.

Zeeman Slower: Red detuning of 810 MHz from the MOT transition is needed for Zeeman slowing. This is achieved by using an AOM at 405 MHz in double pass configuration on part of the light from S1. With no other manipulation of SZ, MOT loading can be approximately 60 seconds. However, similar to the group at Innsbruck [119], an empirically determined frequency modulation of the Zeeman slowing diode laser current at 120 MHz enhances the Zeeman slowed flux by a factor of two and reduces the MOT loading to 30 seconds. The broadening of the laser line width may lead to the effective broadening of the transition linewidth. The atoms would be resonant with the laser beam for a longer period making the slowing more effective. Due to an inhomogeneous beam we focus the light from SZ through a 300 μm pin hole to remove the higher spatial frequencies. This is then re-collimated to 25 mm diameter using a telescopic arrangement of 200 and 300 mm focal length lenses. Finally the beam is focussed at the oven by a 1000 mm focal length lens placed at the sapphire view port.

3.2.2 Offset locking

Much of the interesting physics that we wish to study takes place in the strongly interacting regime achievable at high magnetic fields. For this reason, an imaging laser denoted M2 in figure 3.2.4 with a large and easily tunable locking frequency was required. This can be achieved using an offset locking scheme similar to that described by U. Schünemann *et al.* [120] and a version of this was implemented into our system. Using a second external cavity diode laser (ECDL) M2 in figure 3.2.4, light from the master laser M1 is allowed to beat with it on a fast photo-diode. The output signal is amplified and mixed with a Voltage Controlled Oscillator (VCO) with tunable frequency 600-1200 MHz. Frequencies ≥140 MHz are filtered out and the signal is amplified further. Splitting the signal in two and introducing a frequency dependent

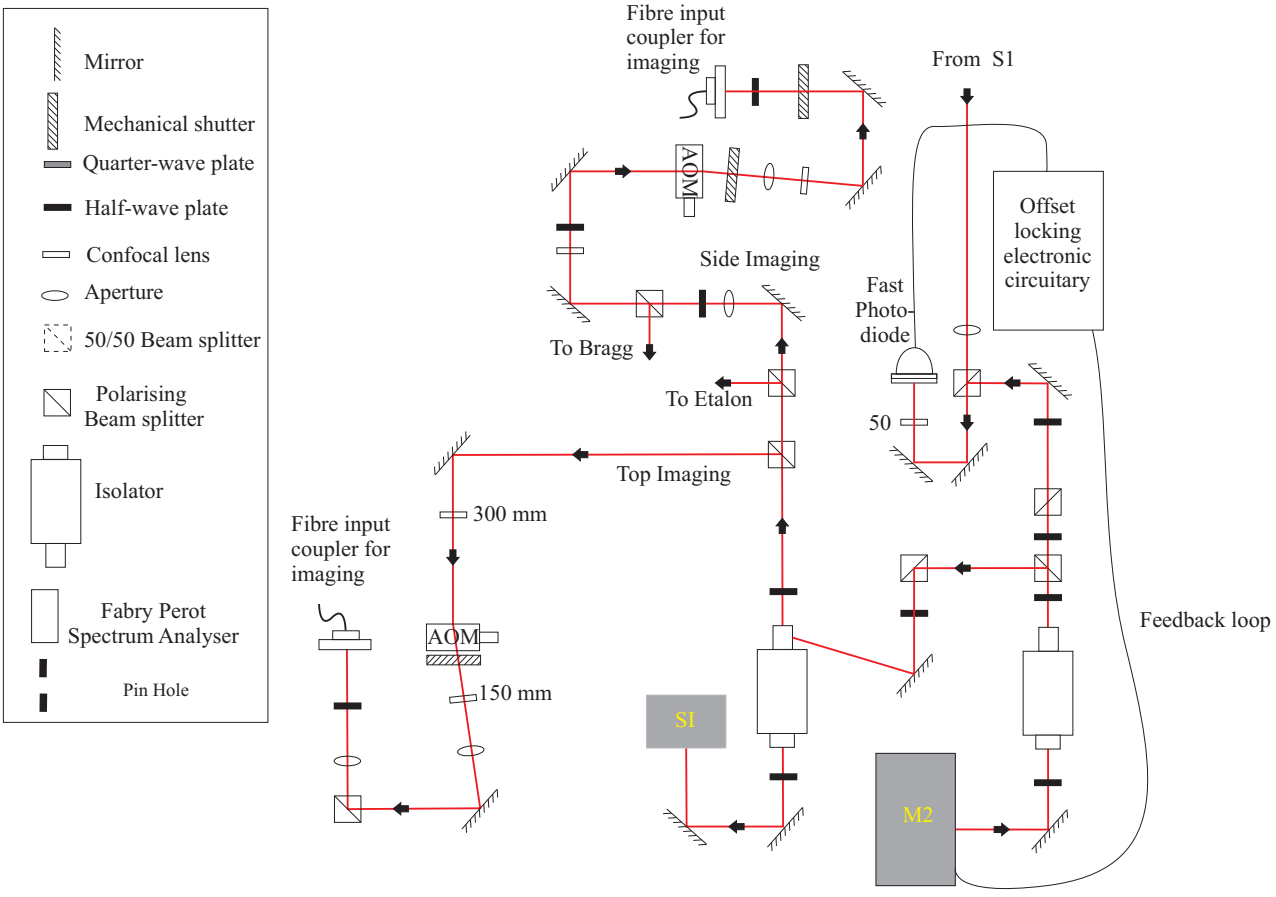

Figure 3.2.4: Schematic for offset locking and side and top imaging.

phase shift of one by passing it through a 5 m cable allows the two signals to beat together at a phase detector. The resulting output is used as an error signal for the locking of M2 controlled via a second MOGlabs controller. We now have the flexibility required to image at varying magnetic fields over a range of 650-1000 G by varying the operating frequency of the VCO. Since M2 is only 9 mW amplification of the beam is achieved by injection locking SI with M2. The beam is split in two, one is frequency shifted a further 90 MHz and used for absorption imaging from either the top or side and the other produces the beams for Bragg spectroscopy.

3.3 Absorption imaging

To obtain physical information such as the density, width, and position of the atomic cloud, absorption imaging is employed [65]. The modus operandi is to irradiate the atomic cloud with resonant laser light, and image the shadow of the cloud on a CCD camera. A schematic of the two imaging systems that we use is shown in figure 3.3.1. Integrating across the cloud in the direction of the propagating laser, $n(x,y) = \int n(x,y,z)dz$, a two dimensional density profile can be obtained. A second reference image is taken without the atomic cloud present. A third image is also taken at the beginning of the experimental run to measure the dark counts of the CCD during an image. This dark image is then subtracted from all subsequent images as it does not change over the course of an experimental sequence. Depending on whether top or side imaging is being used, the timing for the second image occurs 270 or 50 ms, respectively, after the first image. The intensities in each image differ after passing through the science cell. Image 1 is denoted by $I(x,y)$ and image 2 by $I_0(x,y)$ and the column density is derived through the relationship

$$\frac{I(x,y)}{I_o(x,y)} = e^{-\sigma \int n(x,y,z)\ dz}, \tag{3.3.1}$$

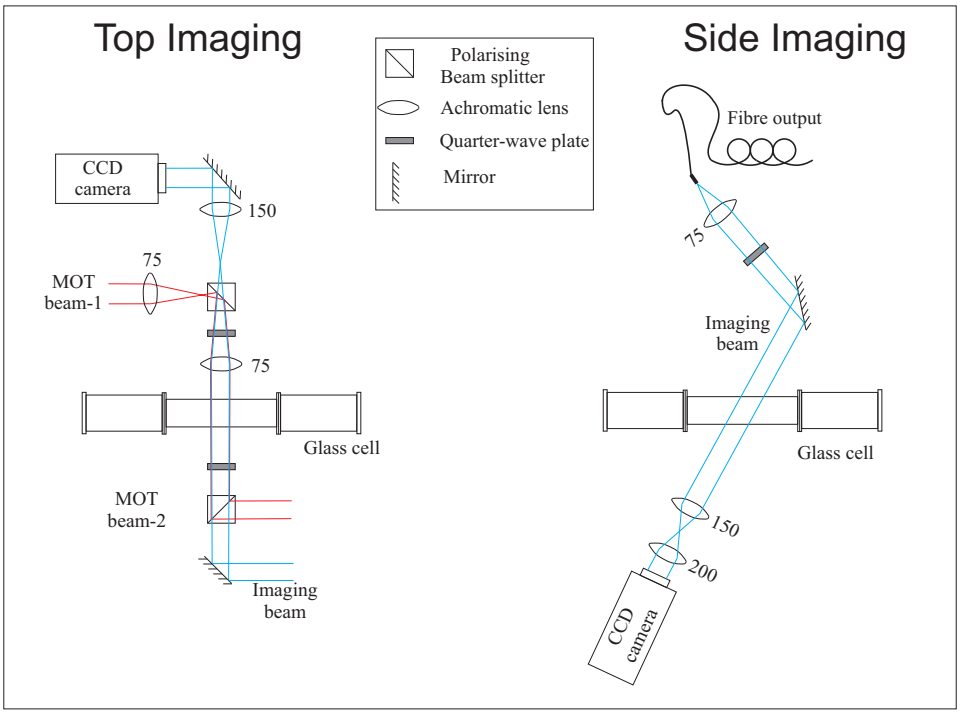

Figure 3.3.1: Schematic of side and top imaging.

where σ is the absorption cross section, and depends on the orientation of our imaging as discussed next.

Top Imaging: As stated above there are two imaging orientations in our system; the application of the imaging beam is the same, but there are some subtle differences that need to be taken into account depending on the orientation. The top imaging beam is derived from laser S2 as described in section 3.2.1, and it is then passed through an optical fibre. At the output the beam is collimated to a diameter of 20 mm by a 60 mm focal length lens. The beam propagates along the same path as the vertical MOT beams, shown in figure 3.3.1a, which are parallel to the quantization axis of the magnetic fields generated by the Feshbach coils. The presence of the large magnetic field removes the degeneracy of the excited state generating an ideal two level transition We can now use circularly polarised light and drive the closed optical transition between the states $\mid 2S_{\frac{1}{2}}, m = -1/2\rangle$ and

$|\, 2P_{\frac{3}{2}}, m = -3/2\rangle$ shown in figure 3.2.2. The resonant cross section is

$$\sigma_o = \frac{3\lambda^2}{2\pi}. \tag{3.3.2}$$

Using two achromatic 50 mm diameter lenses with focal lengths of 75 mm and 150 mm the atomic cloud is imaged onto the CCD camera[3] with a magnification of two, where each pixel has a size of 6.45 μm^2, corresponding to 3.225 μm^2 after magnification. Imaging along the magnetic field improves the contrast of the images by maximising the absorption cross section. However, due to combining the paths of the imaging and vertical MOT beams, the images are degraded. Since each extra element such as polarising beam splitting cubes, wave plates and mirrors introduces degradation of the probe beam wavefronts and within the beam splitting cubes multiple reflections can occur and produce interference fringes in the image. To overcome this a side imaging system was established using a much simpler set-up.

Side Imaging: The beam used for side imaging is also derived from laser S2 as previously described. Once passed through an optical fibre it is collimated to approximately a diameter of 25 mm and passed through the science cell. Using two 50 mm diameter achromats, of 150 and 200 mm focal lengths, the atomic cloud is imaged onto the CCD camera[4], with a magnification of 1.3. The imaging beam propagates horizontally, which is perpendicular to the quantization axis by direction of the magnetic field. Linearly polarised light is used to irradiate the atom cloud, and the absorption cross section is

$$\sigma_o = \frac{3\lambda^2}{4\pi}, \tag{3.3.3}$$

which is now half of equation 3.3.2. Since there are fewer optical elements for the

[3]Qimaging, model Ret-Exi-F-M-12-IR

[4]Prosilica GE1380 Mono, High Sensitivity 1.4 Mp CCD camera

beam to propagate through the images are much cleaner.

3.4 Optical dipole traps

First realised by S. Chu *et al.* [2], the optical dipole trap is an important tool for controlling ultracold atoms. This section sets out some of the theoretical aspects of dipole traps, leading onto the design of a two-dimensional optical trap that is used in our studies, described in chapter 5. A more detailed review can be found in [121]. Whilst undertaking our studies several different optical dipole trap geometries were tested and a detailed description of these earlier schemes can be found in [81]. Here we only concentrate on the geometry that we currently use.

In contrast to magnetic traps, optical dipole traps can confine atoms and molecules in a wide range of internal states. The method relies on the interaction of the induced atomic dipole moment $\mathbf{p}$ with the electric field of the laser light $\mathbf{E}$. The polarisiability α of the atom determines the strength of the induced dipole moment $\mathbf{p}{=}\alpha\mathbf{E}$, whilst this interaction, known as the AC Stark effect, creates the potential $U_{dip} = -\frac{1}{2}|p|E$. Substituting for α leads to

$$U_{dip} = -\frac{1}{2}\alpha\mathbf{E}^2. \tag{3.4.1}$$

The square of the time averaged electric field amplitude can be written as $\varepsilon^2/2$ and since the intensity I is proportional to ε^2 we have

$$U_{dip} = -\frac{1}{2\epsilon_0 c}\alpha I \tag{3.4.2}$$

where ϵ_0 is the permittivity of free space and c the speed of light. Equation 3.4.2 shows that the sign of α determines whether the potential is attractive or repulsive. By calculating the polarisability, α, as shown in [121] one obtains the optical dipole potential

$$U_{\rm dip}(\mathbf{r}) = -\frac{3\pi c^2}{2\omega_0^3}\Big(\frac{\Gamma}{\omega_0-\omega} + \frac{\Gamma}{\omega_0+\omega}\Big)I(\mathbf{r}), \tag{3.4.3}$$

where ω_0 is the atomic transition frequency, ω the driving laser frequency, Γ the natural line width, and $I(\mathbf{r})$ the position dependent laser field intensity. Heating of atoms in optical dipole traps can occur through the absorption and spontaneous emission of photons. The spontaneous photon scattering rate is given by [121]

$$\Gamma_{\mathrm{dip}}(\mathbf{r}) = -\frac{3\pi c^2}{2\hbar\omega_0^3}\Big(\frac{\omega}{\omega_0}\Big)^3\Big(\frac{\Gamma}{\omega_0-\omega}+\frac{\Gamma}{\omega_0+\omega}\Big)^2 I(\mathbf{r}). \tag{3.4.4}$$

It can be seen from equations 3.4.3 and 3.4.4 that the potential scales inversely with the detuning $\Delta = \omega_0 - \omega$, and the scattering rate inversely with the square of the detuning. Having large detuning reduces the spontaneous scattering rate and, as a result, heating in the potential will be minimised.

3.4.1 Single beam optical dipole trap

Optical dipole traps fall into two categories, red detuned or blue detuned. For blue detuned traps the atoms are confined in the intensity minima surrounded by high intensity. The main advantage is that they have lower scattering rates as the atoms spend most of the in the lowest intensity regions. In general, however, they have more complicated geometries. A red detuned trap confines the atoms in a local intensity maximum. The simplest realisation is a single focussed red-detuned laser beam, which is used in our experiment. A focused Gaussian beam has an intensity distribution with power P given by

$$I(r,z) = \frac{2P}{\pi w^2(z)}\exp\Big(-2\frac{r^2}{w^2(z)}\Big) \tag{3.4.5}$$

where $r^2{=}x^2+y^2$ and

$$w(z) = w_0\sqrt{1+\Big(\frac{z}{z_R}\Big)^2}. \tag{3.4.6}$$

Here w_0 is the beam waist and $z_R = \pi w_0^2/\lambda$ the Rayleigh length. The waist is defined as the radial distance where the intensity drops to $1/e^2$ of its peak intensity. Combining

equations 3.4.2, with 3.4.5 and 3.4.6 the potential has the form

$$U_{\rm dip}(\mathbf{r}) = \frac{U_0}{1+\left(\frac{z}{z_R}\right)^2}\exp\left(-2\frac{r^2}{w_0^2\left(1+\left(\frac{z}{z_R}\right)^2\right)}\right) \tag{3.4.7}$$

where U_0 is the trap depth and can be calculated using equations 3.4.5 and 3.4.3 for $r = z = 0$. When the temperature T of the atomic sample is low such that $T \ll U_0$ the atoms will reside at the centre of the trap. This allows one to use the harmonic approximation of equation 3.4.7. A Taylor expansion out to the second order gives

$$U_{\rm dip}(\mathbf{r}) \simeq -U_0\Big[1-\Big(\frac{z}{z_R}\Big)^2-2\Big(\frac{r}{w_0}\Big)^2\Big]. \tag{3.4.8}$$

The 2nd and 3rd terms are harmonic oscillator potentials. The characteristic oscillation frequencies of these potentials are in the radial and axial trapping directions

$$\omega_z = \sqrt{\frac{2U_0}{mz_R^2}} \qquad \text{and} \qquad \omega_r = \sqrt{\frac{4U_0}{mw_0^2}}, \tag{3.4.9}$$

where m is the mass of the atom.

Dipole trap generation: The laser source for our dipole trap is a CW ytterbium fibre laser (IPG-Photonics, YLR-100) with a peak output power of 100 Watts at a wavelength of 1075 nm. It has a near Gaussian beam profile ($M^2 \leq 1.05$) and linearly polarised output. Lasers required to produce a dipole trap do not generally require high stable frequency control so long as the light is far enough detuned from resonance. However, during the evaporation process we require good intensity stabilisation, and therefore we use an acousto optic modulator[5] (AOM) with a fixed frequency (-120 MHz) and control the first order intensity of the AOM through a Proportional Integral Differential (PID)[6] controller. For optimum AOM efficiency a 1 mm beam diameter is used, and therefore we reduce

[5]Crystal Technology Inc. λ=1047-1060 nm, 120 MHz fixed frequency

[6](Stanford Research Systems: SIM 960)

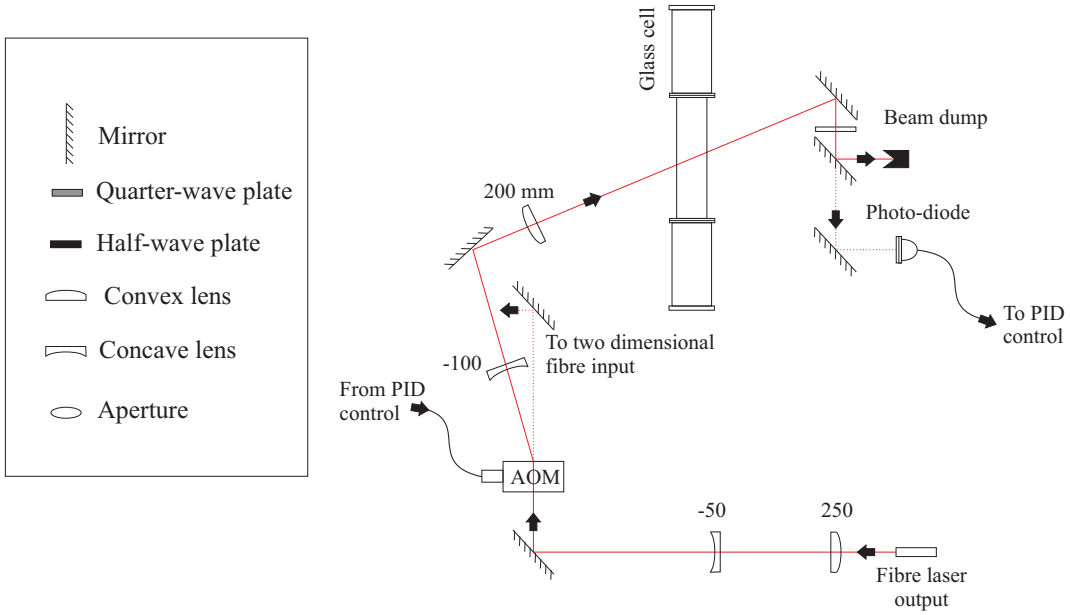

Figure 3.4.1: Schematic of the single optical dipole trap.

the 5 mm beam output of the fibre laser by a telescopic arrangement of 250 mm and -50 mm focal length lenses. Using the first order of the AOM we expand the beam with a -100 mm focal length lens, and use a 200 mm focal length lens to focus to a waist of 38 μm at the centre of the glass cell, as shown in figure 3.4.1. After passing through the cell, a fraction of the dipole trap is split of and directed onto a photodiode. The photodiode signal is compared to a control voltage generated by our LabView control program. The difference of these provides an error signal which is sent to the PID controller to control the Radio Frequency (RF) power sent to the AOM.

3.4.2 2D optical dipole potential

Recently experiments using ultracold bosonic gases have been able to access the Berezinskii-Kosterlitz-Thouless (BKT) regime in a quasi-2D environment using optical lattices [52], laser light sheets [49, 53], a surface wave trap [50, 54], and a combination of optical and magnetic trapping [51]. The work presented here is based on a laser light sheet: an elliptical Gaussian beam produced by tightly focusing a circular Gaussian

beam in one direction with a cylindrical lens. This will enable us to confine atoms in the light sheet such that the transverse harmonic oscillator level spacing discussed in section 2.9.2 in the tight trapping direction is greater than the Fermi energy of the gas. This will allow an investigation of the quasi-2D regime of a strongly interacting ^{6}Li Fermi gas. This section describes the changes to the equations for the single dipole trap potential described in section 3.4.1 in the presence of the elliptical Gaussian beam.

A schematic of the potential can be seen in figure 3.4.2. At this point we will also define the axes that are used throughout the two dimensional discussion and will be repeated where necessary for the reader. From figure 3.4.2 one can see that

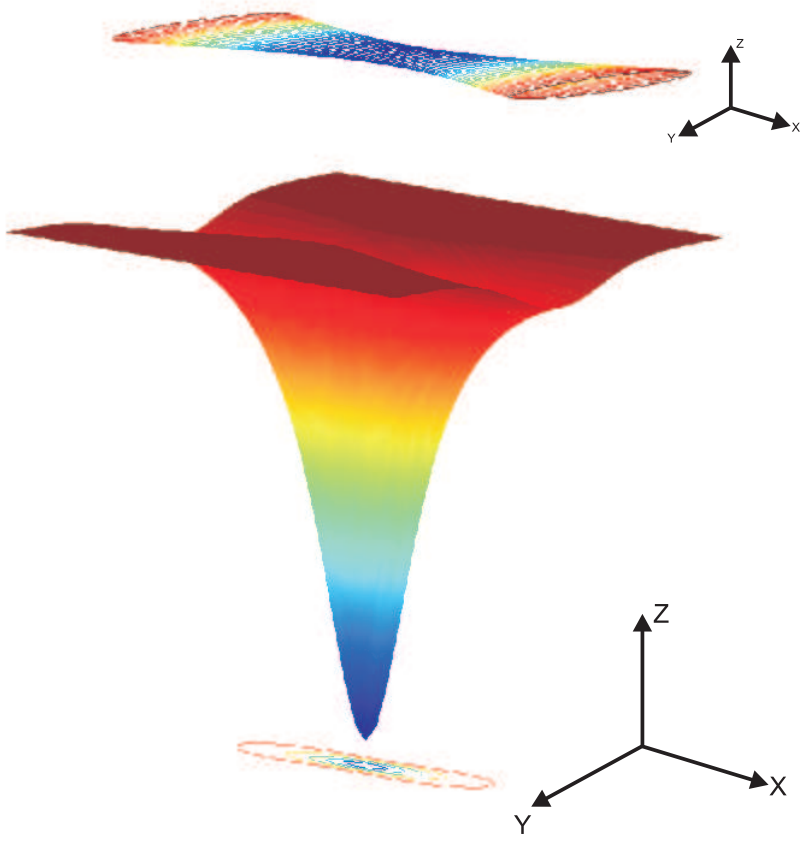

Figure 3.4.2: Schematic of the two dimensional optical potential.

the z-direction is the direction of tight axial confinement and the x, y directions are the directions of weak radial confinement. In section 3.4 equation 3.4.5 gives the intensity distribution for a circular Gaussian beam. Since an elliptical beam has two different waists, we modify equation 3.4.5 such that $w(z)$ is replaced by the geometric mean $\sqrt{w_y(x)w_z(x)}$. Substituting this into the intensity distribution equation 3.4.5, we obtain

$$I(x,y,z) = \frac{2P}{\pi w_y(x) w_z(x)} \exp\Big(-2\frac{y^2}{w_y^2(x)} - 2\frac{z^2}{w_z^2(x)}\Big). \tag{3.4.10}$$

The potential now has the form

$$U_{\text{dip}}(\mathbf{r}) = \frac{U_0}{\sqrt{1+\big(\frac{x}{x_{Ry}}\big)^2}\sqrt{1+\big(\frac{x}{x_{Rz}}\big)^2}} \exp\Big(\frac{-2y^2}{w_{0y}^2\big(1+\big(\frac{x}{x_{Ry}}\big)^2} - \frac{2z^2}{w_{0z}^2\big(1+\big(\frac{x}{x_{Rz}}\big)^2\big)}\Big). \tag{3.4.11}$$

As defined in section 3.4.1 if the temperature T of the atomic sample is lower than the dipole potential $T \ll U_0$ the atoms will reside at the centre of the trap and one can apply a Taylor expansion, to obtain a harmonic approximation of the trapping potential

$$U_{\text{dip}}(\mathbf{r}) \simeq -U_0\Big[1 - \Big[\Big(\frac{x}{2x_{Ry}}\Big)^2 + \Big(\frac{x}{2x_{Rz}}\Big)^2\Big] - 2\Big(\frac{y}{w_{0y}}\Big)^2 - 2\Big(\frac{z}{w_{0z}}\Big)^2\Big]. \tag{3.4.12}$$

The trap frequencies in the tight axial and weak radial directions are

$$\omega_z = \sqrt{\frac{4U_0}{mw_{0z}^2}} \qquad \text{and} \qquad \omega_y = \sqrt{\frac{4U_0}{mw_{0y}^2}}. \tag{3.4.13}$$

One can see from equation (3.4.13) that the z and y directions are unchanged in calculating the frequencies. However, one must take into account both waists to calculate the frequency in the x direction of the potential, giving

$$\omega_x = \sqrt{\frac{U_0}{m}\Big(\frac{1}{x_{Ry}^2} + \frac{1}{x_{Rz}^2}\Big)}. \tag{3.4.14}$$

3.4.3 Two dimensional set-up

Figure 3.4.3 shows a schematic of the two dimensional optical set-up. The laser source is a 1 W pick-off of the main 100 W ytterbium fibre laser. This is coupled into an acousto-optic modulator (AOM) which is connected to a home-made Proportional Integral (PI) controller, since we require precise intensity stabilisation. The light is shifted -120 MHz by a fixed frequency AOM. This eliminates any interferences due to the overlap of the two dimensional trap and the main optical dipole trap. The beam is coupled to a single mode polarisation maintaining fibre. The fibre input has a large mode field diameter giving a small power density and allowing high power (1-2 W) beam input. The fibre is directly coupled to a lens mounting cage giving direct alignment with the axes of the lenses. To calculate the lens requirements we apply the ABCD matrix to a Gaussian beam propagating through a set of lenses. Selecting waists of 5 μm for the tight confinement and 400 μm for the weak confinement we fix the final focal length to 100 mm, since this is as close to the glass cell as we can position the optics. Using a 100 mm focal length lens, a $1/e^2$ beam waist of 5 μm is obtained with a beam of 6.8 mm radius. Since we are coupling directly out of a fibre we do not use a telescope. We set the distance of the collimating achromat to be 100 mm from the fibre exit. To obtain weak confinement we expand the beam in only one dimension; this is achieved

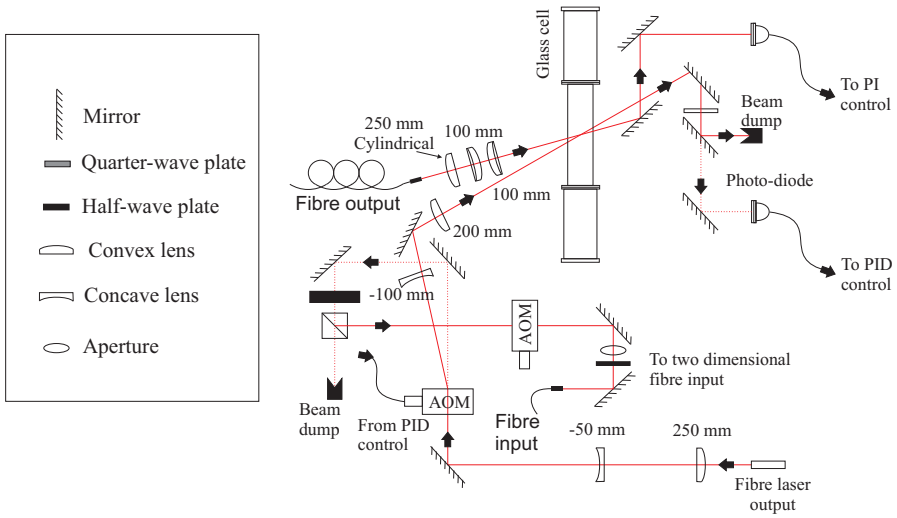

Figure 3.4.3: Schematic of the optics used for the 2D optical trap.

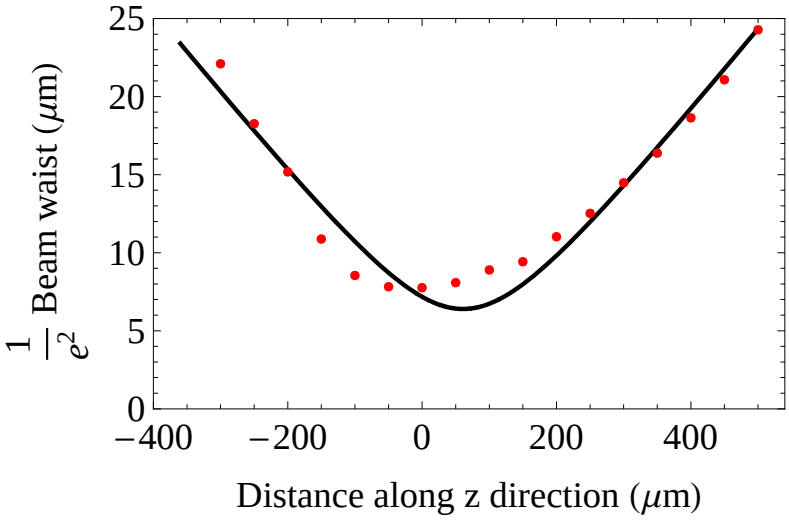

Figure 3.4.4: Beam waist measurement of the tight confinement direction.

with a cylindrical lens of 250 mm focal length. This is situated before the achromats allowing the position to be changed if a smaller or larger weak confinement is required, without disturbing the tight confinement. The beam waist was measured for the tight trapping direction in a test set-up prior to installing the optics onto the experiment. Using a CCD camera on a translation stage images at different distances from the fixed fibre and lenses along the beam were obtained. By fitting each measurement with a Gaussian function we obtain the $1/e^2$ beam radii value and fit these values to the beam waist equation 3.4.6, giving a minimum waist of 6.4(0.3) μm, where the statistical error is produced by a nonlinear regression fit in Mathematica. From figure 3.4.4 one can see that the beam waist measurement becomes flat around the minimum, due to the finite pixel size (6.45 μm) of the camera.

3.5 Experimental control sequence

This chapter has described the construction of the main experimental segments. However, without precise timing and control of the sequence of events, production of a quantum degenerate gas would be impossible. All parameters are controlled by voltages that are varied throughout a sequence. This job is performed by three National

Instruments PCI digital to analog boards, with eight analog outputs and a voltage range of -10 to +10 V housed in a PC. More detail of the computer control program can be found in [81]. With the ability to now control each element a typical experimental sequence is described below.

The first stage is the MOT: production. A vapour of ^{6}Li is produced by the oven and collimated towards the Zeeman slower. Before entering the slower the mean velocity of the atoms is approximately 1500 m/s. The Zeeman slowing coil is held at 2.95 Amps for 30 seconds and produces a spatially varying magnetic field up to 620 G with an approximate parabolic shape. Opposing the atomic beam is the Zeeman slowing laser beam, which is red-detuned from the $|F = 3/2\rangle$ state by 913 MHz. At the end of the Zeeman slower the velocity of the atoms is reduced to a point where the atoms can be captured in the MOT. The Zeeman slowing beam is then shut off via a mechanical shutter and the coil switched off. During this time the MOT is being continuously loaded. Next the MOT is compressed to increase the density by increasing the current through the MOT coils such that the magnetic field gradient changes from 20 G/cm to 50 G/cm. In the same instance the frequency of the trapping light and re-pump light are brought to half a line width from resonance. The intensities in both beams are also reduced to reach the lowest temperature, where the re-pump light is reduced more rapidly than the trapping light. This helps pump the atoms into the $|F = 1/2\rangle$ state for loading into the dipole trap. This phase of the experiment takes 20 ms and at the end an AOM and mechanical shutter switch off the MOT beams. The dipole trap is switched on 100 ms before the MOT compression takes place. A transfer of approximately 10^6 atoms to the $|F = 1/2, m_f = \pm 1/2\rangle$ states into the dipole trap is achieved. At this point the Feshbach coils are switched on ready for evaporation. The coils are mounted in Helmholtz configuration and are wound on hollow core square cross-section wire so that cooling water can be sent through them. Each coil has dimensions of 3.5 (5.5) cm inner(outer) radius and are 3 cm thick and are separated by 3.5 cm. They can produce magnetic fields up to 1.5 kG by passing 200 Amps through them; this provides good coverage of the 834 G Feshbach resonance.

There are three stages to the evaporative cooling process: Initially the IPG laser is turned on at 95 W and held there for plain evaporation to take place, then a linear ramp of the laser intensity is performed reducing the power from 95 W to 12 W in 1800 ms. The first part of the evaporation is performed using an analog control input directly on the IPG fibre laser. Once the power reaches 12 W the photodiode which was previously above saturation takes over and the signal from it is sent to the intensity stabilisation electronics. The laser power is now lowered by a 4 second logarithmic ramp to a final trap power of around 20 mW. This cools the atom cloud down to degeneracy. The optical trap can then be shut off via an AOM and the control unit of the laser.

Upon reaching degeneracy the ramps for different experimental measurements take place. At the end of those sequences information is extracted via absorption imaging. We start by allowing the cloud to expand, opening the imaging shutter in 1.3 ms and pulsing on resonant light for 10 μs where the resulting image is recorded by the CCD camera. This completes one cycle of the experiment which typically takes 40 seconds. The system is then reset to start a new cycle.

3.6 Summary

This chapter describes the experimental set-up and outlines the vacuum system, the laser system for producing a ^{6}Li MOT, absorption imaging procedures and our optical dipole potential used to obtain our quantum degenerate gases. Many of the details are kept brief and a more in depth discussion of the vacuum system, magnetic field coils and absorption spectroscopy are contained in the thesis of Jürgen Fuchs [81]. A brief description of the new additions; offset locking and side imaging, is also given where a more in depth discussion is given in the thesis of Gopisankararao Veeravalli [82]. Along with the introduction of the single beam optical dipole trap we discussed the design and construction of the 2D optical dipole trap to perform the 2D experimental studies described in chapter 5.

Chapter 4

Quantum degenerate gas production

4.1 Introduction

This chapter describes the production of our quantum degenerate gases. Trapping and cooling techniques for neutral atoms have been well documented, both theoretically and experimentally and only a brief description of each topic is given. The reader is referred to articles [2, 3, 4, 5] and references therein for a more detailed discussion on these subjects.

In our laboratory the trapping and cooling procedure is a two stage process involving a magneto optical trap (MOT) and a single beam optical dipole trap where forced evaporation takes place. Depending on the type of experiment being performed we apply an external magnetic field which can control the interparticle interactions via a magnetic Feshbach resonance to produce a molecular Bose-Einstein Condensate (mBEC) or an interacting Degenerate Fermi Gas (DFG).

4.2 Zeeman slower

Unless otherwise stated the description given in this section and section 4.3 follow that of Metcalf and van der Straten [122]. To trap atoms in a magneto optical trap (MOT) the atoms need velocities on the order of a few tens m/s. However, the thermal lithium atomic beam originating from our oven has an average velocity that is much larger than this. We can calculate the average velocity of the atomic beam after exiting the oven using [123]

$$f_{ab}(v) = \frac{v^3}{2}\Big(\frac{m}{k_bT}\Big)^2 \exp\Big(\frac{-mv^2}{2k_bT}\Big). \tag{4.2.1}$$

From this it follows that the lithium atomic beam has an average velocity of

$$\bar{v}_{ab} = \sqrt{\frac{9\pi}{8}\frac{k_bT}{m}} \sim 1840ms^{-1}. \tag{4.2.2}$$

Deceleration of the atomic beam can be achieved with a counter-propagating resonant laser. The velocity of the atom changes since it continuously absorbs and emits a photon with momentum $\hbar\vec{k}$ as described below.

We start by considering a simple two-level atom with a ground state $|g\rangle$ and an excited state $|e\rangle$; the atom has a resonance frequency ω_{atom} in the presence of a field with frequency $\omega_{atom} \approx \omega_{laser}$. By absorbing a photon, momentum is transferred to the atom from the optical field. Due to momentum conservation, the atom's momentum changes. When spontaneous emission occurs the atom relaxes into the ground state and emits a photon in a random direction. Following many cycles of absorption and emission the nett force resulting from absorption point in the direction of the laser beam, while the recoil kicks from spontaneous emission, being in random directions, average to zero. The resulting spontaneous force is

$$\vec{F}_{sp} = \hbar\vec{k}\Gamma_s, \tag{4.2.3}$$

where $\hbar\vec{k}$ is the momentum of the photon and Γ_s is the scattering rate of spontaneous

emission by the atom after absorbing a photon. The scattering rate depends upon the intensity of the laser I, the initial velocity of the atoms $\vec{v}$ and the frequency detuning of the laser from the resonant frequency of the atom, defined as $\delta = \omega_{atom} - \omega_{laser}$. This gives a velocity dependent detuning

$$\delta' = \delta - \vec{k} \cdot \vec{v}. \tag{4.2.4}$$

The scattering rate is given by [122]

$$\Gamma_s = \frac{1}{2}\Gamma \frac{I/I_s}{1 + I/I_s + (2\delta'/\Gamma)^2} \tag{4.2.5}$$

where I_s is the saturation intensity and Γ is the natural line width of the transition. For ^{6}Li these are Γ=2π 5.9 MHz, $I_s = 2.5$ mW/cm^2. The combination of many absorption and emission cycles can lead to a significant velocity change of the atom and slow or cool it down.

Maximum deceleration is limited by the atomic lifetime, $\tau = 1/\Gamma$, and is

$$a_{max} = \frac{\hbar k}{2m\tau} \tag{4.2.6}$$

where m is the mass of the atom. As the atoms slow they move out of resonance with the beam, due to the velocity dependence of equation 4.2.4. To overcome this in our laboratory we employ a spatially varying magnetic field[1] which keeps the atoms in resonance. A Zeeman slower uses a spatially varying magnetic field to tune the energy levels of the atom such that the atom stays resonant with the laser beam. The Zeeman shift is used to compensate the Doppler shift as the atom slows when travelling down the slower. Two types of Zeeman slowing field profiles are generally used; these depend upon the type of circular polarisation used in the Zeeman slowing beam, σ^- or σ^+. If the field of the Zeeman slower is decreasing then one would use σ^+ circularly

[1]The Zeeman slowing coil was first used by Phillips and Metcalf [124]

polarised light and for increasing field as used in our experiment, one would use σ^-. For circularly polarised light in a magnetic field equation 4.2.4 becomes

$$\delta_\pm = \delta \pm \vec{k} \cdot \vec{v} \pm \mu' B/\hbar \tag{4.2.7}$$

where $\mu' = (g_e M_e - g_g M_g)\mu_B$ is the effective magnetic moment with μ_B the Bohr magneton and g_e and g_g are the Landé factors of the ground and excited state. The use of a σ^- Zeeman slower has the distinct advantage that the resonant light used to slow the atoms is far detuned from the MOT where our slowing light has a detuning of 913 MHz with respect to the $|F = 3/2\rangle \longrightarrow |F' = 5/2\rangle$ transition and therefore passes through the MOT without any significant disturbance. The optimal magnetic field profile for such a slower is derived from equations 4.2.5 and 4.2.7 giving

$$B(z) = B_o\Big(1 - \sqrt{1 - \frac{z}{z_o}}\Big), \tag{4.2.8}$$

where $z_o \equiv m v_i^2/\eta\hbar k\Gamma$ and determines the length of the magnet. The magnetic field is

$$B_0 = \frac{\hbar k v_i}{(g_e M_e - g_g M_g)\mu_B}, \tag{4.2.9}$$

where v_i is the initial velocity and the efficiency of the deceleration is $\eta = a/a_{max}$. As stated in section 3.5 the maximum spatially varying magnetic field value is 620 G. This decelerates atoms with velocities of 650 m/s and less to 50 m/s, which is the capture velocity of our MOT, over the length of the Zeeman slower. With the MOT positioned at 18 cm from the end of the Zeeman slowing coil we can determine the radial spread of the atomic beam due to photon scattering and calculate the available percentage of atoms that could be captured by the MOT. The number of photons scattered by the time the atoms reach the end of the Zeeman slower following [125] is

$$v_f(t) = v_i - v_{rec} N(t) \tag{4.2.10}$$

where $v_{i,f}$ are the initial and final velocities $v_{rec} = \hbar k/m$ and N the number of

photons scattered in time t. This gives approximately 6000 photons scattered. The velocity in the transverse direction $v_{x,y}$ will increase due to heating from the number of spontaneous emissions

$$v_{x,y} = \sqrt{\alpha \frac{v_{rec}^2}{3} N(t)} \sim 4.2\ ms^{-1} \tag{4.2.11}$$

where $\alpha = 9/10$ due to the dipole radiation pattern of the spontaneous emission. We now know the transverse velocity component and the MOT capture velocity; this means that once the slowed beam has reached its final velocity it will diverge at an angle of $2v_{x,y}/v_f$ which is approximately 0.17 radians. It is then straight forward to calculate the divergence at the MOT which is 18 cm from the end of the Zeeman slowing coil. The radial spread at the MOT is thus 3 cm. Since the MOT beams are approximately 20 mm in diameter the total number of atoms that reach the MOT is 5%.

4.3 Magneto-optical trap (MOT)

In the previous section we considered the deceleration of an atomic beam such that the atomic beam has been slowed for trapping and cooling in a MOT. Using the scattering rate equation 4.2.5 to describe the rate at which photons are absorbed and spontaneously emitted, a description for cooling of a single atom by a near resonant laser beam can be obtained. The radiative force alone is not enough to trap atoms as there is no spatial confinement. To overcome this a hybrid system is employed using a magnetic field and an optical field [3]. Construction of a magnetic field with two coils in an anti-Helmholtz configuration provides the spherical quadrupole field, which is zero at the centre and increases in all directions as $B(x, y, z) = Ax + Ay - 2Az$, where A is the field gradient.

Consider now an atom with a zero angular momentum ground state $J_g = 0$ and an excited state with $J_e = 1$ angular momentum. In the presence of a magnetic field, the

degeneracy is lifted such that three Zeeman sub-states exist. The resonant frequencies of the magnetic sub-states depend on the atom's position and the polarisation of the laser light. The introduction of the magnetic field modifies equation 4.2.4. The total force acting on the atoms in one dimension is

$$\vec{F}_{\text{total}} = \vec{F}_{+} + \vec{F}_{-} = \pm\frac{\hbar\vec{k}\Gamma}{2}\frac{I/I_{\text{s}}}{1 + I/I_{\text{s}} + [2(\delta_{\pm}/\Gamma)]^2} \tag{4.3.1}$$

where δ now depends on the atom's position as well as its velocity. If the detuning δ is large compared to the Doppler and Zeeman shift we can reduce equation 4.3.1, by expanding the denominator, to

$$\vec{F} = -\beta\vec{v} - \kappa\vec{r}, \tag{4.3.2}$$

where the damping coefficient β and spring constant κ are given by

$$\beta = \frac{8\hbar k^2 \delta I/I_{\text{s}}}{\Gamma(1 + I/I_{\text{s}} + (2\delta/\Gamma)^2)^2}, \tag{4.3.3}$$

$$\kappa = \frac{\mu' A}{\hbar k}\beta. \tag{4.3.4}$$

This treatment can be easily extended to beams propagating along the other axes such that a six beam MOT can be generated. In general MOTs are more complicated than the simple situation defined above. In our experiment the ground state has two angular momentum states $|F = 1/2\rangle$ and $|F = 3/2\rangle$. Light that is resonant with the $|F = 1/2\rangle$ to excited state transition will not be resonant with the $|F = 3/2\rangle$ to excited state transition. This leads to the use of two beams, a trapping beam which pumps from the $|F = 3/2\rangle$ ground state and a re-pump that keeps the atoms from decaying into the dark $|F = 1/2\rangle$ state.

Before loading the atoms into the optical dipole trap we wish to obtain the highest phase space density possible to maximise the number of atoms transferred. This can be achieved by compression of the MOT. Compression is achieved by detuning both

the trapping and re-pump light to half a line width $\Gamma/2$ from resonance and lowering their intensities below the saturation intensity. Simultaneously the gradient of the quadrupole magnetic field is ramped from 20 G/cm to 50 G/cm. We can then determine the temperature of the MOT by turning off the optical and magnetic fields, allowing the cloud to expand, and for various expansion times take an absorption image. Figure 4.3.1 shows the data. The vertical axis is the radial $1/\sqrt{e}$ width squared and the horizontal axis is the square of the expansion time. A Gaussian fit was applied to the profiles of the expanded cloud, and the $1/\sqrt{e}$ width extracted. The width $\sigma(t)$, will increase as

$$\sigma(t) = \sqrt{\sigma_0^2 + \frac{k_B T}{m} t^2}, \tag{4.3.5}$$

where σ_0 is the initial width. From a linear fit we extract a temperature of 280(15) μK. The temperature extracted from the fit is still very high. If we consider equation 4.2.7 it would seem possible to cool the atomic gas to $T = 0K$, but for each recoil kick given to the atom some heating takes place and these random recoil kicks set a lower

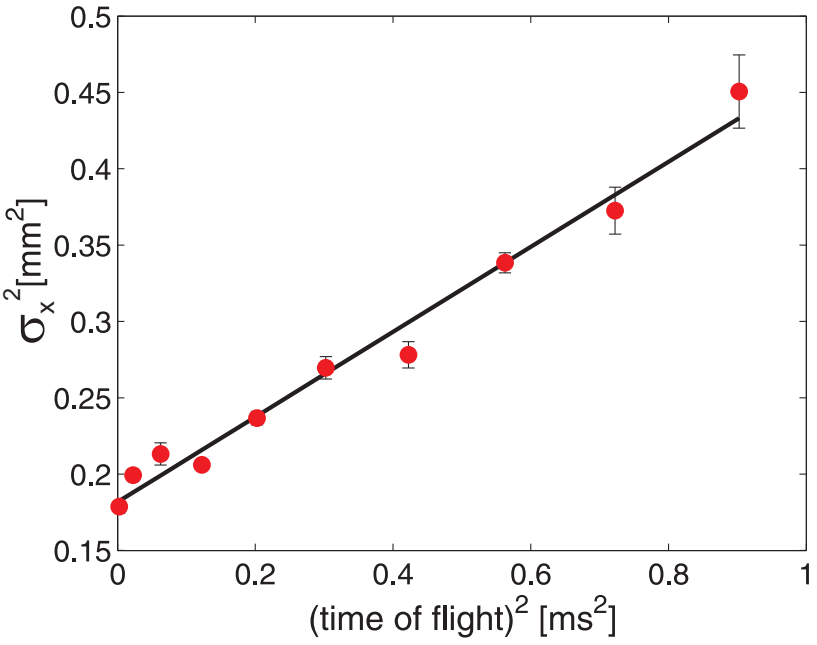

Figure 4.3.1: Temperature measurement of the MOT with 10^8 atoms. The radial width squared is plotted versus the time of flight squared.

limit on the achievable temperature given by the Doppler limit [4, 126]

$$T_D = \frac{\hbar\Gamma^2}{8k_b\delta}[1 + I_t/I_s(2\delta/\gamma)^2]. \tag{4.3.6}$$

In other alkali atom experiments sub-Doppler cooling has been achieved based on the method of polarisation gradient cooling. However, due to the small hyperfine splitting in ^{6}Li we are unable to apply this technique to our MOT, and therefore a lower temperature limit for a ^{6}Li MOT is calculated to be 140 μK.

4.4 Optical dipole trap

The temperature achieved in the MOT is still a long way above the degeneracy temperature. To obtain lower temperatures the atoms must be stored in a different type of trap in which they no longer undergo spontaneous emission. Two types of conservative potentials are possible magnetic and optical potentials. In this work we use an optical trap formed from a single focussed laser beam.

When characterising an experiment using trapped atoms and for any subsequent analysis it is necessary to know the trapping frequencies of the optical dipole trap. Previous theses [81, 82] from our group have reported the trap frequencies. However, since then an additional magnetic gradient field has been added to counteract a stray magnetic field gradient produced by the Feshbach coils. This has changed the effective trap frequencies and allowed us to achieve shallower traps. In section 3.4.1 we presented the single optical dipole potential and derivation of the trap frequencies; here we show the experimentally determined trap frequencies for our experiment.

Measurement of both axial and radial trap frequencies are achieved by shifting the cloud from its equilibrium position and measuring the ensuing oscillation. This process starts by evaporative cooling of the atomic cloud at 810 G, where the scattering length is $\sim$16000 a_0, to a trap depth of 530 nK. Depending on whether a measurement of the

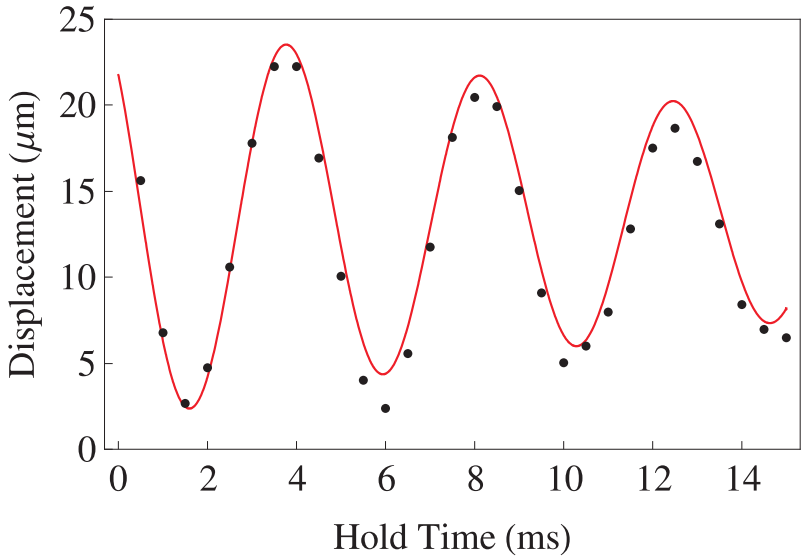

Figure 4.4.1: Single dipole trap frequency in the radial direction given as 230(2) Hz

axial or radial trap frequency, the following process takes place. In the radial case the dipole potential is abruptly switched off and on in the presence of a weak magnetic field gradient. This causes the centre of mass to shift and the cloud oscillates in the trap. The oscillations are observed by measuring the centre of mass displacements of the atomic sample after various hold times through absorption imaging as seen in figure 4.4.1. Fitting the data with a decaying sinusoidal function, due to a slightly anharmonic trapping potential that causes damping, and a straight line to account for a slight drift in the trap position we obtain a radial frequency of 230(2) Hz. In the axial direction, the confinement from the single dipole trap is very weak and the axial confinement is dominated by the residual magnetic field curvature of the Feshbach coils. This is measured to be $0.024(3)\times B$ cm^{-2} in the horizontal plane, and results in an effective trap frequency written as [81]

$$\omega_z = \sqrt{814(180)\, B/\mathrm{kG} + 13.6(4)\, P/\mathrm{mW}}\ \mathrm{Hz}. \tag{4.4.1}$$

The procedure to measure the axial trap frequency is similar to the radial direction except that the initial displacement of the atomic sample is driven by switching on and off of an auxiliary magnetic field gradient. Through the sinusoidal fitting of the

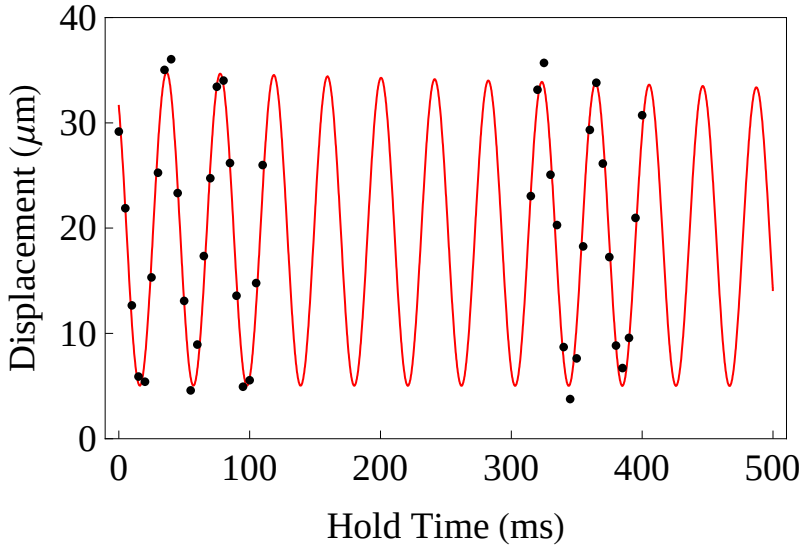

Figure 4.4.2: Trapping frequency due to Feshbach field curvature in the axial direction determined as 24.4(2) Hz

data shown in figure 4.4.2 a frequency of 24.4(2) Hz is obtained, which compares well with the calculated value. Measurements taken in [81, 82] for the radial trap frequencies were observed via top imaging allowing the calculation of the residual magnetic field curvature to be acquired in the horizontal plane. Due to the single dipole trap being cylindrically symmetric one can infer then the frequencies in the vertical plane. However, we now have side imaging and the radial trapping frequencies can be measured with this system allowing us to check for anisotropy and effects of anti-trapping caused by the field curvature of the Feshbach fields in the vertical direction. The radial optical trap frequency will dominate the magnetic frequency as it is much larger, but we can determine the effect of the magnetic field curvature by measuring the trapping frequencies for different trap depths and determining where a power law fit intersects the y-axis as seen in figure 4.4.3. This gives a value of $\omega_{mag} = i35(5)$ Hz compared with the theoretical value $\sqrt{-24.8^2 - 24.8^2} = i34.5$ Hz. The imaginary value informs us that the atoms are anti-trapped as one would expect. Following from this we can calculate the curvature of the magnetic field in the vertical direction

$$\frac{d^2B}{dz^2} = \sqrt{\frac{\omega_{mag}^2 m_{atom}}{\mu_b}} \equiv 0.036(2)B \cdot cm^{-2}. \tag{4.4.2}$$

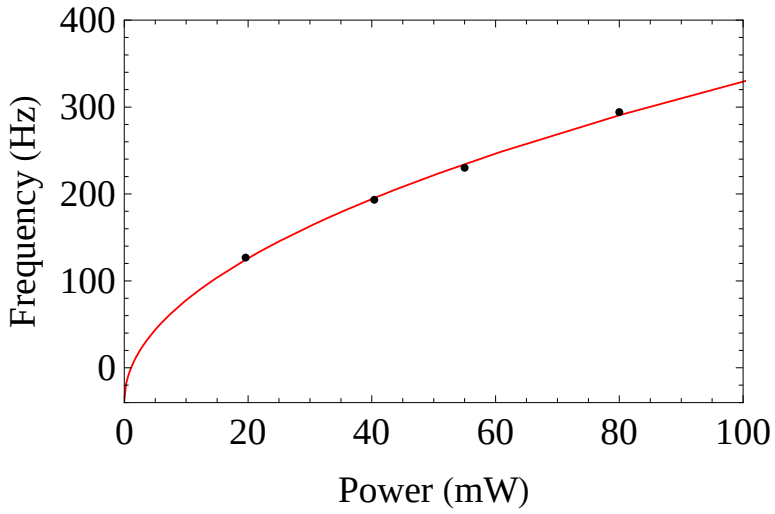

Figure 4.4.3: Radial trap frequencies for four different powers showing an anti-trapping due to the Feshbach magnetic field curvature determined to be $i35(5)$ Hz.

4.4.1 Two dimensional trapping frequencies

In this section measurements of the trapping frequencies for the 2D optical trap in all three dimensions are presented. We first load atoms from the regular 3D optical trap into the 2D optical trap as described later in section 5.2. From the knowledge of the measured trapping frequencies we can calculate the width of the $1/e^2$ Gaussian beam waist of the dipole potential and compare it to the calculated values in section 3.4.2. We apply the same procedure for acquiring the trapping frequencies in the two dimensional gas as we applied to the three dimensional gas described in section 4.4. In the weakly confining directions we displace the centre of mass position of the atomic sample from equilibrium by switching on and off an auxiliary magnetic field gradient, we then observe the ensuing oscillations in the centre of mass by taking absorption images at various hold times. Fitting the observed oscillations with a combined linear and sinusoidal function we extract the frequencies of $\omega_x/2\pi = 57(1)$ Hz and $\omega_y/2\pi = 45(1)$ Hz at a laser power of 504 mW as shown in figures 4.4.4c and 4.4.4b.

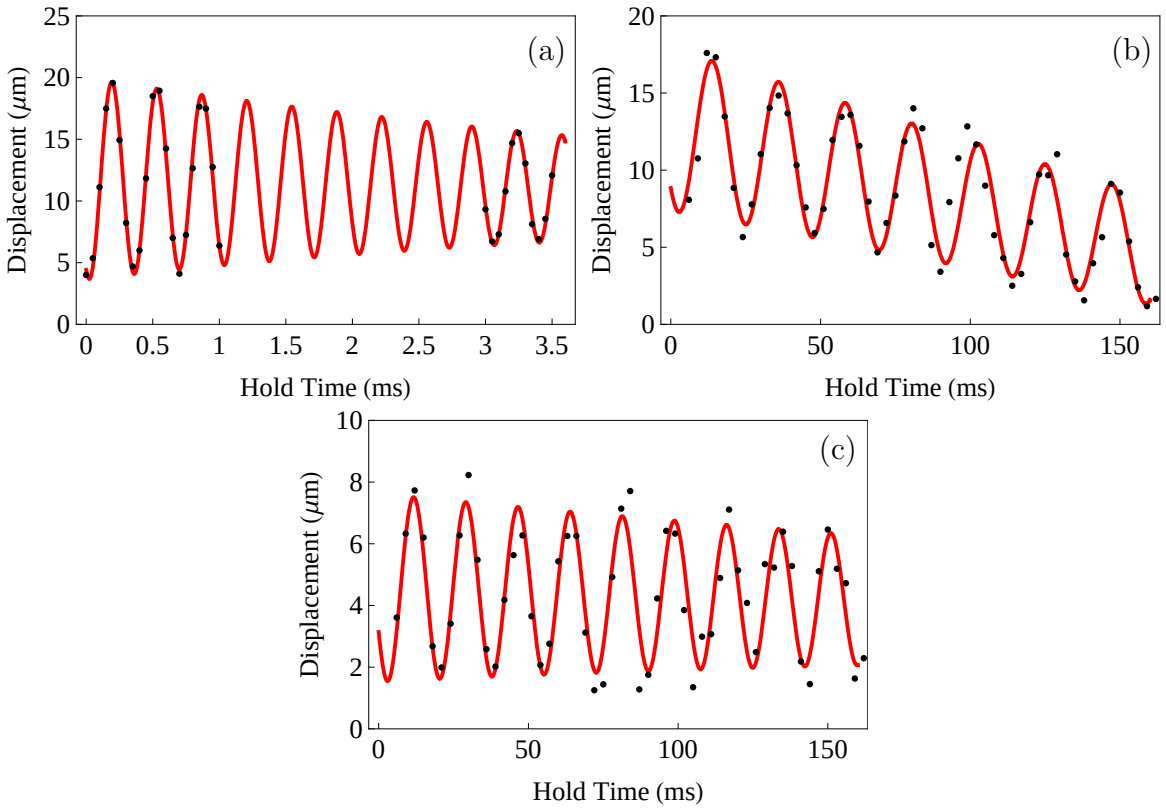

Figure 4.4.4: Trap frequencies in the 2D optical potential (a) $\omega_z/2\pi$=2951(1)Hz, (b) $\omega_y/2\pi$=57(1) Hz, and (c)$\omega_x/2\pi$=45(1)Hz.

Measurements of the tight confinement frequency are achieved by abruptly switching off and on the two dimensional optical potential in the presence of a weak magnetic field gradient and measuring the oscillations as before. Fitting the data gives a trapping frequency of $\omega_z/2\pi$ = 2951(5) Hz as shown in figure 4.4.4a. We can determine the beam waist from measured trapping frequencies which arise from the combination of the residual magnetic field curvature of the Feshbach coils and the optical trap. Our measurements for the trapping frequencies were taken at a magnetic field of 834 G where the magnetic trapping frequency is known to be $\omega_{mag}/2\pi$ = 24.8 Hz. Using $\omega_{meas} = \sqrt{\omega_{mag}^2 + \omega_{opt}^2}$ we calculate the weak confinement trap frequencies to be $\omega_x/2\pi$ = 51(1) Hz and $\omega_y/2\pi$ = 37.5(1) Hz. In the tight confinement direction we have an anti-trapping frequency of $\omega_z/2\pi = i35$ Hz which has essentially no effect on the measured trap frequency being so much smaller than the optical frequency, especially considering

the frequencies add in quadrature. Using equations 3.4.13 and 3.4.14 we can calculate the $1/e^2$ Gaussian beam waist to be in the weak confinement direction 621(5) μm and 7.9(1) μm in the tight confinement direction. We note that the weak direction is larger than described in section 3.4.3. This is due to modifications of the optical trap. Using $\lambda = (\omega_z/\omega_r)^2$ gives an aspect ratio of 58 which is where the majority of our experiments are performed unless stated otherwise. Comparing the tight axial trap frequency to the requirement for two dimensionality $E_f << \hbar\omega_z$ we find that we approach the 2D limit when we have 1700 atoms confined in the trap.

4.5 Evaporative cooling

The technique of evaporative cooling in an optical dipole trap was first demonstrated by Adams *et al.* [127]. The idea behind this technique is for the most energetic atoms to leave the trap whilst allowing the remaining atoms to re-thermalise and lower the average kinetic energy of the atomic sample. The phase space density defined as

$$D = N\left(\frac{\hbar\bar{\omega}}{k_{\mathrm{B}}T}\right)^3, \tag{4.5.1}$$

where $\bar{\omega} = (\omega_x\omega_y\omega_z)^{1/3}$ is the mean trapping frequency, T is the temperature of the atomic sample and N the total number of atoms (section 2.4). The MOTs initial temperature is $\sim 280\mu$K and the phase space density $D \sim 0.006$. The procedure to increase the phase space density in our system starts with a plain evaporation, where we hold the trap at a constant potential depth for 300 ms, and after this time the atomic sample is colder and the evaporation process starts to slow since the collisions that take place do not have enough energy to remove atoms from the tail of the Boltzmann distribution [128]. To overcome this we can employ a forced evaporation technique that continuously removes the most energetic particles by lowering the trap potential. In the dipole trap we have a 50:50 spin mixture of the lowest two hyperfine ground states $|1\rangle$ and $|2\rangle$, Pauli blocking of identical spins suppresses the elastic scattering process

between the atoms; however the presence of the second state allows collisions to take place. The re-thermalisation process needs to be swift for evaporation to be efficient, and depends on the number of elastic scattering events per second

$$\gamma = n\sigma\overline{v} = \frac{4\pi N m \sigma \nu^3}{k_{\mathrm{B}} T}, \tag{4.5.2}$$

where n is the atomic density of each state, $\overline{v}$ is the mean velocity of the atoms, N is the number of atoms in each state, $\nu = \overline{\omega}/2\pi$ is the mean trapping frequency and σ is the elastic s-wave scattering cross section of the colliding atoms in the two lowest hyperfine ground states. In section 2.2 we saw that the scattering cross section depends on the scattering length a through the relationship $\sigma = 4\pi a^2$ if $k^2 a^2 \ll 1$. At unitary ($\sim$ 834 G) this condition is changed since the scattering becomes energy dependent and can now be described by

$$\sigma = \frac{4\pi a^2}{1 + k^2 a^2}. \tag{4.5.3}$$

If $k^2 a^2 \gg 1$ the scattering cross section becomes $\sigma \simeq 4\pi/k^2$ which is the unitary scattering limit of the cross section. This cross section applies at low D but will decrease as $D \to 1$ due to Pauli blocking [129].

O'Hara *et al.* [130] derived a set of scaling laws, shown below, for the number of atoms, elastic collision rate and the phase space density, as the potential depth is lowered as a function of time. They are based on the evaporation parameter $\eta = U/k_B T$, given by the ratio of the potential depth to the temperature which is assumed to remain constant as the trap depth is lowered. For η=10, which is approximately what we observe in our experiments, one can calculate the reduction in trap depth required to increase the phase space density from 0.006 to 1 at which point the scalings no longer hold.

$$\frac{N}{N_{\mathrm{i}}} = \left(\frac{U}{U_{\mathrm{i}}}\right)^{0.19}. \tag{4.5.4}$$

$$\frac{D}{D_{\mathrm{i}}} = \left(\frac{U}{U_{\mathrm{i}}}\right)^{-1.3}. \tag{4.5.5}$$

$$\frac{\gamma}{\gamma_{\mathrm{i}}} = \left(\frac{U}{U_{\mathrm{i}}}\right)^{0.69} . \tag{4.5.6}$$

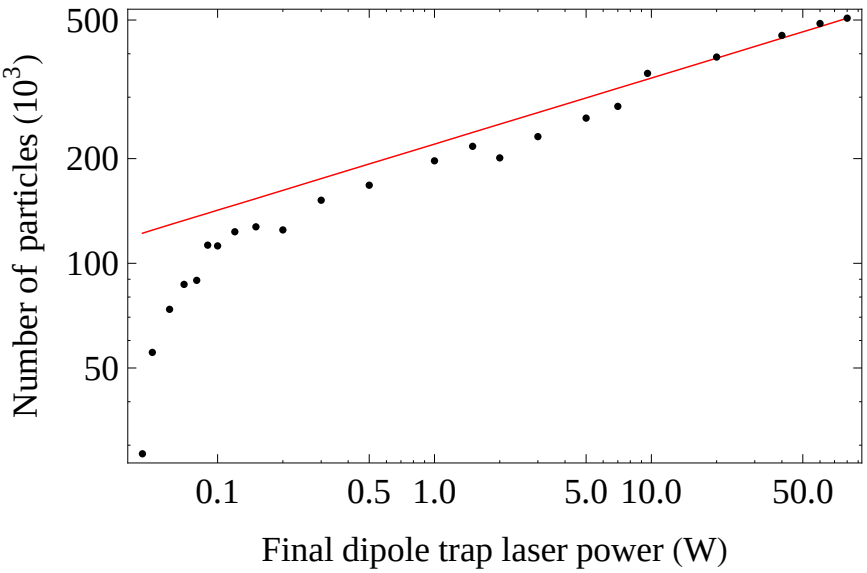

Figure 4.5.1: The scaling law as applied to the evaporation from a single optical dipole trap. Above ∼100 mW the data follows the scaling law predictions.

In figure 4.5.1 we can see data during evaporation in our single beam dipole trap. Evaporative cooling takes place near the Feshbach resonance at 810 G and then the magnetic field is ramped to 750 G in 70 ms where an absorption image is taken. We can see that down to a power of 100 mW ($U_{mol}/k_B = 1\mu K$) the data follows the scaling laws well and that the evaporation is efficient after reducing the trap depth by a factor of 800. Below 100 mW the phase space density approaches unity and the quantum statistics of the gas shift the data below the classical predictions.

4.6 mBEC production

Formation of our mBEC starts by evaporating at 810 G where the scattering length is approximately $16000a_0$. Through three-body recombination stable molecules are

formed when the temperature of the atoms becomes lower than the binding energy of the molecules $E_b \ll k_B T$ as discussed in section 2.7. At this stage, both atoms and molecules can exist in thermodynamic equilibrium. As we evaporate further to lower temperatures the production of molecules is thermodynamically favoured. At a sufficiently high phase-space density Bose-Einstein condensation of the molecules can occur as shown in figure 4.6.1. Here we see the formation of a molecular BEC detected by absorption imaging. Evaporation takes place at 810 G to a final trap power of (a) 16 mW, (b) 60 mW and (c) 200 mW. Then the magnetic field is ramped

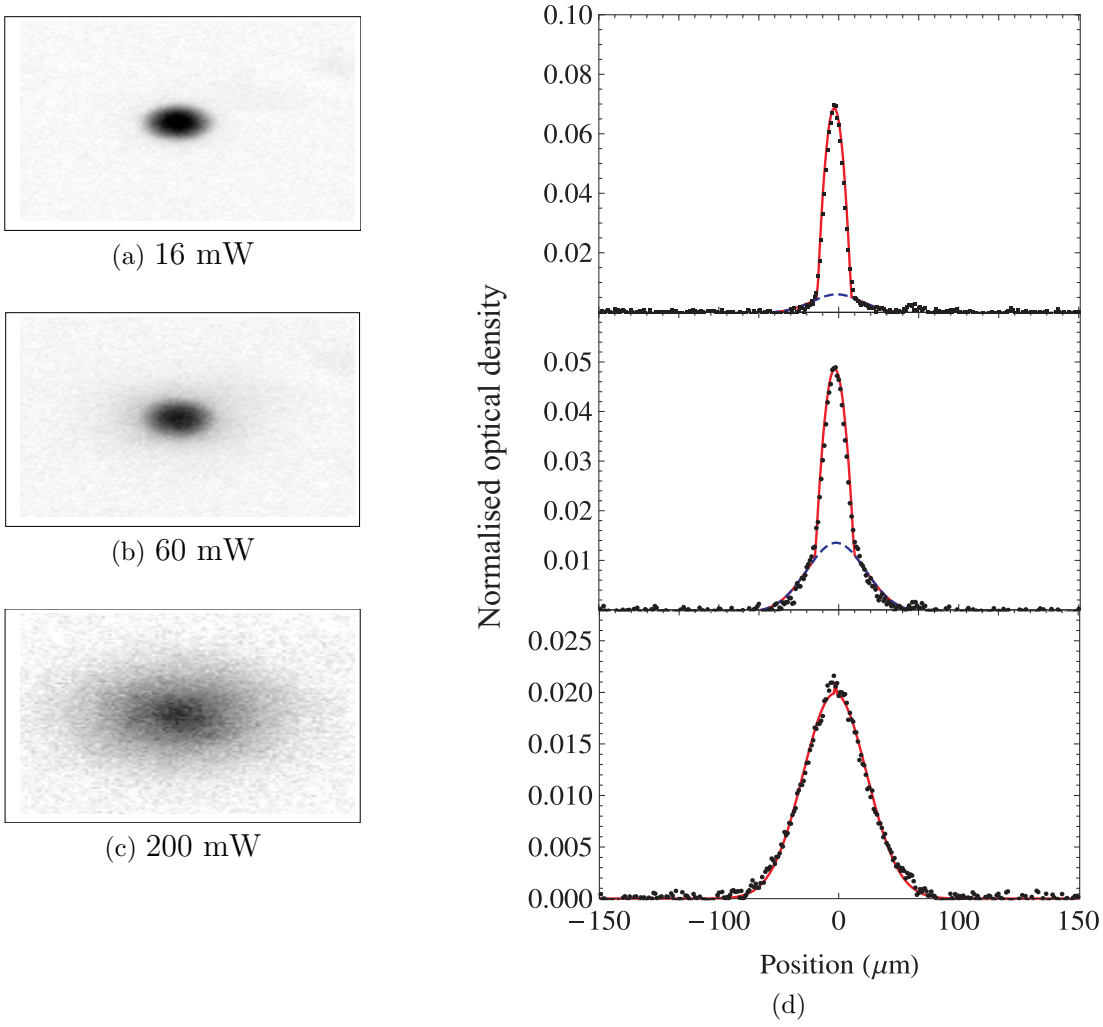

Figure 4.6.1: Formation of a molecular BEC: Absorption images taken at various trap depths are shown in (a)-(c), bimodal distributions of the images a, b and c. The dashed (blue), and solid (red) lines in (d) are fits to a Gaussian, and a combination of the Thomas-Fermi and Gaussian profiles, respectively.

to 650 G in 50 ms and held there for 20 ms to minimise heating due to vibrational quenching collisions. An absorption image is then taken after 3 ms expansion time. Integrated cross sections of these images along the radial trapping direction are shown in figure 4.6.1d. Two different curves fitted to the raw data: a dashed (blue) and solid (red) lines, which are fits to a Gaussian and a combined Thomas-Fermi and Gaussian profile, respectively. The images show a purely thermal cloud increasing to a condensate fraction of $> 85\%$.

4.7 Degenerate Fermi gas production

Production of a strongly interacting degenerate Fermi gas in our system takes place by evaporative cooling the atomic sample at 810 G, then the magnetic field is adiabatically ramped to the desired value on the BCS side of the Feshbach resonance. This takes advantage of the fact that the crossover from the BEC to BCS side can be performed isentropically [16]. Figure 4.7.1 shows a one-dimensional profile of the various degenerate gases taken by absorption imaging and produced in this manner. We see that at 991 G and 834 G fermions follow a Fermi-Dirac distribution. We also show the integrated cross section of a mBEC image at 650 G with a fitted Thomas-Fermi (bosons) distribution. These three plots show the growth of a condensation of fermionic atom pairs as we change from a positive (650 G) to a negative scattering (991 G) length. Figure 4.7.2 shows the 834 G data with both a Fermi-Dirac distribution and a Gaussian distribution fitted to the data. We can see that the peak of the degenerate Fermi gas has a flatter top than that of a Gaussian distribution. This is due to atoms following Fermi-Dirac statistics. The momentum distribution then starts to broaden and has a lower peak.

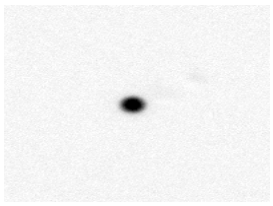

(a) Thomas-Fermi 650 G

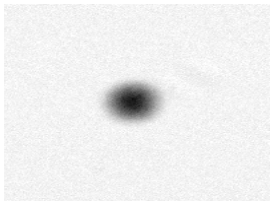

(b) Unitarity 834 G

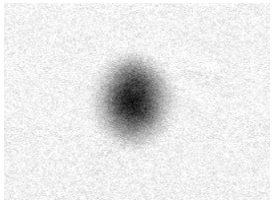

(c) Fermi-Dirac 991 G

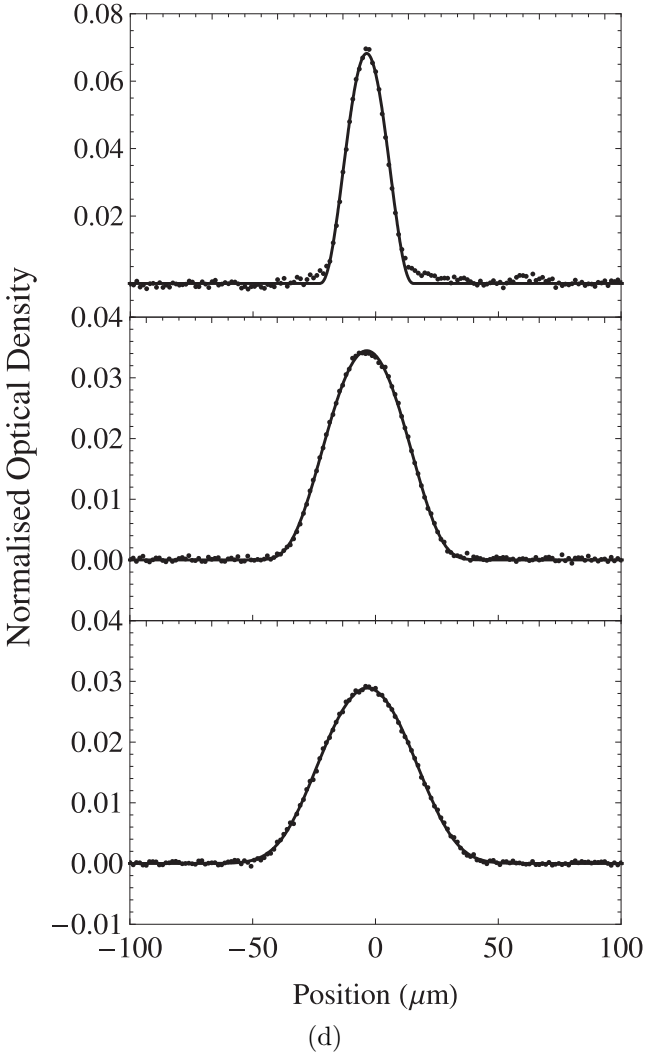

(d)

Figure 4.7.1: Absorption images taken at three different magnetic fields for the same expansion time (a)-(c), one dimensional profiles (d) of images a, b and c. At 650 G a Thomas-Fermi distribution is fit and at 834 G and 991 G a 1D poly-logarithm fit is applied.

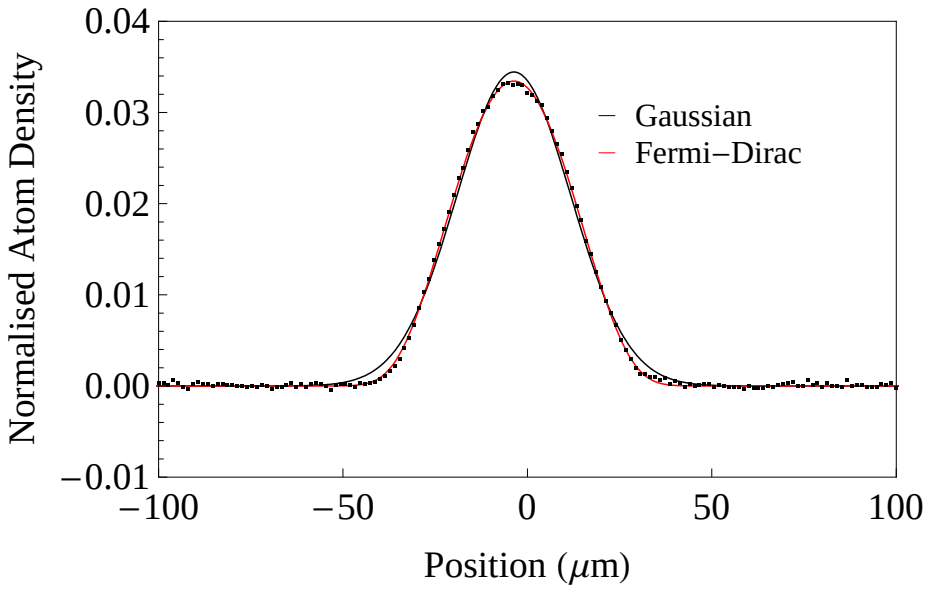

Figure 4.7.2: Gaussian distribution fitted to the image taken at 834 G showing the peak of the Fermi gas has a flatter distribution.

4.8 Summary

This chapter described our procedure for cooling and trapping the ^{6}Li atoms from the Zeeman slowing and MOT stages through to evaporation to degeneracy. We fully characterised both our 3D and 2D optical traps through measurements of the trapping frequencies and comparisons with theoretical expectations. Our ability to prepare ultracold Fermi gases anywhere on the BEC-BCS crossover and to load these into our quasi-2D optical trap set the scene for our experiments on the 2D BEC-BCS crossover described in the following chapter.

Chapter 5

Experiments on a quasi-2D degenerate Fermi gas

5.1 Introduction

During recent years low dimensional quantum gases have generated much interest since they display properties and dynamics vastly different to a their three dimensional counter parts. The first low dimensional condensate was reported by Görlitz *et al.* [49]. Who observed the crossover from 3D to a 2D and 1D condensate in an attractive dipole potential with an aspect ratio of $\lambda \approx 80$. To achieve lower dimensions they lowered the number of trapped atoms below a critical value. Since then a number of groups have studied the quasi-2D regime [50, 51, 52, 53, 54] using various trapping configurations. One of the long standing goals in 2D systems is to observe the Berezinski-Kosterlitz-Thouless (BKT) superfluid transition and the associated formation of vortex-antivortex pairs as described in section 2.11. In 2006 Hadzibabic *et al.* [55] reported evidence for the BKT transition in a trapped Bose gas. Through the study of defects in the matter-wave interference patterns of overlapping 2D Bose-Einstein condensates released from a blue detuned optical lattice they were able to observe phase dislocation associated

with vortices. By examining the coherence length in these interference patterns, they identified the BKT phase transition. More recently Cladé *et al.* [53] have observed the transition from a thermal Bose gas to a 2D quasi-condensate and perhaps the superfluid regime below the BKT transition. A few experimental studies have also been reported for low dimensional Fermi gases. Measurements of p-wave [59] Feshbach resonances in 1D and 2D lattices have been performed in ^{40}K, where there is a shift in the resonance position caused by the confining optical potential. In the same system 1D confinement induced molecules [58] were also observed, where measurements of the binding energy showed the existence of weakly bound molecules at scattering lengths $a < 0$. More recently measurements in a 1D Bose gas of ^{133}Cs [60] have revealed a confinement induced resonance and a transition to a Super Tonks-Girardeau gas. Quasi-2D Fermi systems have not received much attention as they are notoriously difficult to deal with both experimentally and theoretically. One recent publication [61] discusses the inelastic decay rate in a quasi-2D Fermi gas formed in an optical lattice and Ferlaino *et al.* [62] produced a quasi-2D Bose-Fermi mixture in a 1D optical lattice.

This chapter describes experiments on a quasi-2D Fermi gas that have taken place in our laboratory. We start by describing the experimental prescription for crossing into a quasi-2D regime. In section 4.4 we have already reported the trapping frequencies associated with a 2D optical potential; so here we move directly to describing the observations of the cloud widths that demonstrate the two dimensionality of the gas. The second part of this chapter describes the main results of the thesis and the indication of a confinement induced resonance in a quasi-2D Fermi gas.

5.2 Forming a quasi-2D Fermi gas

In section 2.9.2 we saw that for an ideal Fermi gas to be two dimensional, it must have fewer atoms than the critical number of atoms. This depends upon the aspect ratio of the tight confinement direction ω_z and the geometric mean of the weakly confining

directions $\omega_r = \sqrt{\omega_x \omega_y}$.

To access the quasi-2D regime we prepare a mBEC with approximately 10^5 atoms in a single beam optical dipole trap as described in section 3.5. We then continue lowering the dipole potential such that atoms continue to be evaporated. Eventually the depth becomes so low that we begin to lose a significant fraction of the trapped atoms. In this way we can control the final atom number in the 3D trap whilst maintaining the lowest possible temperature and the highest phase space density. Once we have reached the appropriate trap depth for the lowest atom number we adiabatically increase the 3D optical potential to a set depth and ramp the Feshbach magnetic field to 834 G. This procedure is followed in order to avoid three body inelastic collisions that may lead to rapid heating when we apply the tighter confinement of the 2D trap on the BEC side of the Feshbach resonance. The next stage is to linearly ramp up the 2D optical potential in 200 ms to a trap power of 500 mW. After allowing the atoms to thermalise for 200 ms we linearly reduce the 3D trap to zero in 200 ms. The final stage is to ramp the Feshbach magnetic field to the magnetic field values we wish to use. Since measurements taken on the BEC side of the resonance can be prone to inelastic losses we apply a short 50 ms magnetic field sweep. Since the mean trapping frequencies are high this is slow enough for the cloud to follow adiabatically. We then allow the atoms to equilibrate for 20 ms. This equilibration time has been experimentally tested and we clearly observe mBECs with very small thermal fraction at a magnetic field of 650 G (section 4.6). This procedure is then followed for all magnetic fields that are used, and an absorption image is taken. This allows us to lower or increase the atom number simply by changing the depth to which we evaporate in the 3D trap while keeping all other parameters the same. Where all 2D traps are much deeper than the final 3D trap.

Measurements of the size of the trapped cloud would be well below the resolution of our imaging system; so time of flight images are needed. Since the trap frequency in the tight direction is now much higher than the 3D case, the gas will expand very quickly in this direction; so only a 500 μs expansion time was used for experiments

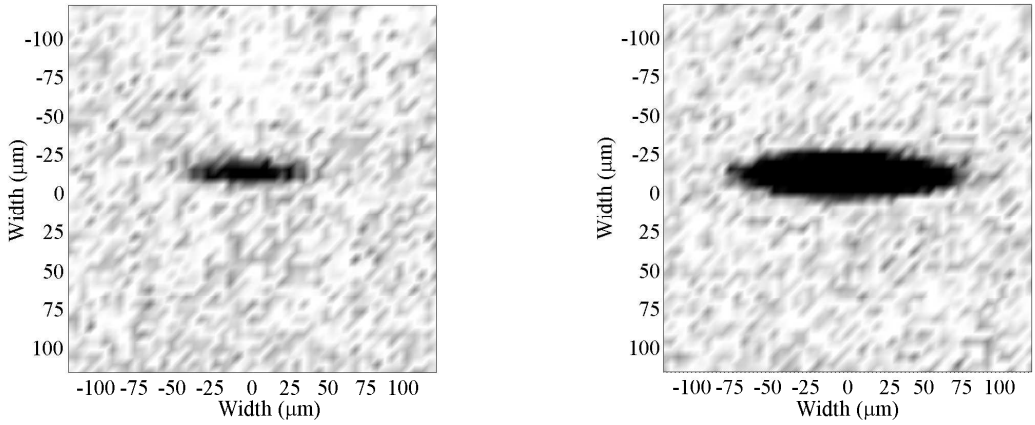

(a) (b)

Figure 5.2.1: Lowering the atom number to reach the quasi-2D regime of a strongly interacting Fermi gas (a) ∼4000 atoms and (b) ∼20000 atoms. Both absorption images are taken at a magnetic field of 834 G and an expansion time of 500 μs.

described in the next section. Figure 5.2.1 shows typical absorption images for a gas approaching the quasi-2D region (a) and a 3D gas (b).

5.3 Two dimensional crossover: Radial cloud size

In section 2.9.2 we saw that reduced dimensionality modifies the density of states such that the 2D radius of a Fermi gas and a BEC grow in the weak confinement direction as

$$R_{F2D} = (8N)^{1/4}\sqrt{\frac{\hbar}{m\omega_r}}\frac{\omega_r}{\omega_i} \tag{5.3.1}$$

$$R_{TF} = \Big(\frac{128}{\pi}\Big)^{1/8}(\frac{Naa_r^4}{a_z})^{1/4}, \tag{5.3.2}$$

respectively. The three dimensional radii of a Fermi gas and BEC grow, respectively as

$$R_{\mathrm{F}}^{i} = \sqrt{\frac{\hbar}{m\overline{\omega}}}(48N)^{1/6}\frac{\overline{\omega}}{\omega_i} \tag{5.3.3}$$

$$R_i = a_{ho}\frac{\bar{\omega}}{\omega_i}\left(\frac{15Na}{a_{ho}}\right)^{1/5}. \tag{5.3.4}$$

As a result, by measuring the radial width of the gas as we reduce the atom number we expect a change in the slopes when we enter the quasi-2D regime. Measurements are shown in figure 5.3.1, where the black (squares), red (triangles), and blue (circles) are the data points for magnetic fields of 810 G, 834 G and 991 G, respectively. The

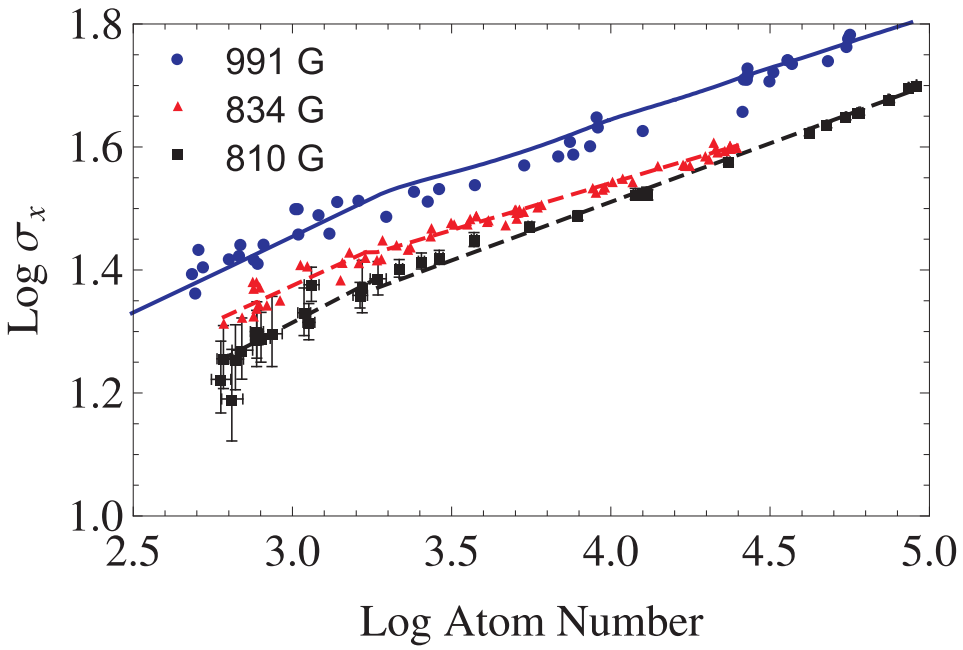

Figure 5.3.1: Observation of the crossover from 3D to 2D in the weak radial direction after 500 μs expansion time. The data points are black (squares), red (triangles), and blue (circles) for magnetic fields of 810 G, 834 G and 991 G, respectively. The dashed lines are $\log\sigma(N) = \log nN + a$ curves fitted to the data points of 991 G, 834 G and 810 G, where the dashed black line for 810 G gives n=0.20(0.01)in the 3D regime and n=0.27(0.04) in the 2D regime. At 834 G the dashed red line gives n=0.15(0.01)in the 3D regime and n=0.23(0.02) in the 2D regime. At 991 G the dashed blue line gives n=0.175(0.010)in the 3D regime and n=0.26(0.03) in the 2D regime. Also shown is the theoretical curve calculated in section 2.9.2 as the solid blue line. We also show typical error bars on the 810 G data points in both width (vertical error bar) and atom number (horizontal error bar).

dashed lines are fits of a straight line function $\log \sigma(N) = n \log N + a$ except for the upper solid blue line which is the theoretical curve shown in figure 2.9.4. The expansion time for the atomic cloud is 500 μs and the trap frequencies are $\omega_z/2\pi$=2820(50) Hz in the axial direction and $\omega_x/2\pi$=55(1) Hz and $\omega_y/2\pi$=41(1) Hz in the radial directions. The frequencies here differ from those given in section 4.4.1 as the data was taken with a slightly different optical configuration. To find the cloud width a Gaussian function was fit to an averaged image, where for the lower atom numbers ($N < 10^4$) the average consisted of 30 individual images, and for the larger atom numbers the average consisted only of 3 images as the signal to noise was far better. At 834 G we apply linear fits to the 3D and 2D regimes. We make the assumption that the 3D regime starts at the critical atom number given as N_{crit}=1700. This is also justified by the data obtained for the transverse width shown in figure 5.4.2. Since the error bars are quite large in the low atom number region each fit is weighted appropriately. By doing this we obtain values of $n = 0.15(0.01)$ in the 3D regime and n=0.23(0.02) in the 2D regime, which indicates that we crossover from a 3D to a 2D regime. We apply the same procedure to the 810 G data and obtain the value $n = 0.20(0.01)$ in the 3D regime and $n = 0.27(0.04)$ in the 2D regime, again indicating a dimensional crossover. For 991 G we can plot the theoretical curve shown in figure 2.9.4 for a non-interacting Fermi gas. This is shown as the solid blue line in figure 5.3.1. We apply an arbitrary scaling to the width since the theoretical calculation is for an in-trap non-interacting Fermi gas. A straight line fit to the 991 G data is also applied in the 2D and 3D sections giving slopes of $n = 0.26(0.01)$ and $n = 0.175(0.010)$, respectively. This is where we expect the cloud to closely match the ideal Fermi gas and the fitted slopes demonstrate this. However, the shell structure that is described in section 2.9.2 is difficult to discern from the experimental data points. Due to difficulty in measuring small atom numbers we are not able to conclude that we are in the 2D regime. More conclusive evidence is shown in sections 5.4 and 5.5. To compare these results to a true 3D system we perform the same experiment in the main single beam optical dipole trap at 834 G where the measurements can be seen in figure 5.3.2. The trapping frequencies are

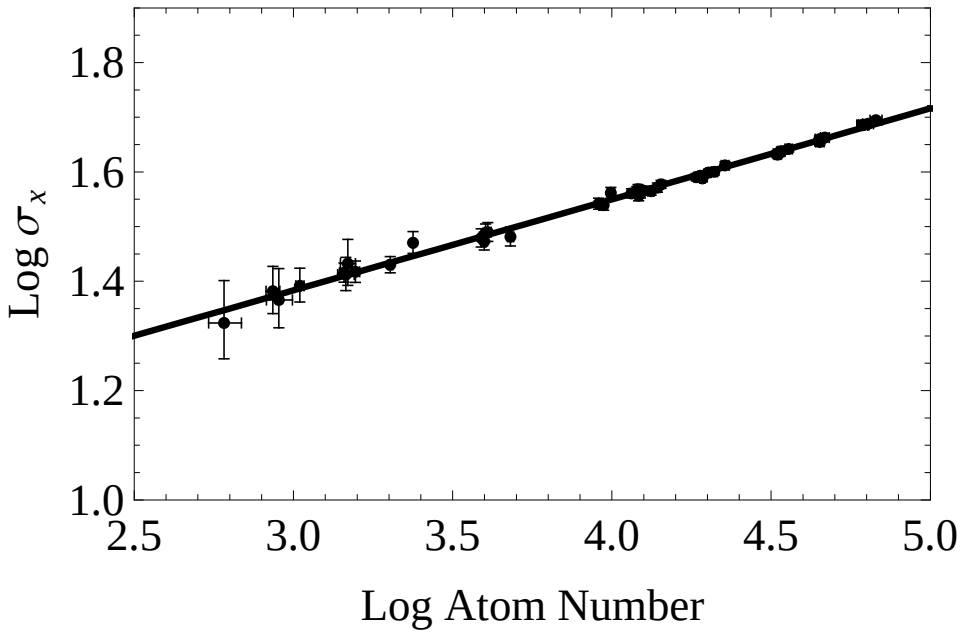

Figure 5.3.2: Axial measurement of the 3D Fermi gas at 834 G. A $\log \sigma(N) = n \log N + a$ curve is fit to the data points where n is left as a free parameter and found to be 0.166(0.01).

$\omega_r/2\pi = 100$ Hz, $\omega_z/2\pi = 24.8$ Hz and the aspect ratio is approximately 4. Applying the same fitting procedure as previously we obtain a value of n=0.166(0.005) which is in good agreement with the theoretical value of 1/6 for an ideal Fermi gas. Figure 5.3.2 shows two data points that sit above and below the slope. This suggest that there are two distinct slopes. Comparing a single straight line fit to the 991 G data shown in figure 5.3.1 the exponent would be $n = 0.195(0.01)$ compared to n=0.166(0.005). This suggests that in the 2D data two slopes are present and only one in the 3D data, otherwise it would be closer to the true 3D value.

5.4 Two dimensional crossover: Transverse cloud size

In the tightly confined direction the behaviour of the cloud width as we reduce the atom number to enter the quasi-2D regime is quite different to that in the weak radial

direction. At large atom numbers the scalings of $N^{1/6}$ at unitarity and for $a < 0$, and $N^{1/5}$ on the BEC side of the Feshbach resonance will still hold. However, as we enter the 2D regime we find that the $1/\sqrt{e}$ Gaussian width asymptotes to a constant value. This lower limit reflects the spread of the lowest transverse harmonic oscillator state of the potential once we enter the 2D regime. Here the density distribution of the cloud changes from a Thomas-Fermi shape to a Gaussian shape with a spatial extent equal to the harmonic oscillator length $a_z = \sqrt{\hbar/m\omega_z}$. The measurements are shown in figure 5.4.1 for a fixed expansion time of 500 μs. In the 2D regime we would assume a Gaussian spatial profile for the gas where the width would be the harmonic oscillator length a_z. We then use the scaling equation $\ddot{b} = \omega_z^2/b_z^2$ discussed in section 5.7.1 where $b_z R_z(t)$ gives the size of the cloud after some expansion time, to obtain the

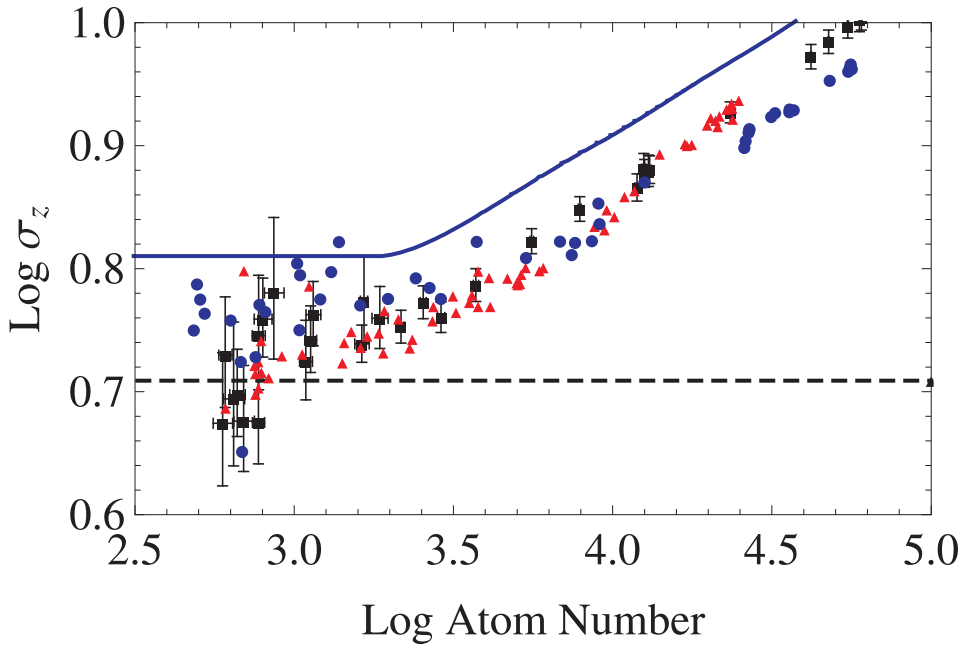

Figure 5.4.1: Observation of the crossover from 3D to 2D in the tight axial direction after a 500 μs expansion time. The data points are black (squares), red (triangles), and blue (circles) for magnetic fields of 810 G, 834 G and 991 G respectively. The dashed black line is the calculated expansion width of the gas in the quasi-2D regime which is determined as $R_z = 0.71$. At 991 G we show the theoretical curve calculated in section 2.9.2. The $\log \sigma(N) = n \log N + a$ fits to the data points of 834 G and 810 G are not shown to improve clarity of the figure.We also show typical error bars on the 810 G data points in both width (vertical error bar) and atom number (horizontal error bar).

calculated expansion widths shown by the dashed black curve in figure 5.4.1. Applying the theoretical curve from section 2.9.2 with a width scaling $b_z(t)R_z(t)$ we find that it does not agree well with the gas trapped in the lowest transverse oscillator state. This could be accounted for by the strong deviations that we observe in the transverse width of the cloud as we approach the quasi-2D limit in section 5.8. It should also be noted from the figure that in the 3D regime the slopes increase differently from the scalings indicated by equations 5.3.3 and 5.3.4. This could be due to the change in collisional behaviour of the interacting gas since we are only populating a few oscillator states. This is described further in section 5.8 on confinement induced resonances. We compare the results again to a gas that has been released from our 3D single beam optical dipole trap as shown in figure 5.4.2 where we have many transverse modes occupied and we see no such plateau. This confirms that the gas confined in the pancake geometry is in a quasi-2D regime.

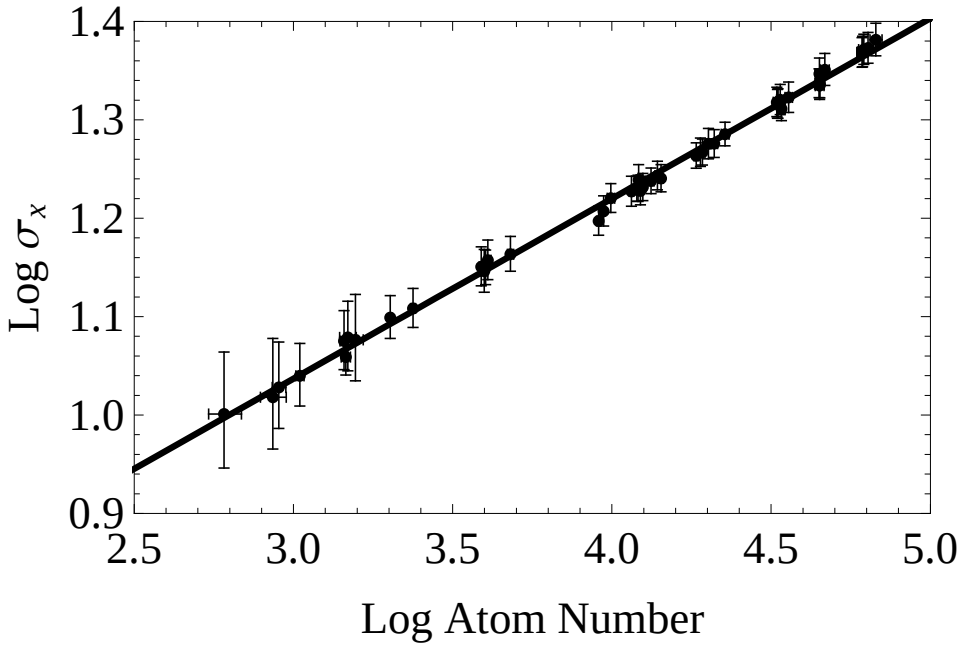

Figure 5.4.2: Axial measurement of the 3D Fermi gas at 834 G. A $\log\sigma(N) = n\log N + a$ curve is fit to the data points where n is left as a free parameter and found to be 0.17(0.01).

5.5 Change of the aspect ratio

A final observation of demonstrating the 2D regime is seen by considering the aspect ratio as we reduce the atom number. In a 3D BEC the aspect ratio both in-trap and after expansion does not depend on the atom number and will remain constant as we reduce the atom number, as shown by the orange data points (open circles) in figure 5.5.1. In the pancake shaped trap the same will apply in the 3D limit of the system, i.e., when the atom number is large. As stated above the Thomas-Fermi parabolic shape changes to a Gaussian shape as we reduce the atom number. In the two dimensional case during expansion the interaction energy is converted almost exclusively into kinetic energy in the tightly confined direction where the weak radial confinement stays almost constant. This then causes the aspect ratio to change as we enter the 2D regime as shown in figure 5.5.1. Here we observe the aspect ratio of the cloud for three different

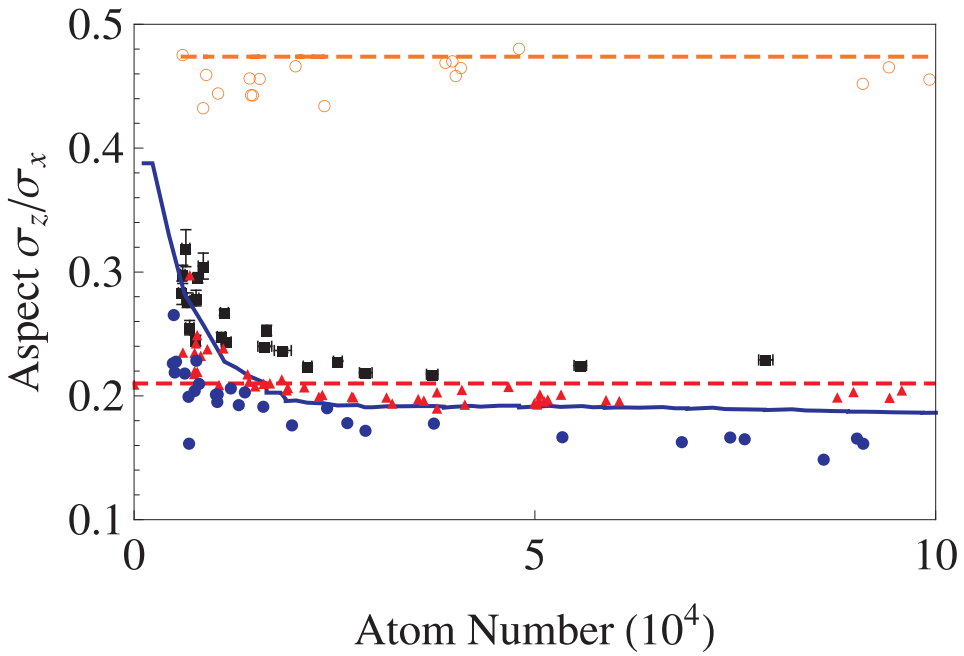

Figure 5.5.1: Measurements of the aspect ratio for an expansion time of 500 μs at three different magnetic fields. The data points are black (squares), red (triangles), and blue (circles) for magnetic fields of 810 G, 834 G and 991 G, respectively. The orange (open circles) are measurements taken for the 3D trap and the dashed orange line is the hydrodynamic expansion for a gas at unitary for a fixed expansion time. The dashed red line is the asymptotic value in the Thomas-Fermi limit.

magnetic fields where the black (squares), red (triangles), and blue (circles) data points are for magnetic fields of 810 G, 834 G and 991 G, respectively. In the BEC case we know the Thomas-Fermi radius in the weakly confining direction from equation 5.3.1. Using the scaling parameters defined above from the pancake shape trap in the Thomas-Fermi regime the aspect ratio is given as $b_z(t)R_z/R_\perp \approx \sqrt{2}\omega_z t$ [131]; this gives AR = 0.21 as shown by the dashed red line in figure 5.5.1, in good agreement with the 810 G data. The blue solid line shows the weakly interacting theory curve which resides slightly above the data. Again applying the approximation shown above for the 3D case, where the expansion time was 2 ms and the trap frequencies are $\omega_r/2\pi = 100$ Hz, $\omega_z/2\pi = 24.8$ Hz, we calculate the constant value to be 0.49(1). This is in good agreement with the experimental data. The change in aspect ratio is clear evidence of entering the 2D regime. The 991 G theoretical curve does not show good agreement with the data. Again this could be due to a change in the collisional behaviour as we only populate a few oscillator states and is discussed in section 5.8.

5.6 Temperature derivation in the 2D trap

To measure the temperature of the strongly interacting gas is not straight forward. Two common methods exist that provide the temperature of a strongly interacting Fermi gas, [16, 132]. The first uses an isentropic magnetic field ramp to image the cloud far away from the Feshbach resonance such that the gas is very weakly interacting. One can then fit a non-interacting gas profile and obtain a temperature. The second method [34] involves fitting an ideal gas profile to a cloud at unitarity. This is valid since the equation of state for a unitary gas is the same as that of a non-interacting one apart from a universal scaling parameter. One can then determine an empirical temperature $\tilde{T}$. The discussion in this section is limited to briefly describing the method to obtain the empirical temperature $\tilde{T}$ [34] and is described in more detail in [82].

We estimate the temperature of our clouds based on an upper limit obtained in the

large atom number regime. Figure 5.6.1 shows a typical absorption image at 834 G in the pancake trap. This is an integrated density distribution in the direction of the resonant imaging beam. We then integrate this in the axial direction to avoid any anharmonicity of the trap in the radial direction. Since several states in the axial direction are occupied it is safe to assume that the density distribution is a Thomas-Fermi distribution with this large atom number. If we were in the 2D regime, i.e., only the lowest transverse harmonic oscillator state is occupied, then we would apply a Gaussian function to this direction and not be able to measure the temperature. After normalisation of the 1D-density profile we obtain the empirical temperature in the following way. To extract the value from the cloud we use the unitary values of $\sigma^* = (1+\beta)^{1/4}\sigma$ and $T_F^* = (1+\beta)^{1/2}T_F$ where σ is the Fermi radius, T_F is the Fermi temperature and β is the universal constant for a three dimensional Fermi gas. We need to obtain σ^* this is found by only fitting the central region of the cloud for σ, and is valid since finite temperature effects are only seen at the wings of the cloud. We can then fit the function [64]

$$n(x,T) = -\frac{3N}{\sqrt{\pi}\sigma_x^*}\left(\tilde{T}\right)^{5/2} Li_{5/2}\Big[-\exp\left(q - \frac{x^2}{(\sigma_x^*)^2\tilde{T}}\right)\Big], \tag{5.6.1}$$

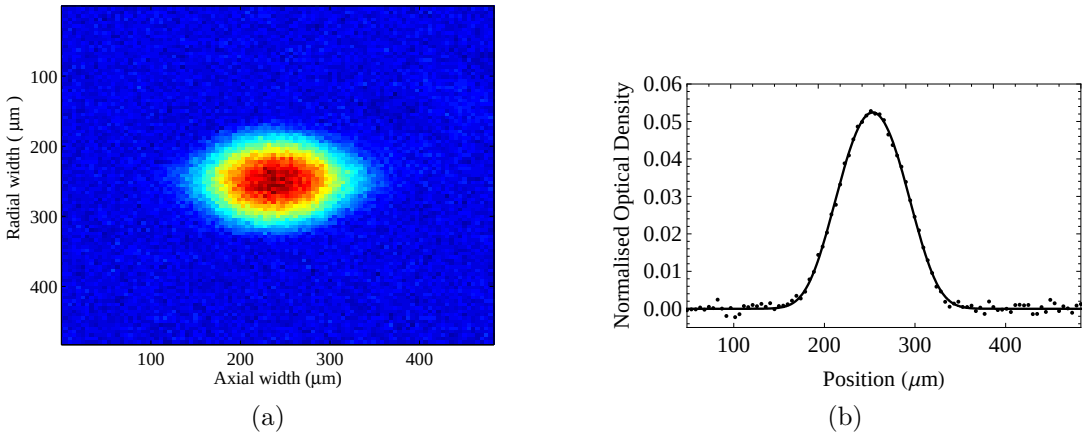

(a) (b)

Figure 5.6.1: The absorption image (a) is integrated in the radial direction to obtain a 1D profile (b). The fit to the profile is a 1D polylogarithm used to obtain the upper limit to the temperature at 834 G, where $T/T_F = 0.085$.

where $Li_{5/2}$ is a 1D polylogarithm. The function is fit to the density profile with q and $\tilde{T}$ as free parameters where for the strongly interacting Fermi gas $q = \mu/E_F\tilde{T}$ and $\tilde{T}$ is given by

$$\tilde{T} = \frac{T}{T_F\sqrt{1+\beta}}. \tag{5.6.2}$$

This gives an empirical temperature $\tilde{T}$ measured in two different traps with tightly confining frequencies of $\omega_z/2\pi = 2951$ Hz and $\omega_z/2\pi = 4151$ Hz being 0.13 and 0.15, respectively. This leads to an upper limit of $T/T_F = 0.09$ and $T/T_F = 0.1$, respectively for the true temperature. These values are only an approximation since they are calculated for a 3D trap and we cannot extract the true 2D temperature.

5.7 Aspect ratio across the BEC-BCS crossover

In section 5.8 we extract information about the cloud width in both the axial and radial directions throughout the Feshbach resonance. This allows us to obtain information on how the aspect ratio varies throughout the crossover. In the following sections the expansion time is 1.5 ms and the lowest achievable atom number is 4000, this is discussed further in section 5.8. Expansion dynamics is a diverse topic and here we concentrate only on what is applicable to our system. For further discussions on this topic that include ballistic expansion the reader is referred to [64].

The first part of this section discusses hydrodynamic expansion in the presence of a magnetic saddle potential since all clouds that are released from our optical trap have a residual magnetic field curvature from the Feshbach coils. The second part shows the aspect ratio across the Feshbach resonance using the calculations of the hydrodynamics in the BEC and BCS regimes to show where the asymptotes would lie at the appropriate time of flight.

5.7.1 Hydrodynamic expansion in the presence of a magnetic field

A gas is said to be in the hydrodynamic regime when the collision rates are high compared to the trapping frequencies. The equations of hydrodynamics describe the expansion of a 3D strongly interacting Fermi gas well. In our system the expansion is not into free space but into a saddle potential caused by the residual magnetic curvature of the Feshbach coils which are left on during imaging. The gas is described in the hydrodynamic regime by the continuity equation for the density and the Euler equation for a velocity field:

$$\frac{\partial n}{\partial t} + \nabla \cdot (nv) = 0 \tag{5.7.1}$$

$$\frac{d\mathbf{v}}{dt} = \frac{m\partial \mathbf{v}}{\partial t} + \nabla \cdot (nv) \tag{5.7.2}$$

where n is the density and v is the velocity. The chemical potential is assumed to have a power law dependence $\mu \propto n^{\gamma}$, where γ is a constant. There exists a scaling solution for the size of the cloud following release from a harmonic trap into a harmonic saddle potential [133]:

$$n(\mathbf{r}, t) = \Big[\prod_{\alpha} b_{\alpha}(t)\Big] n_0\Big(\frac{x}{b_x(t)}, \frac{y}{b_y(t)}, \frac{z}{b_z(t)}\Big). \tag{5.7.3}$$

From a coupled set of differential equations involving the parameters b_i [133]

$$\ddot{b_i} + \omega_i^2 b_i - \Big(\frac{\omega_i^2}{b_i}\Big)\Big(\prod_{\beta} b_{\beta}\Big)^{-\gamma} = 0, \tag{5.7.4}$$

we obtain

$$\ddot{b_i} = -\omega_{m_i}^2 b_i + \frac{\omega_i^2(0)}{b_i \mathcal{V}^{\gamma}} \tag{5.7.5}$$

where ω_{m_i} defines the trapping frequencies for the saddle potential. Depending on whether the atoms are trapped or anti-trapped, these frequencies will be real or imaginary, respectively. In general these equations need to be solved numerically. In our case ω_i is the total trapping frequency of the combined optical and magnetic

potentials. In our experiment, $\omega_{m_{x,y}} = \omega_{x,y}$ and $\omega_{m_z} = i\sqrt{2}\,\omega_{m_z}$. The constant $\gamma = 2/3$ for a Fermi gas at unitarity and in the non-interacting regime and in the BEC limit γ=1. Since the a strongly interacting 3D Fermi gas shows hydrodynamic expansion, we can measure the widths in an experiment and determine the aspect ratio values. Figure 5.7.1 shows the experimental data of such an expansion measurement at unitarity. The aspect ratio is obtained from the ratio of the axial width to the radial (σ_z/σ_x). The solid line in figure 5.7.1 is the theoretical prediction for hydrodynamic expansion for our 2D optical trap frequencies. The theory shows good agreement with the data. The lowest data point is affected by the limit of the optical resolution of our imaging system.

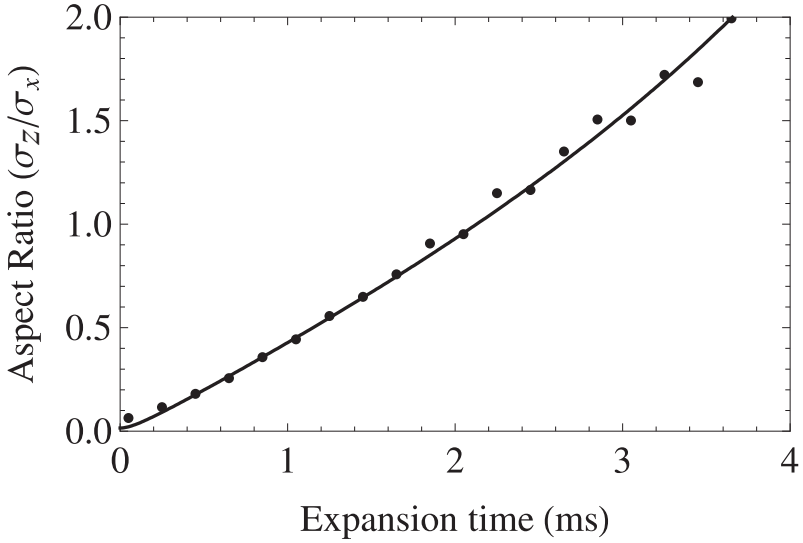

Figure 5.7.1: Observation of the aspect ratio after expansion from the pancake geometry trap containing 10^4 atoms with trapping frequencies $\omega_z/2\pi$ = 2951 Hz, $\omega_y/2\pi$ = 45 Hz, and $\omega_x/2\pi$ = 57 Hz at a magnetic field of 834 G. The solid circles are the data points and the solid line is the hydrodynamic theory fit where the code is from [134].

With equations 5.7.5 in mind we can calculate the expansion of the gas confined to a pancake geometry for a given time of flight and the value of the aspect ratio at unitarity. Figures 5.7.2 and 5.7.3 show the aspect ratios for the three different atom numbers across the BEC-BCS crossover and two different sets of trapping frequencies. As for the previous plots, the blue (circles), red (triangles), and black (squares) are

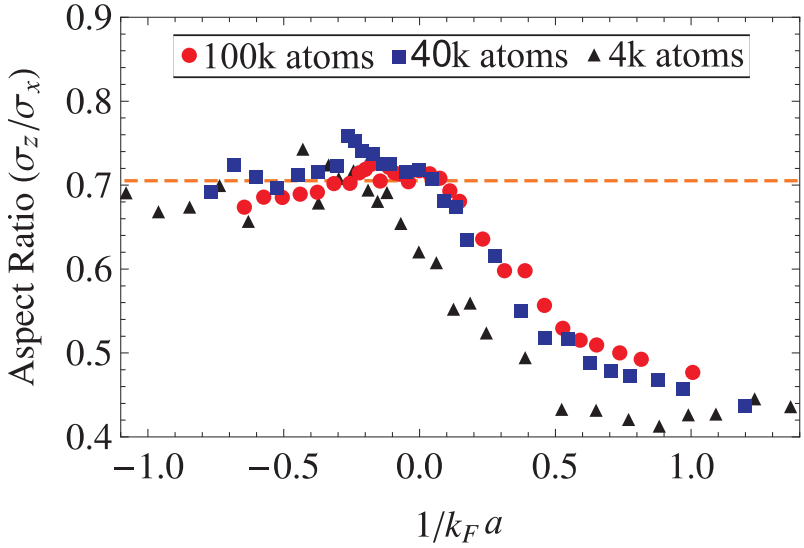

Figure 5.7.2: Aspect ratio of the trap after a fixed expansion time of 1.5 ms. The blue (circles), red (triangles), and black (squares) are data points for 10^5, 4×10^4 and $4{\times}10^3$ atoms, respectively. The trap frequencies are $\omega_z/2\pi = 2951$ Hz, $\omega_y/2\pi = 45$ Hz, and $\omega_x/2\pi = 57$ Hz. The dashed line is the predicted hydrodynamic theory at unitary.

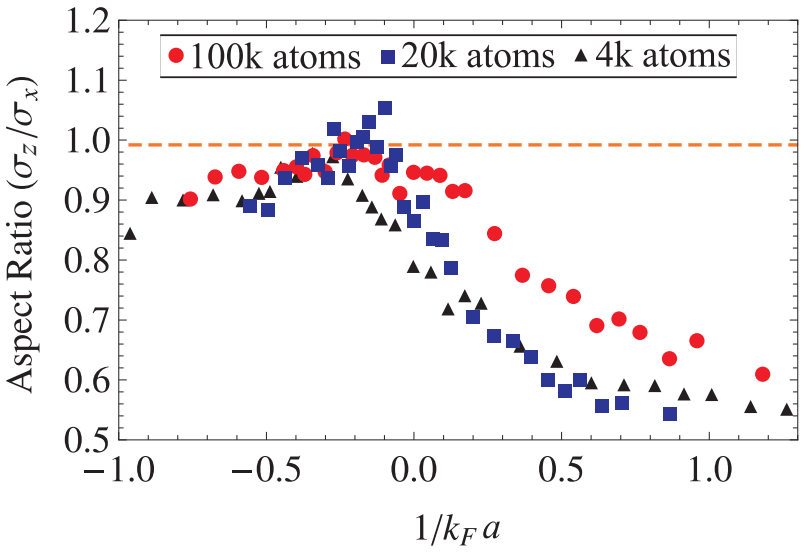

Figure 5.7.3: Aspect ratio of the trap after a fixed expansion time of 1.5 ms. The blue (circles), red (triangles), and black (squares) are data points for 10^5, 2×10^4 and $4{\times}10^3$ atoms, respectively. The trap frequencies are $\omega_z/2\pi = 4157$ Hz, $\omega_y/2\pi = 63$ Hz, and $\omega_x/2\pi = 80$ Hz. The dashed line is the predicted aspect ratio following hydrodynamic theory at unitary

data for 10^5, 4×10^4 and 2×10^4 and $4{\times}10^3$ atoms, respectively. We can observe in these plots that the data departs from the hydrodynamic prediction at negative

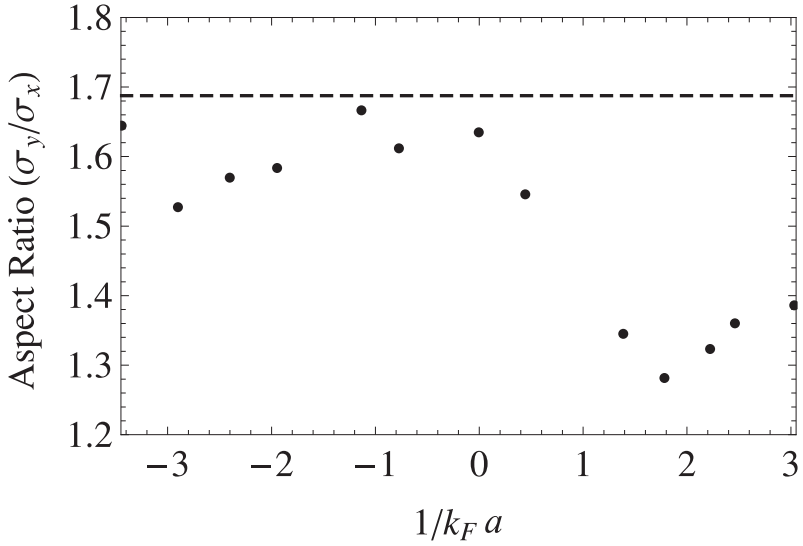

Figure 5.7.4: Aspect ratio of the 3D trap after a fixed expansion time of 6 ms for 4000 atoms. The dashed line is the predicted hydrodynamic theory at unitary.

scattering lengths. This departure is more rapid as we approach the 2D regime and the maximum aspect ratio corresponds to the peak value at the confinement induced resonance discussed in section 5.8. We can also compare the lowest atom number from the pancake trap to our 3D optical trap shown in figure 5.7.4. The change in aspect ratio is observed to take place at ∼834 G where one would expect. This indicates that there is a change in the collisional dynamics in the quasi-2D gas.

5.8 Confinement induced resonances

To study quasi-2D behaviour across the Feshbach resonance we prepare the desired atom number as discussed in section 5.2. Measurements taken of the cloud size in the previous section were obtained with as short a time of flight as possible, keeping the width of the gas above the resolution limit of the imaging. The measurements here use 1.5 ms time of flight. This means the clouds are more dilute and atom numbers above 4000 were used to ensure a sufficiently high imaging signal to noise. At this point we are in the quasi-2D to confinement-dominated 3D regime since $E_F \approx \hbar\omega_z$ and atoms will start to populate excited transverse harmonic oscillator states. Increasing

the atom number we are able to move into a confinement dominated 3D regime, and only for the largest atom numbers do we approach the 3D limit. Comparison with the 3D behaviour is achieved by performing the same measurement from our regular 3D single beam optical dipole trap where the aspect ratio is about 4.

To control the contact interaction strength g_{2D} we change the 3D s-wave scattering length a_{3D} using the broad Feshbach resonance at 834 G. This variation ranges from $a_{3D} \approx +6000a_0$ at 780 G through the pole to $a_{3D} \approx -4000a_0$ at 991 G. A confinement induced resonance should appear when the 3D scattering length is equal to the transverse harmonic oscillator length $a_z = \sqrt{\hbar/m\omega_z}$ where m is the mass and ω_z the transverse trapping frequency. For $\omega_z/2\pi = 2950$ Hz, this resonance should appear at $a_{3D} = 1.03$ μm or 814 G, calculated using equation 2.10.10. Increasing the transverse confinement the induced resonance should shift further to the positive scattering length side of the Feshbach resonace and for $\omega_z/2\pi = 4160$ Hz should appear at $a_{3D} = 828$ nm or 809.4 G.

Figure 5.8.1 shows absorption images of the quasi-2D cloud (a)-(d). The number

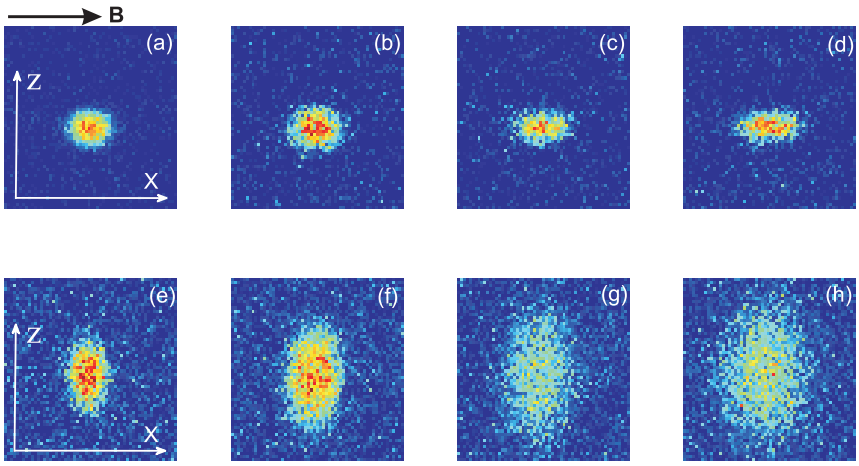

Figure 5.8.1: Images (a)-(d) are of a quasi-2D gas taken across the broad s-wave Feshbach resonance with 2 ms time of flight. Images (e)-(f) are of the cylindrical 3D trap for the same atom number; however the time of flight is much longer at 6 ms. Magnetic fields are, from left to right, 780 G, 820 G, 850 G and 950 G, respectively.

of atoms is $N \sim 4000$ and $T/T_F \leq 0.09$ for four different magnetic field values across the Feshbach resonance. Images (e)-(h) show absorption images of the expanded cloud from the 3D cylindrical trap for the same atom number and magnetic field values. The magnetic fields are, from left to right, 780 G, 820 G, 850 G and 950 G. In the 3D case we see that the width of the cloud in the y direction increases in a monotonic fashion. However, in the quasi-2D case there is a maximum in the width of the tightly confined direction at 820 G and then the gas appears to narrow again at 850 G and beyond. The width in the weakly confined direction increases monotonically. We show

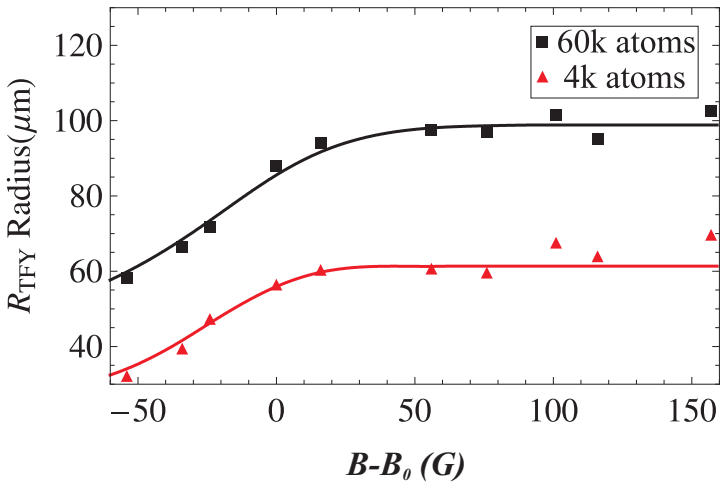

Figure 5.8.2: Variation of cloud width in the y direction across the Feshbach resonance for the 3D case with a fixed expansion time of 6 ms.

the 3D case in figure 5.8.2 for a fixed expansion time of 6 ms and trap frequencies of $\omega_r/2\pi = 100$ Hz, $\omega_z/2\pi = 24.8$ Hz. We observe the width increasing monotonically across the Feshbach resonance to a constant value in the BCS limit. This has also been observed for three dimensional Fermi gases by Tarruell *et al.* [102]. This is in stark contrast to our observations in a quasi-2D Fermi gas. Figures 5.8.3 and 5.8.4 show the measured Thomas-Fermi radius R_{TFZ} in the axial direction versus the magnetic field. We observe the size of the gas at various magnetic fields across the resonance through absorption images at a fixed expansion time of 1.5 ms and $T/T_F \leq 0.09$. For the quasi-2D case each point is an average of 10 individual images whereas for the larger atom numbers they are averages of 3 images. The size of the cloud is extracted

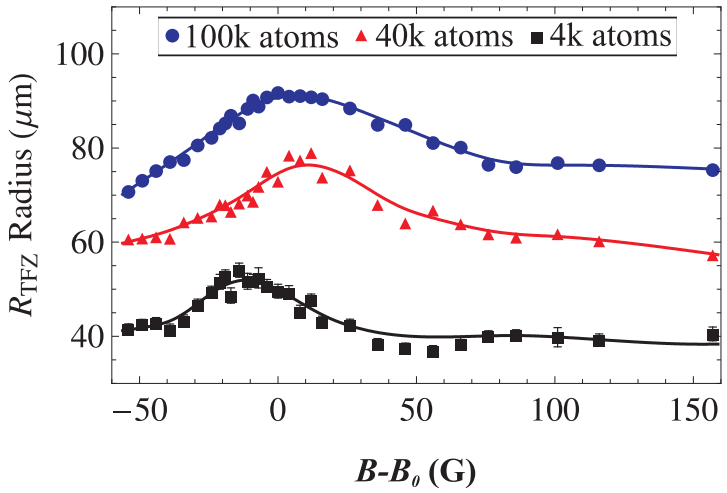

Figure 5.8.3: Observation of the tightly confined width behaviour for a fixed expansion time of 1.5 ms. The blue (circles), red (triangles), and black (squares) are data points for 10^5, 4×10^4 and $4{\times}10^3$ atoms, respectively. The trap frequencies are $\omega_z/2\pi =$ 2951 Hz, $\omega_y/2\pi = 45$ Hz, and $\omega_x/2\pi = 57$ Hz. As we move across the Feshbach resonance there is a large deviation from the usual monotonic increase in the width as observed in figure 5.8.2. As we reduce the atom number to enter the quasi-2D regime the width narrows and moves further to the BEC side of the broad Feshbach resonance at 834 G. The curves shown serve only to guide the eye.

using a Thomas-Fermi fit in both the radial and axial directions. Figure 5.8.3 shows the width of the cloud in the tightly confined direction. The trapping frequencies were $\omega_z/2\pi = 2950$ Hz, $\omega_y/2\pi = 45$ Hz and $\omega_x/2\pi = 57$ Hz. The three data sets are: blue (circles), red (triangles), and black (squares) for 10^5, 4×10^4 and $4{\times}10^3$ atoms, respectively. We see that this data reflects what is shown qualitatively in figure 5.8.1. At large N the width initially increases in a monotonic fashion like the 3D resonance but then decreases. A similar behaviour is seen at $N = 4 \times 10^4$. However, the central peak shifts in the opposite direction to what we expect. Although it is not fully understood it may be due to the shell structure and most probably collision energies for this trap and atom number. As we lower the atom number further and approach the quasi-2D regime the maximum of the width is observed on the BEC side of the Feshbach resonance and the width of the peak has narrowed significantly. Figure 5.8.4 shows a similar behaviour where the main difference in the conditions are the trapping frequencies, which are $\omega_z/2\pi =$4160 Hz, $\omega_y/2\pi =$60 Hz and $\omega_x/2\pi =$83 Hz. The peak

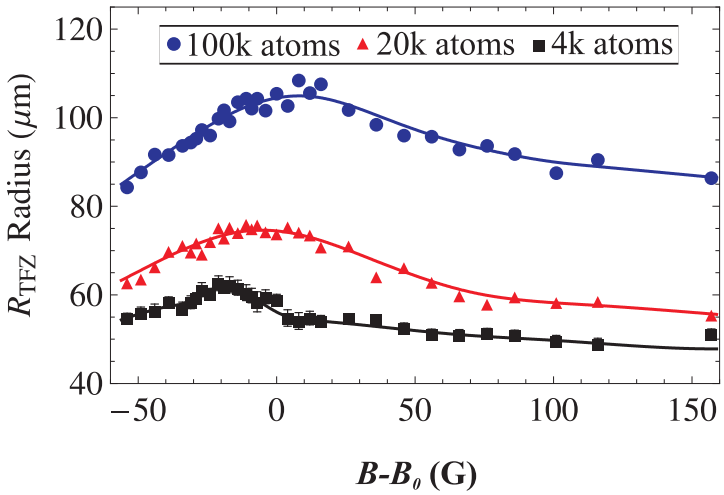

Figure 5.8.4: Observation of the tightly confined width behaviour for a fixed expansion time of 1.5 ms. The blue (circles), red (triangles), and black (squares) are data points for 10^5, 2×10^4 and $4{\times}10^3$ atoms, respectively. The trap frequencies are $\omega_z/2\pi = 4157$ Hz, $\omega_y/2\pi = 63$ Hz, and $\omega_x/2\pi = 80$ Hz. As we move across the Feshbach resonance there is a large deviation from the usual monotonic increase in the width as observed in figure 5.8.2. As we reduce the atom number to enter the quasi-2D regime the width narrows and moves further to the BEC side of the broad Feshbach resonance at 834 G. The curves shown serve only to guide the eye.

in the width with 10^5 atoms shifts to negative scattering lengths. Again a quantitative understanding of this peak shift is missing but may arise from higher energy collisions accessing resonances with higher lying transverse modes. We also see that in the intermediate regime the maximum position of the peak has shifted towards positive a which is what we would expect for a confinement induced resonance. In figure 5.8.5 we show an enlarged picture of the quasi-2D widths with a single Lorentzian fit to each set of data that determines the centre of the peak. The black (squares) and red (triangles) are data points for trapping frequencies $\omega_z/2\pi = 4160$ Hz and $\omega_z/2\pi = 2950$ Hz, respectively. The two vertical dashed lines indicate the magnetic field value for each peak where the dashed black line is for the lower trap frequency and is at the s-wave scattering length $a \approx 26600a_0$, or 819(1) G, and the dashed red line is at the s-wave scattering length $a \approx 21700a_0$, or 816(1) G, where a_0 is the Bohr radius. It is clear that the extra confinement of the gas modifies the dynamics of the expansion in a non-trivial way not observed in a 3D degenerate Fermi gas. We interpret this increase in

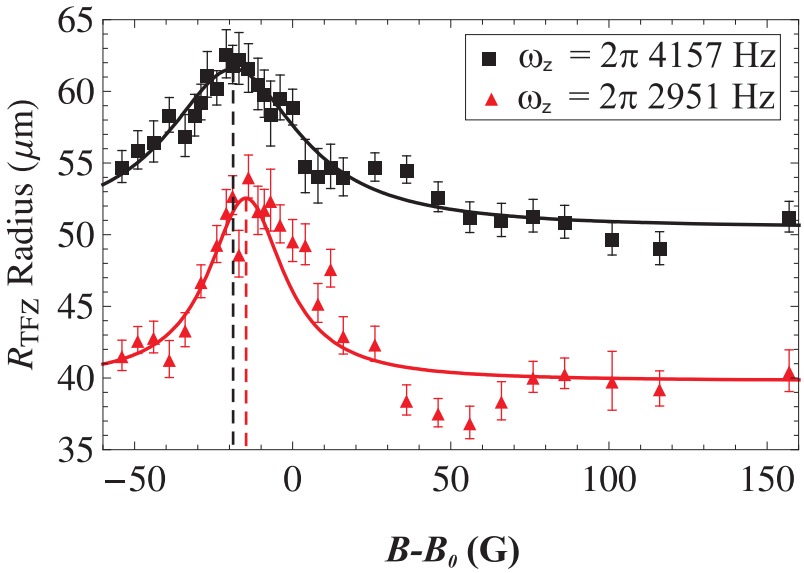

Figure 5.8.5: Enlargement of the observed width behaviour in a quasi-2D gas at a fixed expansion time of 1.5 ms for 4000 atoms. The black (squares) and red (circles) are data points for trapping frequencies $\omega_z/2\pi = 2951$ Hz and $\omega_z/2\pi = 4157$ Hz respectively. To find the central peak we apply a Lorenztian fit and extract the centre value of 819 G and 816 G which agrees well with the calculated values.

the cloud width near the centre of the Feshbach resonace as arising from the population of the transverse modes with higher vibrational states. This could be explained by a confinement induced resonance in which the threshold energy of two colliding ground state atoms becomes resonant with molecules in the first excited state at a particular value of the scattering length. This concept is depicted in figure 5.8.6. When the ground state continuum, $E_{c,g}$, of the open channel coincides with the binding energy of a molecule in the first transverse excited state we expect a confinement induced resonance to occur.

The calculated positions of the resonance are at 810 G and 814 G for 4157 Hz and 2951 Hz respectively. Although we do not see the experimental peak in the calculated position it is close to the expected values and shifts in the right way as we increase the tight confinement. Also the calculated values assume only the lowest transverse oscillator state to be occupied and this is not the case for 4000 atoms. Further experiments and theoretical analysis are needed to exactly understand the origin of the peak and its position. This is discussed further in the outlook 6.2.

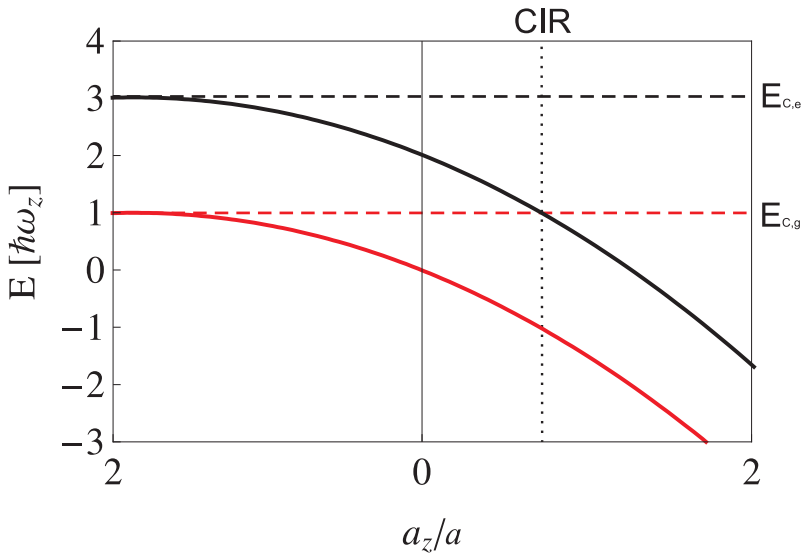

Figure 5.8.6: Pictorial representation of the confinement induced resonance (CIR). The red curve is the binding energy of the ground state and the black curve the binding energy of the excited state. When $a_z = a$ the ground state free atom continuum crosses the bound state with one quantum of excitation. This (avoided) level gives rise to a scattering resonance.

Since the resonance feature is a consequence of the tight confinement, we would expect that in the weakly confined direction there would be no such feature. Figure 5.8.7 shows the width for the weakly confined direction of the 2D trap where we see no such resonance. Instead, the behaviour in the width of the 2D gas is similar to that of the three dimensional gas. In a recent theoretical paper Lin *et al.* [1] describe the Thomas Fermi cloud size in a quasi-2D Fermi gas across the BEC-BCS crossover for a fixed particle number. Their inclusion of the dressed molecule states, which derive from the fact that atoms will populate the transverse excited states throughout the Feshbach resonance, results in a monotonic increase from the BEC limit to the BCS limit. The data sets in figure 5.8.8 show the normalised Thomas Fermi radius at two different trapping frequencies, $\omega_z/2\pi = 2951$ Hz and $\omega_z/2\pi = 4151$ Hz, respectively. In both sets of data we observe a monotonic increase from the BEC side of the resonance to a limiting value in the BCS regime. This shows that the description given in terms of dressed state molecules should be appropriate. These data show qualitative agreement with the theory [1] but not exact quantitative agreement. This is most likely due to

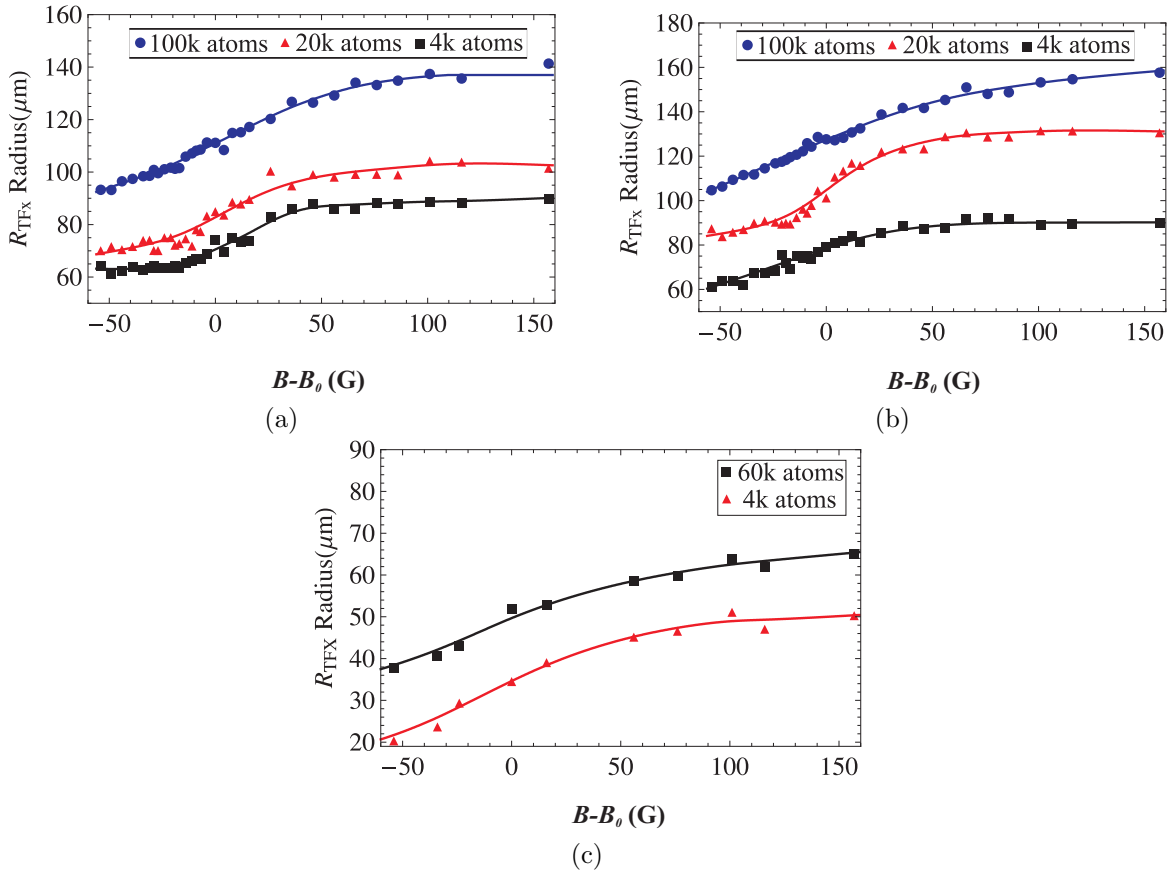

Figure 5.8.7: Observed width in the weakly confined x direction for a fixed expansion time of 1.5 ms. The blue (circles), red (triangles), and black (squares) are data points for 10^5, 2×10^4 and $4{\times}10^3$ atoms, respectively. (a) shows the behaviour for trap frequencies of $\omega_z/2\pi = 2951$ Hz, $\omega_y/2\pi = 45$ Hz, and $\omega_x/2\pi = 57$ Hz, (b) shows the behaviour for trap frequencies of $\omega_z/2\pi = 4157$ Hz, $\omega_y/2\pi = 63$ Hz, and $\omega_x/2\pi = 80$ Hz, and (c) shows the behaviour for the 3D trap with a fixed expansion time of 6 ms. As we move across the Feshbach resonance, in contrast to the tight confinement, we observe a monotonic increase similar to the 3D trap. The curves shown serve only to guide the eye.

the fact that the theory considered the highly 2D limit ($\hbar\omega_z \gg E_F$) whereas in our experiment $E_F \approx \hbar\omega_z$.

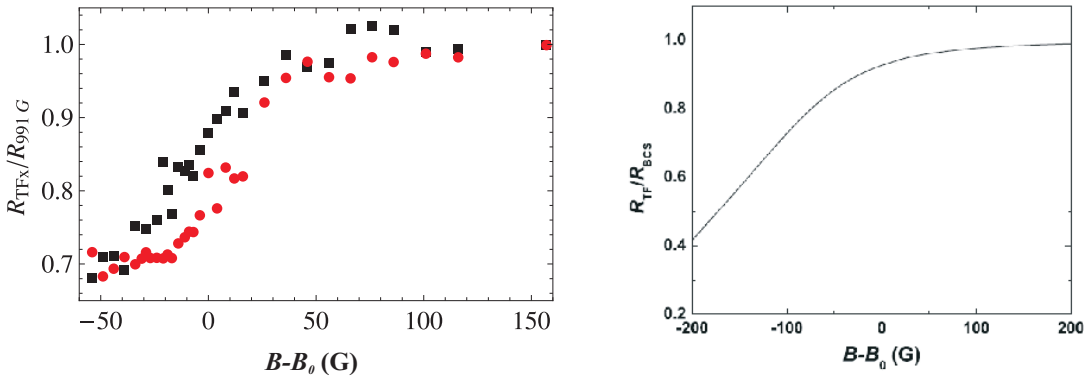

Figure 5.8.8: Thomas-Fermi width in the radial direction after a fixed expansion time of 1.5 ms, where the black (squares) and red (circles) are the data points for $\omega_z/2\pi = 2951$ Hz and $\omega_z/2\pi = 4157$ Hz respectively. In (a) the data is normalised to the width at 991 G. We see that the width is a monotonically increasing function as described by the effective 2D Hamitonian given in [1]. In figure (b) we show the normalised width described in the paper. The figure is reproduced from [1].

5.9 Summary

This chapter describes the first experiments carried out across the broad ^{6}Li Feshbach resonance in a quasi-2D interacting Fermi gas. Evidence for the crossover from a 3D interacting Fermi gas to a 2D interacting Fermi gas is obtained through measurements of the cloud widths versus atom number at three different magnetic fields. The clearest signature is observed at 991 G where the cloud behaves similarly to that of a weakly interacting Fermi gas and we are able to apply the non-interacting model of section 2.9.2 which fits the data well in the weakly confining direction. Using the Feshbach resonance to control the contact interaction across the BEC-BCS crossover as we enter the 2D regime we find that there is a significant deviation in the width. Where an increase in the transverse width of the cloud after expansion indicates the population of higher lying vibrational levels. This fits well with the concept of a confinement induced resonance. The positions of the peak in widths fit qualitatively to the calculation of a pole existing when a_{3D}=a_z. However, to be able to explicitly state this more detailed experiments and theoretical analysis is needed. In the weakly confined direction no such peak is observed. Instead the width behaves similarly to that of a 3D Fermi gas

and is also consistent with the theoretical work carried out by Lin *et al.*[1].

It is also clear from the scatter in the data observed in crossing from 3D to 2D that there are limitations in our system. A clear way to improve the experiments would be to increase the aspect ratio of the trap which would make the 2D regime accessible with larger atom numbers, reducing the need to average (up to 30) images in order to extract qualitative information. These are discussed in the appendix.

Chapter 6

Conclusion and outlook

6.1 Summary

This thesis describes the first experimental investigation of a quasi-2D Fermi gas near the broad ^{6}Li Feshbach resonance. Before the study of a quasi-2D Fermi gas could take place we had to design and construct the 2D optical trap. To form a quasi-2D cloud we start by creating molecular Bose-Einstein condensates and degenerate Fermi gases of ^{6}Li in our regular, 3D, single beam optical dipole trap formed by a 100 W fibre laser. At the broad 834 G Feshbach resonance evaporation takes place through reduction of the dipole trap laser power. On the BEC side of the Feshbach resonance three body recombination leads to the formation of molecules which can undergo Bose condensation to form a molecular BEC. Through a sweep of the magnetic field to values of negative scattering length we can form weakly or strongly interacting Fermi gases. We can then transfer the cloud into the 2D optical trap. The main theory needed to understand the experiments in both 3D and 2D has been summarised. The following sections summarise the main experimental results and look towards future experiments that would help to resolve outstanding issues.

From three dimensions to two dimensions - To enter the quasi-2D regime we load ultracold atoms from the 3D trap into a 2D laser light sheet formed by an elliptical Gaussian beam produced by tightly focusing a circular beam in one direction with a cylindrical lens. By reducing the atom number we are able to cross over from 3D to 2D. We observe the transition to a 2D gas through different scalings of the radial and axial widths in the 3D and 2D regimes. This is particularly clear at a magnetic field of 991 G where the gas behaves like a weakly interacting degenerate Fermi gas. We also observe a change in the aspect ratio as a function of the atom number which does not occur in a 3D quantum degenerate gas. The transition point appears to occur when the atom number reaches ~ 2000 although due to the noise on the data this is difficult to quantify with high accuracy. This value does, however, coincide roughly with the calculation for a non-interacting Fermi gas.

Confinement induced resonance - A key result of this thesis is the preliminary indications of a confinement induced resonance in a quasi-2D Fermi gas [135]. We have observed a significant difference in the width after expansion of the quasi-2D Fermi cloud across the Feshbach resonance compared to the 3D degenerate Fermi gas. Through measurements of the width in the tightly confining direction after a fixed expansion time we observe a peak at 819(1) G for a trapping frequency of $\omega_z/2\pi = 2950$ Hz. Increasing the tight axial confinement we observe a shift in the peak position to 816(1) G at a trapping frequency of $\omega_z/2\pi = 4160$ Hz. These values are close to the point where $a_z = a_{3D}$. We interpret this increase in the cloud width as arising from the population of the transverse modes with molecules in higher vibrational states. This could be readily explained by a confinement induced resonance where the threshold energy of two colliding ground state atoms becomes resonant with molecules in the first excited state leading to an increase in the energy in the tightly confined direction. In the weakly confined direction there is no such increase in the width which instead behaves similarly to the 3D case and increases monotonically across the Feshbach resonance. Such behaviour of the width in the weakly confined direction is consistent with the theoretical work of Lin *et al.* [1]. However, further experiments and a full

theoretical description of the width in the tightly confining direction is needed to verify this interpretation.

6.2 Outlook

With the proposed improvements discussed in the appendix we would be able to increase the critical particle number and better study the effects of reduced dimensionality. In the following three sections proposed directions are discussed.

Further investigation of a confinement induced resonance: The experiments indicating the confinement induced resonance in this thesis were all carried out with a fixed hold time of 100 ms before being released from the optical trap and imaged. Studying the widths using a range of hold times would indicate if the system is in equilibrium or if it is continually evolving. From the equilibrium width increases we may be able to determine the fraction of excited state molecules as a function of magnetic field.

We have already seen that there is a shift in the peak position of the width as the tight confinement frequency is increased which qualitatively agrees with the expected resonance shift. To investigate this further it is possible to vary the tight confinement trap frequency from low to high and measure the dependence on trap frequency. Ideally, measurements with smaller atom numbers would allow us to isolate only the lowest transverse oscillator state. This would provide further evidence of a confinement induced resonance. These measurements are currently on-going in our laboratory.

p-wave molecules in 2D: This thesis has only been concerned with s-wave collisions between fermionic particles using the broad ^{6}Li Feshbach resonance. However, this is not the only type of resonance that exists. It is possible to form molecules using a p-wave Feshbach resonance. In previous work on p-wave Feshbach

resonances [136, 137, 138, 139] it has been experimentally shown that the lifetime of the p-wave molecules is short, on the order of, 2-20 ms. This is due to atom-molecule and molecule-molecule relaxation, where an atom scatters from a molecule which falls into a deeply bound state and the resultant kinetic energy, which can be large, is shared between the atom and the molecule. This process is inhibited by the Pauli principle for a s-wave superfluid, but not for p-wave interactions. It has been proposed [140] that a p-wave superfluid would be more stable in a 2D system as is briefly summarised below. The lifetime of a p-wave molecular condensate in 3D is given by [140] as

$$\Gamma_{3D} \sim \frac{\hbar}{ml^2}\frac{R_e}{l} \tag{6.2.1}$$

where R_e is the van der Waals length, m is the mass, and l is the interatomic separation. It is then shown that for a Fermi energy of $\sim$10 kHz the lifetime is only 20 ms, whereas the lifetime of a s-wave molecular condensate is orders of magnitude longer. In the case of a quasi-2D system where the width of the tight confinement d is much less than l, but $d > R_e$, the decay rate is given by [140] as

$$\Gamma_{Q2D} \sim \frac{\hbar}{ml^2}\frac{R_e}{d}. \tag{6.2.2}$$

At first glance this appears to be faster than the 3D case; however, when taking into account the typical interaction energy given for a 2D case as

$$E_{2D} \sim \frac{\hbar}{ml^2}\frac{1}{\ln\left(\frac{l}{R_e}\right)} \tag{6.2.3}$$

it is shown that the interaction energy in a quasi-2D system can be made much larger than in 3D and in fact larger than the decay rates. This may allow for the formation of a p-wave molecular condensate in the strongly interacting region [140]. In [136] we studied the properties of p-wave Feshbach molecules and presented the measurements of the binding energies of molecules in all

three possible combinations of $|F = 1/2, m_f = +1/2\rangle$ and $|F = 1/2, m_f = -1/2\rangle$ states. With our ability to control the magnetic fields and measure p-wave resonances with a precision of 10 mG, transferring the gas into the pancake geometry may allow us to form longer lived molecules and possibly a p-wave superfluid. We could also envisage the use of Bragg spectroscopy to detect the molecule formation [141].

Observation of BKT transition in a Fermi gas: In section 2.11 we discussed some of the experiments that have reported observations of the BKT transition in a Bose gas. So far the creation of the BKT transition in an interacting Fermi gas has not been achieved. Theoretically it has been shown in [117, 142] that the evolution of the BKT transition temperature varies across the Feshbach resonance to a limiting value on the BEC side of the resonance. Zhang *et al.* [117] were able to show that in the radial plane of the quasi-2D gas there is a sudden jump in the superfluid density that occurs where the superfluid meets the normal fluid. This is characteristic of the BKT transition. It is also shown that the as we move from an s-wave scattering length of $a < 0$ to $a > 0$ the limiting transition temperature for the BKT transition is reached whilst still on the BCS side of the Feshbach resonance. This can be understood through the existence of a two-body bound state for a scattering length of any sign in a lower dimensional gas. With our Bragg spectroscopy technique it may be possible to detect these two-body bound pairs at unitarity and on the BCS side of the Feshbach resonance where we would expect a larger pairing signal than in the 3D case [141].

Appendix A

Improving the atom number in 2D

A.1 Introduction

From the preceding investigation it is apparent that there are a number of limitations to our current experimental system. Due to the relatively low aspect ratio we require the atom number to be below ∼2000 to enter the 2D regime. Obtaining high quality, reliable images of such low atom numbers can be problematic. The most obvious solution is to improve the signal to noise of the imaging system. However, this would still leave us with a small atom number when crossing over to a two dimensional regime. Instead, we would like to increase the aspect ratio such that we have a much larger atom number. The critical atom number grows with the square of the aspect ratio so there is the potential for larger gains to be made and subsequently a better signal to noise level.

Another limitation of our system is the residual magnetic field curvature of the Feshbach coils. As seen in section 4.4 we have a residual magnetic field curvature that produces a trapping frequency $\omega_r/2\pi = 24.8(1)$ Hz in the radial direction and an anti-trapping of $\omega_z/2\pi = i34(1)$ Hz in the axial direction. This places a lower limit on the radial confinement and reduces the largest aspect ratio achievable. To overcome these

problems we could change the trapping potential to increase the trapping frequency in the tightly confined direction. Two methods based upon the work of [52] and [143] to achieve this, are described in sections A.3 and A.4. We could also modify the Feshbach coils to control the amount of field curvature, described in section A.2. With this control it would be possible to vary the weak confinement rather than the atom number to enter the quasi-2D regime. If we reduced the weak confinement of the optical potential below that of the Feshbach field curvature this direction would be dominated by the magnetic trapping potential. This would have the advantage of forming a very harmonic trap because of the large size of the Feshbach coils.

A.2 Modification of the Feshbach coils

The control over the residual magnetic field curvature is not a difficult problem per se; however the amount of variation will be limited. To vary the curvature we can add a set of coils that work in a Helmholtz configuration but the current would flow in the opposite direction to the Feshbach coils, shown in figure A.2.1. We can estimate trapping frequencies that are created by the Feshbach field curvature through a numerical simulation of the magnetic fields. Figure A.2.2 shows a parabolic fit to magnetic field of the Feshbach coils that were simulated using [144]. It is possible from the fit coefficient of the parabola to extract the trapping frequencies. Since we can equate the magnetic field to a harmonic oscillator given as

$$\frac{1}{2}\frac{\partial^2}{\partial z^2}(\mu_B \cdot \mathbf{B})z^2 = \frac{1}{2}m\omega_y^2 y^2. \tag{A.2.1}$$

Solving gives the trapping frequency $\omega_z/2\pi = i33.9$ Hz and $\omega_r = 23.6$ Hz which are very close to the values experimentally obtained in section 4.4. The curvature compensation coils will create an inverted version of the Feshbach coils with larger curvature for the same applied field. The addition of the two fields will reduce the overall field curvature in both the radial and axial trapping directions. These two fields then form

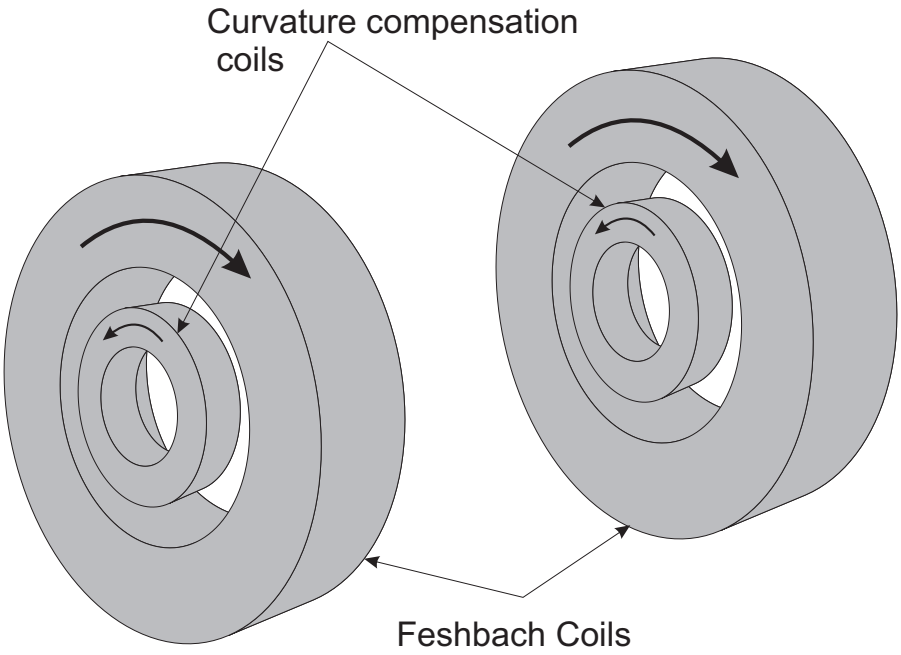

Figure A.2.1: Schematic of the current carrying Feshbach coils with a curvature compensation coil placed inside to reduce the magnetic field gradient produced by the Feshbach coils.

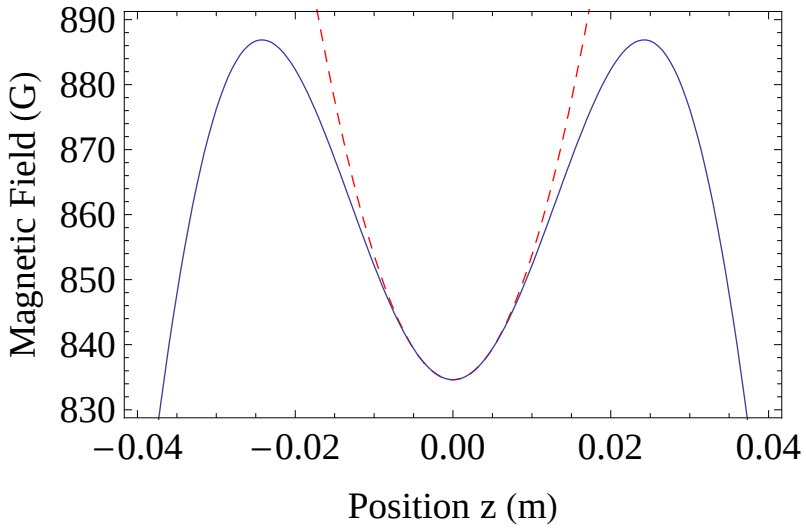

Figure A.2.2: Calculated magnetic field in the axial direction versus position from the centre of the coils. The dashed curve is a parabolic fit to the field curvature and the solid line is the theoretical calculation.

the magnetic field shown in figure A.2.3. Calculation of the trapping frequencies for an applied current of 20 amps gives $\omega_r/2\pi = 6$ Hz and $\omega_z/2\pi = i8.5$ Hz which can be varied with the current. Depending on how much current we apply it is possible

to swap the trapping direction such that the radial direction is anti-trapped and the axial direction is trapped. Applying this to our present set-up we could increase the aspect ratio from 60 to approximately 80 by applying 40 amps to the compensating coils. This change would increase the atom number in the quasi-2D regime to ∼3200 applying equation 2.9.10. This however, is not a large change. Changing the optical trap from a red detuned system to a blue detuned trap would allow much larger aspect ratios to be obtained.

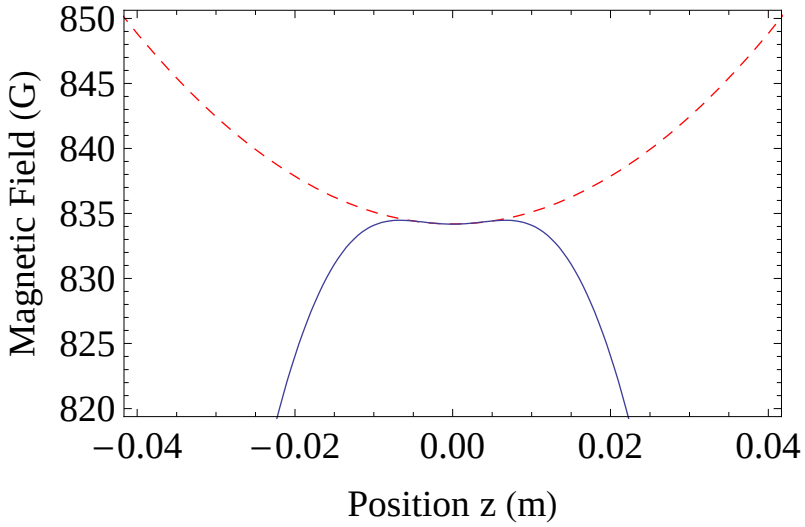

Figure A.2.3: The combined magnetic field for the Feshbach coils and the curvature compensation coils. We can see that there is far less curvature than previous.

A.3 Blue detuned lattice

An optical lattice is formed by the interference of two laser beams which intersect at some angle. In general this can be achieved through an angle of $0 < \theta < 180°$. Depending on the wavelength of the light used to form the lattice we can have atoms trapped at an intensity minima or maxima. For our consideration we wish to have the atoms trapped in a minima and therefore the formation of a lattice would be achieved with a blue detuned laser at a wavelength of $\lambda = 532$ nm. Using a combination of a blue detuned lattice with the residual curvature of our current Feshbach coils would

allow us to trap atoms in all three dimensions. The advantage of using a lattice is the very tight confinement that can be created, but tunneling between lattice sites has to be avoided. This will place a lower limit on the distance between each site and the trapping frequency we could obtain. Additionally the observation of just one site would require the removal of atoms from the other lattice sites and this is not an easy task.

In our set-up we could create a lattice by intersecting two laser beams at an angle of $\theta = 72^\circ$ or lower. This would allow access to lattice spacings of $d = 452$ nm and above, where $d = \lambda/(2\sin\theta/2)$. Calculation of the frequencies is considered as in section 3.4. The interference pattern varies sinusoidally where the maximum is given by $I = 8P/\pi w^2$ with periodicity d as shown in figure A.3.1a. By using equation 3.4.3 we can determine the lattice potential given as

$$U(x) = U_0 \sin^2 k_l x \tag{A.3.1}$$

where $k_l = (2\pi \sin\theta/2)\lambda$ is the wave number and U_0 the potential depth. The trap frequencies in the radial direction are simply given by the same formula as the Gaussian beam. The main difference is that we are now anti-trapped in this direction. For a $1/e^2$ waist of 500 μm we obtain $\omega_x/2\pi = i1$ Hz and $\omega_y/2\pi = i0.4$ Hz and would be dominated by the magnetic field curvature of 24.8 Hz. For the axial direction the trap frequency is given by

$$\omega_z = \sqrt{\frac{2U_0 k_l^2}{m}}. \tag{A.3.2}$$

For a spacing of 3 μm this gives $\omega_z/2\pi = 63$kHz. The tunneling can be written in terms of the trap depth and recoil energy of the lattice $E_R = \hbar^2 k^2/2m$ where m is the mass, k is the wavevector, given by [145], is

$$J = E_R \Big(\frac{U_0}{E_R}\Big)^{(3/4)} \exp(-2\sqrt{U_0/E_R}). \tag{A.3.3}$$

Applying this equation we obtain a tunneling time of 10^{14} seconds for 10^5 atoms

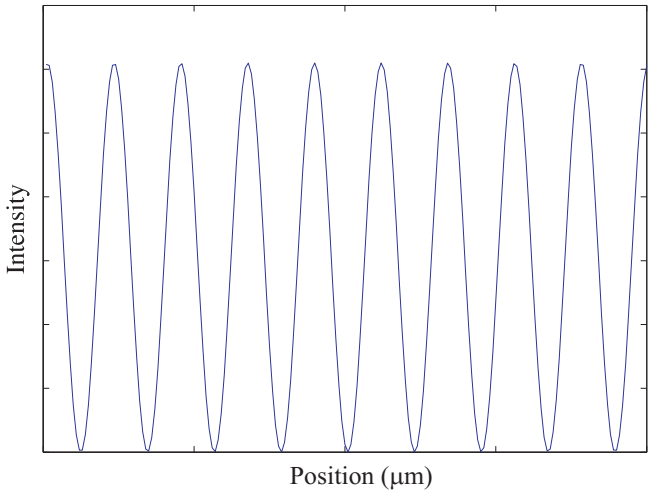

(a)

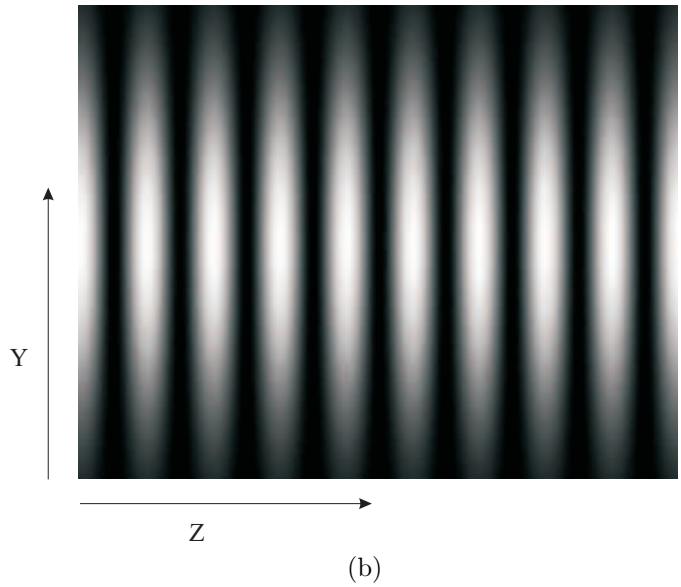

(b)

Figure A.3.1: (a) Intensity profile from a one dimensional lattice, (b) two dimensional intensity pattern.

which is long on the time scale of the experiment. It can be seen that using an optical lattice can generate very high trapping frequencies and very large aspect ratios; however addressability is a very difficult issue. In [52] they used the technique of forced evaporation to remove atoms from the other lattice sites. This does not work for the lowest hyperfine states of lithium. So the preferred approach would be to create a Hermite-Gaussian TEM01 mode. This removes the addressability issue as atoms

would be confined to only one site using a combination of the optical potential with the curvature of the magnetic fields in the radial direction.

A.4 Blue detuned TEM01 mode

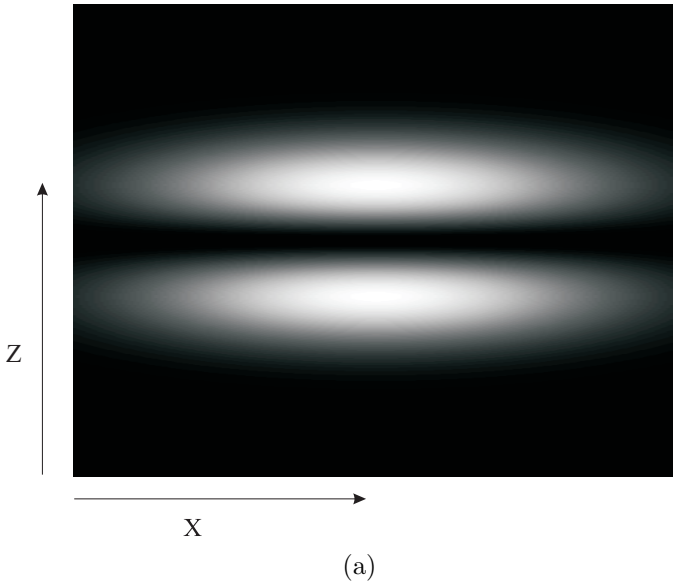

(a)

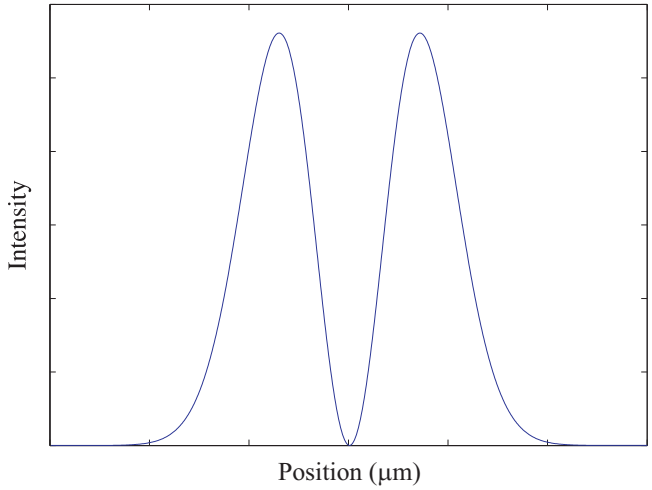

(b)

Figure A.4.1: (a) Intensity profile of a Hermite-Gaussian TEM01 mode, (b) two dimensional intensity pattern.

The common Gaussian beam used in laser optics is part of a family of solutions to the paraxial equations known as Hermite-Gaussian (HG) beam solutions. We can write out the intensity distribution for the TEM01 mode in the focal plane as [146]

$$I(x,y) = \frac{8Px^2}{\pi W_x^3 W_y} \exp\Big(- \frac{2x^2}{W_x^2} - \frac{2y^2}{W_y^2}\Big) \tag{A.4.1}$$

where P is the power and W_x, W_y are the $1/e^2$ Gaussian beam waists and is shown in figure A.4.1. To calculate the potential and the trap frequencies we apply equation 3.4.3 again, this gives

$$U(x,y) = U_0 \frac{2x^2}{W_x^2} \exp\Big(- \frac{2x^2}{W_x^2} - \frac{2y^2}{W_y^2}\Big) \tag{A.4.2}$$

where U_0 is the potential depth given in equation 3.4.3. By setting $y = 0$ in equation A.4.2 we can find the trap frequencies in this direction giving

$$\frac{\omega_y}{2\pi} = \sqrt{\frac{U_0}{\pi^2 m W_y^2}}. \tag{A.4.3}$$

If we assume a $1/e^2$ waist in the axial direction of 8 μm and in the radial direction a $1/e^2$ width 400 μm and a power of 2 W the trapping frequency in the axial direction is $\omega_y/2\pi = 10$ kHz. In the weak confinement directions there will be an anti-trapping given by [143] as

$$\frac{\omega_x}{2\pi} = \frac{i}{\sqrt{2}\pi} \frac{1}{W_y W_x^{1/2}} \Big(\frac{U_0}{\pi^2 m W_y^2} \Big)^{1/4} \tag{A.4.4}$$

$$\frac{\omega_z}{2\pi} = \sqrt{\frac{3}{2}} \frac{i}{2\pi^2} \frac{\lambda}{W_x^{5/2}} \Big(\frac{U_0}{\pi^2 m W_y^2} \Big)^{1/4} \tag{A.4.5}$$

this would give $\omega_x/2\pi = i3.8$ Hz and $\omega_z/2\pi = i4$ Hz, which with the control over the Feshbach fields will be dominated by the magnetic field curvature. This then gives a maximum aspect ratio of 400 and a critical atom number of ∼80k. The application of this TEM01 mode and the modifications to the magnetic field would allow a much better investigation into the two dimensional world.

Bibliography

[1] G.-D. Lin W. Zhang and L.-M. Duan. BCS-BEC crossover of a quasi-two-dimensional Fermi gas: The significance of dressed molecules. *Physical Review A (Atomic, Molecular, and Optical Physics)*, 77(6):063613, 2008.

[2] S Chu, J. E. Bjorkholm, A. Ashkin, and A. Cable. Experimental observation of optically trapped atoms. *Phys. Rev. Lett.*, 57:314, 1986.

[3] S. Chu, L. Hollberg, and J. E. Bjorkholm. Three-dimensional viscous confinement and cooling of atoms by radiation pressure. *Phys. Rev. Lett.*, 55:48, 1985.

[4] P. D. Lett, R. N. Watts, C. I. Westbrook, and W. D. Phillips. Observation of atoms laser cooled below the Doppler limit. *Phys. Rev. Lett.*, 61:169, 1988.

[5] E. Raab, M. Prentiss, A. Cable, S. Chu, and D. Pritchard. Trapping of neutral-sodium atoms with radiation pressure. *Phys. Rev. Lett.*, 59:2631, 1987.

[6] M. H. Anderson, J. R. Ensher, M. R. Matthews, C. E. Wieman, and E. A. Cornell. Observation of Bose-Einstein condensation in a dilute atomic vapor. *Science*, 269:198, 1995.

[7] K. B. Davis, M.-O. Mewes, M. R. Andrews, N. J. van Druten, D. S. Durfee, D. M. Kurn, and W. Ketterle. Bose-Einstein condensation in a gas of sodium atoms. *Phys. Rev. Lett.*, 75:3969, 1995.

[8] C. C. Bradley, C. A. Sackett, J. J. Tollett, and R. G. Hulet. Bose-Einstein condensation in an atomic gas with attractive interactions. *Phys. Rev. Lett.*, 75:1687, 1995.

[9] H. K. Onnes. On the sudden rate at which the resistance of mercury disappears. *Akad. van Wetenschappen*, 14(113):818, 1911.

[10] D. D. Osheroff, R. C. Richardson, and D. M. Lee. Evidence for a new phase of solid He^3. *Phys. Rev. Lett.*, 28:885, 1972.

[11] L. N. Cooper. Bound electron pairs in a degenerate Fermi gas. *Phys. Rev.*, 104:1189, 1956.

[12] S. J. J. M. F. Kokkelmans, J. N. Milstein, M. L. Chiofalo, R. Walser, and M. J. Holland. Resonance superfluidity: Renormalization of resonance scattering theory. *Phys. Rev. A*, 65(5):053617, May 2002.

[13] C. A. Regal, M. Greiner, and D. S. Jin. Observation of resonance condensation of fermionic atom pairs. *Phys. Rev. Lett.*, 92:040403, 2004.

[14] M. Zwierlein, C. A. Stan, C. H. Schunck, S. M. F. Raupach, A. J. Kerman, and W. Ketterle. Condensation of pairs of fermionic atoms near a Feshbach resonance. *Phys. Rev. Lett.*, 92:120403, 2004.

[15] C. Chin and R. Grimm. Thermal equilibrium and efficient evaporation of an ultracold atom-molecule mixture. *Phys. Rev. A*, 69:033612, 2004.

[16] M. Bartenstein, A. Altmeyer, S. Riedl, S. Jochim, C. Chin, J. Hecker Denschlag, and R. Grimm. Crossover from a molecular Bose-Einstein condensate to a degenerate Fermi gas. *Phys. Rev. Lett.*, 92:120401, 2004.

[17] T. Bourdel, L. Khaykovich, J. Cubizolles, J. Zhang, F. Chevy, M. Teichmann, L. Tarruell, S. J. J. M. F. Kokkelmans, and C. Salomon. Experimental study of the BEC-BCS crossover region in lithium 6. *Phys. Rev. Lett.*, 93:050401, 2004.

[18] J. Kinast, S. L. Hemmer, M. E. Gehm, A. Turlapov, and J. E. Thomas. Evidence for superfluidity in a resonantly interacting Fermi gas. *Phys. Rev. Lett.*, 92:150402, 2004.

[19] G. B. Partridge, K. E. Strecker, R. I. Kamar, M. W. Jack, and R. G. Hulet. Molecular probe of pairing in the BEC-BCS crossover. *Phys. Rev. Lett.*, 95:020404, 2005.

[20] H. Feshbach. Unified theory of nuclear reactions. II. *Annals of Physics*, 19:287, 1962.

[21] E. Tiesinga, B. J. Verhaar, and H. T. C. Stoof. Threshold and resonance phenomena in ultracold ground-state collisions. *Phys. Rev. A*, 47:4114–4122, 1993.

[22] S. Inouye, M. R. Andrews, J. Stenger, H.-J. Miesner, D. M. Stamper-Kurn, and W. Ketterle. Observation of Feshbach resonances in a Bose-Einstein condensate. *Nature*, 392:151, 1998.

[23] Ph. Courteille, R. S. Freeland, D. J. Heinzen, F. A. van Abeelen, and B. J. Verhaar. Observation of a Feshbach resonance in cold atom scattering. *Phys. Rev. Lett.*, 81:69–72, 1998.

[24] D. S. Petrov, C. Salomon, and G. V. Shlyapnikov. Weakly bound dimers of fermionic atoms. *Phys. Rev. Lett.*, 93:090404, 2004.

[25] C. A. Regal, C. Ticknor, J. L. Bohn, and D. S. Jin. Creation of ultracold molecules from a Fermi gas of atoms. *Nature*, 424:47, 2003.

[26] C. A. Regal, M. Greiner, and D. S. Jin. Lifetime of molecule-atom mixtures near a Feshbach resonance in K. *Phys. Rev. Lett.*, 92:083201, 2004.

[27] J. Cubizolles, T. Bourdel, S. J. J. M. F. Kokkelmans, G. V. Shlyapnikov, and C. Salomon. Production of long-lived ultracold Li_2 molecules from a Fermi gas. *Phys. Rev. Lett.*, 91:240401, 2003.

[28] K. E. Strecker, G. B. Partridge, and R. G. Hulet. Conversion of an atomic Fermi gas to a long-lived molecular Bose gas. *Phys. Rev. Lett.*, 91:080406, 2003.

[29] S. Jochim, M. Bartenstein, A. Altmeyer, G. Hendl, S. Riedl, C. Chin, J. Hecker Denschlag, and R. Grimm. Bose-Einstein condensation of molecules. *Science*, 302:2101–2103, 2003.

[30] S. Jochim, M. Bartenstein, A. Altmeyer, G. Hendl, C. Chin, J. Hecker Denschlag, and R. Grimm. Pure gas of optically trapped molecules created from fermionic atoms. *Phys. Rev. Lett.*, 91:240402, 2003.

[31] M. Greiner, C. A. Regal, and D. S. Jin. Emergence of a molecular Bose Einstein condensate from a Fermi gas. *Nature*, 426:537, 2003.

[32] M. W. Zwierlein, C. A. Stan, C. H. Schunck, S. M. F. Raupach, S. Gupta, Z. Hadzibabic, and W. Ketterle. Observation of Bose-Einstein condensation of molecules. *Phys. Rev. Lett.*, 91:250401, 2003.

[33] J. Fuchs, G. J. Duffy, G. Veeravalli, P. Dyke, M. Bartenstein, C. J. Vale, P. Hannaford, and W. J. Rowlands. Molecular Bose-Einstein condensation in a versatile low power crossed dipole trap. *J. Phys. B.*, 40:4109–4118, 2007.

[34] J. Kinast, A. Turlapov, J. E. Thomas, Q. Chen, J. Stajic, and K. Levin. Heat capacity of a strongly interacting Fermi gas. *Science*, 307:1296–1299, 2005.

[35] J. E. Thomas, J. Kinast, and A. Turlapov. Virial theorem and universality in a unitary Fermi gas. *Phys. Rev. Lett.*, 95:120402, 2005.

[36] L. Luo, B. Clancy, J. Joseph, J. Kinast, A. Turlapov, and J. E. Thomas. Evaporative cooling of unitary Fermi gas mixtures in optical traps. *New Journal of Physics*, 8:213, 2006.

[37] J. T. Stewart, J. P. Gaebler, C. A. Regal, and D. S. Jin. Potential energy of a ^{40}K Fermi gas in the BCS-BEC crossover. *Phys. Rev. Lett.*, 97:220406, 2006.

[38] Hui Hu, Xia-Ji Liu, and P. D. Drummond. Universal thermodynamics of strongly interacting Fermi gases. *Nature Physics*, 3:469, 2007.

[39] J. Bardeen, L. N. Cooper, and J. R. Schrieffer. Theory of superconductivity. *Phys. Rev.*, 108:1175, 1957.

[40] N. D. Mermin and H. Wagner. Absence of ferromagnetism or antiferromagnetism in one- or two-dimensional isotropic Heisenberg models. *Phys. Rev. Lett.*, 17(26):1307, 1966.

[41] P. C. Hohenberg. Existence of long-range order in one and two dimensions. *Phys. Rev.*, 158(2):383–386, 1967.

[42] S. Coleman. There are no Goldstone bosons in two dimensions. *Communications in Mathematical Physics*, 31(4):259–264, 1973.

[43] J. W. Kane and L. P. Kadanoff. Long-Range Order in Superfluid Helium. *Phys. Rev.*, 155(1):80–83, Mar 1967.

[44] V. Berezinskii. Destruction of long-range order in one-dimensional and 2-dimensional systems having a continuous symmetry group, 1 - classical systems. *Sov. Phys. JETP-USSR*, 32:493, (1971).

[45] J M Kosterlitz and D J Thouless. Ordering, metastability and phase transitions in two-dimensional systems. *Journal of Physics C: Solid State Physics*, 6(7):1181–1203, 1973.

[46] D. J. Bishop and J. D. Reppy. Study of the superfluid transition in two-dimensional $He4$ films. *Phys. Rev. Lett.*, 40(26):1727–1730, 1978.

[47] A. I. Safonov, S. A. Vasilyev, I. S. Yasnikov, I. I. Lukashevich, and S. Jaakkola. Observation of quasicondensate in two-dimensional atomic Hydrogen. *Phys. Rev. Lett.*, 81(21):4545–4548, 1998.

[48] V. Bagnato and D. Kleppner. Bose-Einstein condensation in low-dimensional traps. *Phys. Rev. A*, 44(11):7439–7441, 1991.

[49] A. Gorlitz, J. M. Vogels, A. E. Leanhardt, C. Raman, T. L. Gustavson, J. R. Abo-Shaeer, A. P. Chikkatur, S. Gupta, S. Inouye, T. Rosenband, and W. Ketterle. Realization of Bose-Einstein condensates in lower dimensions. *Physical Review Letters*, 8713(13):4, 2001.

[50] D. Rychtarik, B. Engeser, M. Hammes, H.-C. Nägerl, and R. Grimm. Crossover to 2D in a double-evanescent wave trap. *J. Phys. IV France*, 116:241, 2004.

[51] N. L. Smith, W. H. Heathcote, G. Hechenblaikner, E. Nugent, and C. J Foot. Quasi-2D confinement of a BEC in a combined optical and magnetic potential. *J. Phys. B.*, 38(3):223–235, (2005).

[52] S. Stock, Z. Hadzibabic, B. Battelier, M. Cheneau, and J. Dalibard. Observation of phase defects in quasi-2D Bose-Einstein condensates. *Phys. Rev. Lett.*, 95(19):190403, 2005.

[53] P. Cladé, and C. Ryu, and A. Ramanathan, and K. Helmerson, and W. D. Phillips . Observation of a 2D Bose gas: from thermal to quasicondensate to superfluid. *Phys. Rev. Lett.*, 102(17):170401, 2009.

[54] J. I. Gillen, W. S. Bakr, A. Peng, P. Unterwaditzer, S. Fölling, and M. Greiner. Two-dimensional quantum gas in a hybrid surface trap. *Physical Review A (Atomic, Molecular, and Optical Physics)*, 80(2):021602, 2009.

[55] Z. Hadzibabic, and P. Kruger, and M. Cheneau, and B. Battelier, and J. Dalibard. Berezinskii-Kosterlitz-Thouless crossover in a trapped atomic gas. *Nature*, 441(7097):1118–1121, 2006.

[56] B. Paredes, A. Widera, V. Murg, O. Mandel, S. Folling, I. Cirac, G. V. Shlyapnikov, T. W. Hansch, and I. Bloch. Tonks-Girardeau gas of ultracold atoms in an optical lattice. *Nature*, 429(6989):277–281, 2004.

[57] T. Kinoshita, T. Wenger, and D. S. Weiss. Observation of a one-dimensional Tonks-Girardeau gas. *Science*, 305(5687):1125–1128, 2004.

[58] H. Moritz, T. Stöferle, K. Günter, M. Köhl, and T. Esslinger. Confinement induced molecules in a 1D Fermi gas. *Phys. Rev. Lett.*, 94(21):210401, 2005.

[59] K. Günter, T. Stöferle, H. Moritz, M. Köhl, and T. Esslinger. p-wave interactions in low-dimensional fermionic gases. *Phys. Rev. Lett.*, 95:230401, 2005.

[60] E. Haller, M. Gustavsson, M. J. Mark, J. G. Danzl, R. Hart, G. Pupillo, and H-C. Nagerl. Realization of an excited, strongly correlated quantum gas phase. *Science*, 325(5945):1224–1227, 2009.

[61] X. Du, Y. Zhang, and J. E. Thomas. Inelastic collisions of a Fermi gas in the BEC-BCS crossover. *Physical Review Letters*, 102(25):250402, 2009.

[62] F. Ferlaino, E. De Mirandes, R. Heidemann, G. Roati, G. Modugno, and M. Inguscio. Quasi-2D Bose-Fermi mixtures in an optical lattice. *J. Phys. IV France*, 116:253–258, oct (2004).

[63] C. J. Pethick and H. Smith. *Bose-Einstein condensation in dilute gases*. Cambridge University Press, 2001.

[64] W. Ketterle and M. W. Zwierlein. *Making, probing and understanding ultracold Fermi gases, Proceedings of the International School of Physics Enrico Fermi, Varenna, 20-30 June 2006*. IOS press, Amsterdam, 2007.

[65] W. Ketterle, D.S. Durfee, and D.M. Stamper-Kurn. Making, probing and understanding Bose-Einstein condensates. *in: M. Inguscio, S. Stringari and C. Wieman eds., Bose-Einstein Condensation in Atomic Gases: Proceedings of the International School of Physics (Enrico Fermi), Varenna 1998*, page 67, 1999.

[66] L. Pitaevskii and S. Stringari. *Bose-Einstein Condensation*. Oxford University Press, 2003.

[67] A. J. Leggett. Bose-Einstein condensation in the alkali gases: some fundamental concepts. *Rev. Mod. Phys.*, 73(2):307–356, 2001.

[68] R. K. Pathria. *Statistical Mechanics, Second Edition*. Butterworth-Heinemann, July 1996.

[69] I. Bloch, J. Dalibard, and W. Zwerger. Many-body physics with ultracold gases. *Reviews of Modern Physics*, 80(3):885, 2008.

[70] A. Posazhennikova. Colloquium: Weakly interacting, dilute Bose gases in 2D. *Rev. Mod. Phys.*, 78(4):1111–1134, 2006.

[71] J. J. Sakurai. *Modern Quantum Mechanics*. Addison Wesley, International Student Edition, 1989.

[72] B. Diu C. Cohen-Tannoudji and F. Laloe. *Quantum Mechanics, Volume Two*. John Wiley & Sons, New York, 1977.

[73] D. J. Griffiths. *Introduction to Quantum Mechanics.* Prentice-Hall Inc., 1995.

[74] L. D. Landau and E. M. Lifshitz. *Course of theoretical physics. Vol. 3: Quantum mechanics. Non-relativistic theory.* Pergamon Press, 2002.

[75] J. Weiner, V. S. Bagnato, S. Zilio, and P. S. Julienne. Experiments and theory in cold and ultracold collisions. *Rev. Mod. Phys.*, 71(1):1–85, 1999.

[76] J. Dalibard. Collisional dynamics of ultra-cold atomic gases. *in: M. Inguscio, S. Stringari and C. Wieman eds., Bose-Einstein Condensation in Atomic Gases: Proceedings of the International School of Physics (Enrico Fermi), Varenna 1998*, page 321, 1999.

[77] C. Chin, R. Grimm, P. Julienne, and E. Tiesinga. Feshbach resonances in ultracold gases. *Rev. Mod. Phys.*, 82(2):1225–1286, Apr 2010.

[78] T. Köhler, K. Góral, and P. S. Julienne. Production of cold molecules via magnetically tunable Feshbach resonances. *Reviews of Modern Physics*, 78(4):1311, 2006.

[79] A. J. Moerdijk, B. J. Verhaar, and A. Axelsson. Resonances in ultracold collisions of ^{6}Li, ^{7}Li, and ^{23}Na. *Phys. Rev. A*, 51(6):4852–4861, 1995.

[80] M. Bartenstein. *From Molecules to Cooper Pairs: Experiments in the BEC-BCS Crossover.* PhD thesis, Innsbruck University, 2005.

[81] J. Fuchs. *Molecular Bose-Einstein condensates and p-wave Feshbach molecules of* $^6Li_2$. PhD thesis, Swinburne University of Technology, 2009.

[82] G. Veeravalli. *Bragg Spectroscopy of a Strongly Interacting Fermi Gas.* PhD thesis, Swinburne University of Technology, 2009.

[83] L. Salasnich. Ideal quantum gases in D-dimensional space and power-law potentials. *Journal of Mathematical Physics*, 41(12):8016–8024, 2000.

[84] F. Dalfovo, S. Giorgini, L. P. Pitaevskii, and S. Stringari. Theory of Bose-Einstein condensation in trapped gases. *Rev. Mod. Phys.*, 71(3):463–512, 1999.

[85] W. Krauth. Quantum Monte Carlo calculations for a large number of Bosons in a harmonic trap. *Phys. Rev. Lett.*, 77(18):3695–3699, 1996.

[86] N.N Bogoliubov. On the theory of superfluidity. *J. Phys (Moscow)*, 11:23, 1947.

[87] E. P. Gross. Structure in quantized vortex in boson systems. *Il Nuovo Cimento*, 20:454, 1961.

[88] L. P. Pitaevskii. Vortex lines in an imperfect Bose gas. *Sov. Phys. JETP*, 13:451, 1961.

[89] S. Giorgini, L. P. Pitaevskii, and S. Stringari. Condensate fraction and critical temperature of a trapped interacting Bose gas. *Phys. Rev. A*, 54:R4633–R4636, 1996.

[90] D. S. Petrov. Three-body problem in Fermi gases with short-range interparticle interaction. *Phys. Rev. A*, 67(1):010703, 2003.

[91] S. Giorgini, L. P. Pitaevskii, and S. Stringari. Theory of ultracold atomic Fermi gases. *Reviews of Modern Physics*, 80(4):1215, 2008.

[92] D. S. Petrov, C. Salomon, and G. V. Shlyapnikov. Scattering properties of weakly bound dimers of fermionic atoms. *Phys. Rev. A*, 71:012708, 2005.

[93] M. Tinkham. *Introduction to superconductivity.* McGraw-Hill, New York, 1966.

[94] M. Houbiers, R. Ferwerda, H. T. C. Stoof, W. I. McAlexander, C. A. Sackett, and R. G. Hulet. Superfluid state of atomic 6 Li in a magnetic trap. *Phys. Rev. A*, 56:4864, 1997.

[95] G. A. Baker. Neutron matter model. *Phys. Rev. C*, 60(5):054311, Oct 1999.

[96] H. Heiselberg. Fermi systems with long scattering lengths. *Phys. Rev. A*, 63(4):043606, 2001.

[97] Yusuke Nishida and Dam Thanh Son. ϵ Expansion for a Fermi gas at infinite scattering length. *Physical Review Letters*, 97(5):050403, 2006.

[98] A. Perali, P. Pieri, and G. C. Strinati. Quantitative comparison between theoretical predictions and experimental results for the BCS-BEC crossover. *Phys. Rev. Lett.*, 93(10):100404, 2004.

[99] R. Haussmann, W. Rantner, S. Cerrito, and W. Zwerger. Thermodynamics of the BCS-BEC crossover. *Physical Review A (Atomic, Molecular, and Optical Physics)*, 75(2):023610, 2007.

[100] H. Hu, X.-J. Liu, and P. D. Drummond. Equation of state of a superfluid Fermi gas in the BCS-BEC crossover. *EPL (Europhysics Letters)*, 74(4):574–580, 2006.

[101] G. B. Partridge, W Li, R. I. Kamar, Y. Liao, and R. G. Hulet. Pairing and phase separation in a polarized Fermi gas. *Science*, 311:503–505, 2006.

[102] L. Tarruell, M. Teichmann, J. McKeever, T. Bourdel, J. Cubizolles, L. Khaykovich, J. Zhang, N. Navon, F. Chevy, and C. Salomon. Expansion of an ultra-cold lithium gas in the BEC-BCS crossover, Proceedings of the International School of Physics Enrico Fermi, Varenna, 20-30 June 2006. pages pp. 95–287, 2007.

[103] M. W. Zwierlein, A. Schirotzek, C. H. Schunck, and W. Ketterle. Fermionic superfluidity with imbalanced spin populations. *Science*, 311:492, 2006.

[104] F. Gleisberg, W. Wonneberger, U. Schlöder, and C. Zimmermann. Noninteracting fermions in a one-dimensional harmonic atom trap: Exact one-particle properties at zero temperature. *Phys. Rev. A*, 62(6):063602, 2000.

[105] P. Vignolo and A. Minguzzi. Shell structure in the density profiles for noninteracting fermions in anisotropic harmonic confinement. *Phys. Rev. A*, 67(5):053601, 2003.

[106] J. Schneider and H. Wallis. Mesoscopic Fermi gas in a harmonic trap. *Phys. Rev. A*, 57(2):1253–1259, 1998.

[107] E. J. Mueller. Density profile of a harmonically trapped ideal Fermi gas in arbitrary dimension. *Phys. Rev. Lett.*, 93(19):190404, 2004.

[108] Brian O'Sullivan and Thomas Busch. Spontaneous emission in ultracold spin-polarized anisotropic Fermi seas. *Physical Review A (Atomic, Molecular, and Optical Physics)*, 79(3):033602, 2009.

[109] I. Richard Lapidus. Quantum-mechanical scattering in two dimensions. *American Journal of Physics*, 50(1):45–47, 1982.

[110] S. K. Adhikari. Quantum scattering in two dimensions. *American Journal of Physics*, 54(4):362–367, 1986.

[111] Sadhan K. Adhikari and Mahir S. Hussein. Semiclassical scattering in two dimensions. *American Journal of Physics*, 76(12):1108–1113, 2008.

[112] D. S. Petrov and G. V. Shlyapnikov. Interatomic collisions in a tightly confined Bose gas. *Phys. Rev. A*, 64(1):012706, 2001.

[113] M. Randeria, J. M. Duan, and L. Y. Shieh. Bound states, Cooper pairing, and Bose condensation in two dimensions. *Phys. Rev. Lett.*, 62(9):981–984, 1989.

[114] M. Drechsler and W. Zwerger. Crossover from BCS-superconductivity to Bose-condensation. *Annalen der Physik*, 504(1):15–23, 1992.

[115] V. P. Gusynin, V. M. Loktev, and S. G. Sharapov. Pseudogap phase formation in the crossover from Bose-Einstein condensation to BCS superconductivity. *Journal of Experimental and Theoretical Physics*, 88(4):685–695, 1999.

[116] S. S. Botelho and C. A. R. Sá de Melo. Vortex-Antivortex lattice in ultracold Fermionic gases. *Physical Review Letters*, 96(4):040404, 2006.

[117] W. Zhang, G.-D. Lin, and L.-M. Duan. Berezinskii-Kosterlitz-Thouless transition in a trapped quasi-two-dimensional Fermi gas near a Feshbach resonance. *Physical Review A (Atomic, Molecular, and Optical Physics)*, 78(4):043617, 2008.

[118] J. P. Kestner and L.-M. Duan. Effective low-dimensional Hamiltonian for strongly interacting atoms in a transverse trap. *Physical Review A (Atomic, Molecular, and Optical Physics)*, 76(6):063610, 2007.

[119] S. Jochim. *Bose-Einstein Condensation of Molecules*. PhD thesis, Innsbruck University, 2004.

[120] U. Schünemann, H. Engler, R. Grimm, M. Weidemüller, and M. Zielonkowski. Simple scheme for tunable frequency offset locking of two lasers. *Review of Scientific Instruments*, 70(1):242–243, 1999.

[121] R. Grimm, M. Weidemüller, and Y. Ovchinnikov. Optical dipole traps for neutral atoms. *Adv. At. Mol. Opt. Phys.*, 42:95, 2000.

[122] H. J. Metcalf and P. v. d. Straten. *Laser Cooling and Trapping*. Springer-Verlag, Heidelberg, 1999.

[123] N. F. Ramsey. *Molecular Beams, 2nd Edn.* Clarendon, Oxford, 1989.

[124] W. D. Phillips and H. Metcalf. Laser deceleration of an atomic beam. *Phys. Rev. Lett.*, 48:596–599, 1982.

[125] Michael A. Joffe, Wolfgang Ketterle, Alex Martin, and David E. Pritchard. Transverse cooling and deflection of an atomic beam inside a Zeeman slower. *J. Opt. Soc. Am. B*, 10:2257, 1993.

[126] X. Xu, T. H. Loftus, M. J. Smith, J. L. Hall, A. Gallagher, and J. Ye. Dynamics in a two-level atom magneto-optical trap. *Phys. Rev. A*, 66:011401, 2002.

[127] C. S. Adams, H. J. Lee, N. Davidson, M. Kasevich, and S. Chu. Evaporative cooling in a crossed dipole trap. *Phys. Rev. Lett.*, 74:3577, 1995.

[128] O. J. Luiten, M. W. Reynolds, and J. T. M. Walraven. Kinetic theory of the evaporative cooling of a trapped gas. *Phys. Rev. A*, 53(1):381–389, 1996.

[129] M. E. Gehm, S. L. Hemmer, K. M. O'Hara, and J. E. Thomas. Unitarity-limited elastic collision rate in a harmonically trapped fermi gas. *Phys. Rev. A*, 68(1):011603, Jul 2003.

[130] K. M. O'Hara, M. E. Gehm, S. R. Granade, and J. E. Thomas. Scaling laws for evaporative cooling in time-dependent optical traps. *Phys. Rev. A*, 64:051403, 2001.

[131] D. S. Petrov, M. Holzmann, and G. V. Shlyapnikov. Bose-Einstein condensation in quasi-2D trapped gases. *Phys. Rev. Lett.*, 84(12):2551–2555, 2000.

[132] Q. Chen, J. Stajic, S. Tan, and K. Levin. BCS-BEC crossover: From high temperature superconductors to ultracold superfluids. *Physics Reports*, 412, 2005.

[133] Hui Hu, A. Minguzzi, Xia-Ji Liu, and M. P. Tosi. Collective modes and ballistic expansion of a Fermi gas in the BCS-BEC crossover. *Phys. Rev. Lett.*, 93(19):190403, 2004.

[134] B. E. Clancy. *Hydrodynamics of a rotating strongly interacting Fermi gas.* PhD thesis, Duke University, 2008.

[135] P. Dyke, E. Kuhnle, W. Rowlands, P.Hannaford, and C. Vale. Confinement induced resonance in a strongly interacting Fermi gas of ^{6}Li. *In preparation*, 2009.

[136] J. Fuchs, C. Ticknor, P. Dyke, G. Veeravalli, E. Kuhnle, W. Rowlands, P. Hannaford, and C. J. Vale. Binding energies of ^{6}Li p-wave Feshbach molecules. *Phys. Rev. A*, 77:053616, 2008.

[137] J. Zhang, E. G. M. van Kempen, T. Bourdel, L. Khaykovich, J. Cubizolles, F. Chevy, M. Teichmann, L. Tarruell, S. J. J. M. F. Kokkelmans, and C. Salomon. P-wave feshbach resonances of ultracold li-6. *Physical Review A*, 70(3):–, 2004.

[138] J. P. Gaebler, J. T. Stewart, J. L. Bohn, and D. S. Jin. p-wave feshbach molecules. *Physical Review Letters*, 98(20):–, 2007.

[139] Y. Inada, M. Horikoshi, S. Nakajima, M. Kuwata-Gonokami, M. Ueda, and T. Mukaiyama. Collisional properties of p-Wave Feshbach molecules. *Physical Review Letters*, 101(10):100401, 2008.

[140] J. Levinsen, N. R. Cooper, and V. Gurarie. Stability of fermionic gases close to a p-wave Feshbach resonance. *Physical Review A (Atomic, Molecular, and Optical Physics)*, 78(6):063616, 2008.

[141] G. Veeravalli, E. Kuhnle, P. Dyke, and C. J. Vale. Bragg spectroscopy of strongly interacting Fermi gas. *Phys. Rev. Lett.*, 101:250403, 2008.

[142] M. Iskin and C. A. R. Sá de Melo. Evolution from BCS to Berezinskii-Kosterlitz-Thouless superfluidity in one-dimensional optical lattices. *Physical Review Letters*, 103(16):165301, 2009.

[143] T. Meyrath, F. Schreck, J. Hanssen, C. Chuu, and M. Raizen. A high frequency optical trap for atoms using Hermite-Gaussian beams. *Opt. Express*, 13(8):2843–2851, 2005.

[144] T. Bergeman, Gidon Erez, and Harold J. Metcalf. Magnetostatic trapping fields for neutral atoms. *Phys. Rev. A*, 35(4):1535–1546, 1987.

[145] S. Stock. *Quantized vortices in a Bose-Einstein condensate: thermal activation and dynamic nucleation*. PhD thesis, Laboratoire Kastler Brossel, 2006.

[146] B. E. A. Saleh and Malvin C. Teich. *Fundamentals of Photonics*. Wiley-Interscience, 1st edition, August 1991.

Publications of the author

From the contents of this thesis and contributions to the old experiments :

G. Veeravalli, E. Kuhnle, P. Dyke, and C. J. Vale.
Bragg spectroscopy of strongly interacting Fermi gas,
Phys. Rev. Lett. **101**, 250403 (2008).

J. Fuchs, G. J. Duffy, G. Veeravalli, P. Dyke, M. Bartenstein, C. J. Vale,
P. Hannaford and W. J. Rowlands.
Molecular Bose-Einstein condensation in a versatile low power crossed dipole trap,
J. Phys. B. **40**, 4109 (2007).

J. Fuchs, C. Ticknor, P. Dyke, G. Veeravalli, E. Kuhnle, W. Rowlands, P. Hannaford and C. J. Vale.
Binding Energies of ^{6}Li p-wave Feshbach Molecules,
Phys. Rev. A. **77**, 053616 (2008).